Ph.D. Dissertation

Spin-related Phenomena in BiSb Topological Insulator – Ferromagnet Bilayers

Nguyen Huynh Duy Khang

Dissertation supervisor
Associate Professor Pham Nam Hai

Department of Electrical and Electronic Engineering
Tokyo Institute of Technology

July, 2019

Thesis Defense Committee:

Associate Professor Pham Nam Hai (Chair)

Professor Shigeki Nakagawa

Professor Takaaki Manaka

Professor Akira Yamada

Professor Masaaki Tanaka

Associate Professor Shinsuke Miyajima

Contents

Chapter 1

Introduction

This chapter gives a brief overview on the concept of spintronics with its key technology's features. Typical spintronic memory devices and their working principles will be explained, with emphasis on recent developments on spins-orbitronic devices. Next, topological insulators and BiSb in particular will be presented as one of solutions for ultralow power spintronic memory devices from the material view point. From these backgrounds, the motivation and thesis outline will be presented.

1.1. Spintronics

Just two decades ago, "desktop computer" was still a very strange term in electronics. Nowadays it has been become very popular but nearly replaced by mobile devices like smartphones or laptops thank to the dazzling speed of technology development. In order to make these devices more powerful, shrinking the size with denser storage capacity and high speed operation have become the main topic of electronic industry and academic researchers. The early progress of computing technology that leads to the Digital Revolution can be traced back to the introduction of the transistor invented in 1947 by J. Barden, W. Shockley and W. Brattain [1]. Because of its huge impact in development of the semiconductor industry, they received the Nobel Prize in Physics in 1956. Since then, the number of transistors that would be able to fit on a dense integrated circuit has doubled every 18 months, and it is known as the Moore's law [2, 3]. However, continuous progress that pushed the electrical circuits to the nano-scale regime has resulted in huge electric energy leakage. The concept of electron's transportation has begun to pose serious problems and simply packing additional features into the same area to improve performance of circuits has become more and more difficult. To further decrease the size of the devices and continuously enhance their performance while suppressing the energy leakage problem, spintronics comes into play [4].

The spintronics or spin electronics can be known as combination between electric charge and its intrinsic form of angular momentum called spin. In Figure 1.1, the concept of spintronics is described as overlap between electronic engineering (electric charge) and magnetic engineering (spin). Instead of using the "existence' or "absence" of the electric charge, the bit "0" and "1" of the binary data can be expressed by up-spin (↑) or down-spin (↓). Because of the unchanged state of spin under the loss of supplied power and additional functionality that can be controlled by external magnetic field, spintronics exhibit unique advantages expected for low power consumption, non-volatility and high speed's applications [5, 6].

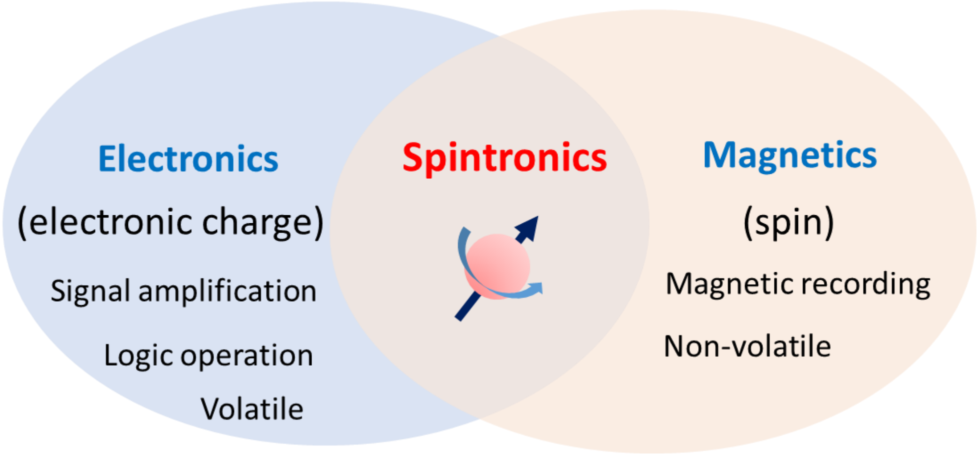

Figure 1.1: The concept of spintronics.

The pioneering work in spintronics can be considered starting from understanding of spin-polarized transport at low temperature in ferromagnetic metals investigated by Nevill Francis Mott [7, 8]. They observed an unusual behavior of resistance due to the un-mixing scattering process of the majority and minority spin, which was further explained as two different spin projections in the two-current model proposed by I. A.

Campbell and A. Fert [9]. Then, the giant magnetoresistance (GMR) effect from the electrical transport measurements of Fe/Cr multilayers system was discovered by P. Grunberg and A. Fert [10]. In multilayers consisting of two or more ferromagnetic (FM) layers separated by a non-magnetic (NM) layer, the GMR arises from spin-dependent scattering of conduction electrons at the interface of FM/NM multilayers and in the bulk of FM that results in the difference between low and high resistance, when the FM layer magnetization's direction of the two FM layers are parallel and antiparallel to each other, respectively. Shortly after, it was realized that GMR can be enhanced by driving the current perpendicular to the film plane, as shown in Fig. 1.2.

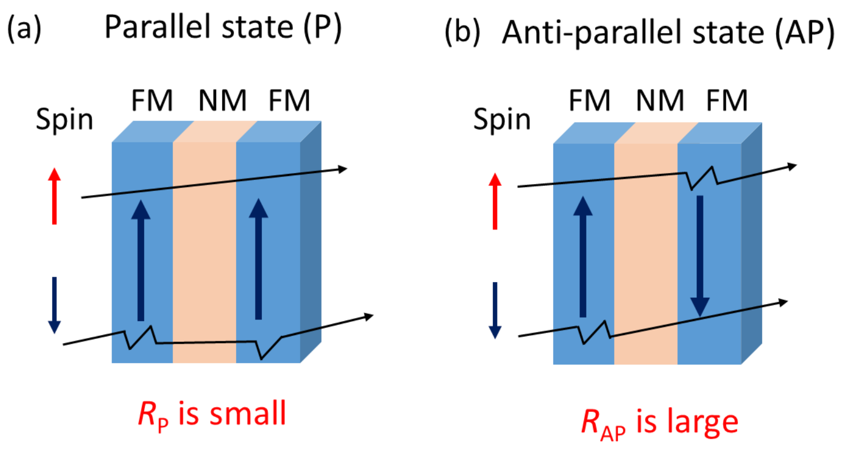

Figure 1.2: Schematic illustrates of (a) Parallel state (P) and (b) Anti-parallel state in GMR effect.

The GMR effect has not only highlighted the critical role of electron spins in electrical transport but also impressively boosted the sensitivity of GMR based magnetic field sensors. Thanks to its high performance in magnetic field's detection, P. Grunberg and A. Fert were honored with a Nobel Prize in Physics in 2007, and there has been a huge effort to deeply understand the GMR effect in order to further enhance its magnitude [11, 12, 13, 14].

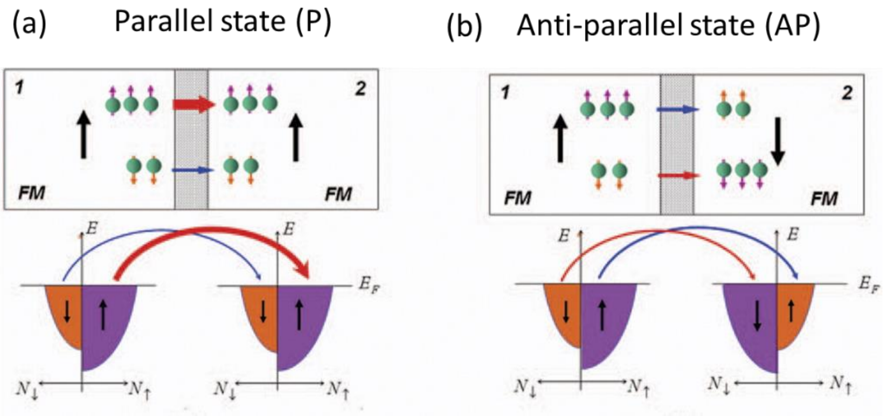

Figure 1.3: Schematic illustrates of (a) Parallel state (P) and (b) Anti-parallel state in TMR effect. Reproduced with permission [15].

In 1975, Julliere experimentally discovered the tunneling magnetoresistance (TMR) effect in a three-layer structure where an insulator layer is used for separating two ferromagnetic layers instead of a NM layer as in the case of GMR. This structure is called magnetic tunnel junction (MTJ), and the TMR effect is the result of a spin polarized current tunneling through the insulator layer, as shown in Fig. 1.3. The electron spins in one electrode can only tunnel to the electronic states with same spin orientation in the opposite electrode. Depending on the magnetization configuration (parallel state or anti-parallel state), the MTJ resistance can be changed as the consequence of spin polarized tunneling. However, because of its small magnitude at the time when spintronics is immature, TMR effect needs over 15 year to get attention and finally matures with realization of a giant TMR ratio over 400% at room temperature in Co/MgO/Co multiple layers in 2006 [15].

Because of the great potential and impact of GMR and TMR, over three decades, huge efforts have been spent to apply them to memory applications [16-28].

1.2. Spintronic memory devices

1.2.1. Magnetic read heads for hard disk drive (HDD)

Since 2006, the TMR effect has played a major role in implementation of the spin degree of freedom to spintronic devices, and the read head of hard disk drives is an example of great success. Figure 1.4 illustrates the MTJ read head in an HDD. The read head structure includes a pinned layer, whose magnetic direction is constrained by an exchange bias field arising from the interface with an antiferromagnetic layer. By choosing a particular metallic interlayer of adequate thickness, the magnetic moment of the free layer is always antiferromagnetically coupled with that of the pinned layer. Under influence of magnetic fields associated with the magnetic domains in the recording media, the free layer of the MTJ can change its magnetization and results in the change of the device resistance due to the TMR effect.

Since the magnetic domain of a single bit in HDD can become very small, at present the density of surface recording is reaching 1 Tbit/inch^2 for the area per bit of 25×25nm^2 [29]. On the other hand, because of extremely small magnetic flux leaking from a small domain in high density HDD, magnetic read heads with higher sensitivity need to be developed, when HDD with a surface recording density exceeding 1 Tbit/cm^2 is considered. There have been a lot of investigations in material engineering with high spin polarization ferromagnets such as Fe, Co and CoFeB in order to increase the sensitivity when influenced by a small magnetic flux [15]. However, TMR poses the problem with its too high resistivity which increases Johnson and shot noise as well as limits the data rate [15]. Recently, MgO-based MTJ as shown in Fig. 1.4(b) has become a great solution for HDD read head, because it can achieve very high TMR ratio comparing with other kind of barrier layers, while device resistance can be controlled by optimizing the barrier thickness.

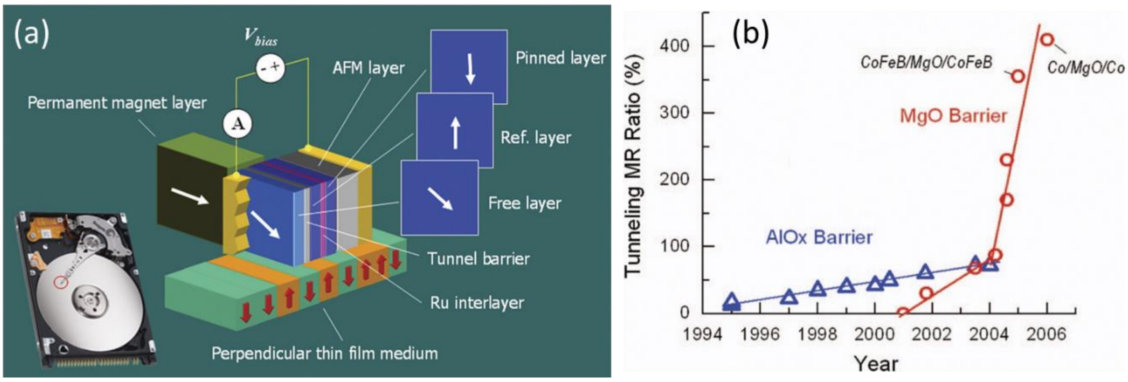

Figure 1.4: (a) MTJ read head in an HDD. The free layer of MTJ can freely rotate its magnetization to response to the stray fields associated with magnetic domains in the recording media. (b) Reported room-temperature TMR ratios over the past decade for AlO_x-based MTJ and MgO-based MTJ. Reproduced with permission [15].

1.2.2. Magnetic random access memory (MRAM) and Spin-transfer torque (STT) – MRAM

Magnetic random access memory (MRAM), a type of memory with non-volatility, high speed and high durability is another well-known application of the TMR effect. Comparing with volatile memories, such as the static random access memory (SRAM) and dynamic random access memory (DRAM), MRAM inherits the unique characteristic of non-volatile memories that they do not need the power to maintain the data bits. Figure 1.4(a) visualizes the mechanism of MRAM. Instead of using magnetic domains to store the information like HDD, MRAM uses the free layer to record each data bit with two states (parallel or anti-parallel) depending on the relative direction between its magnetization and that of the reference layer. The reading process is achieved by measuring the device resistance. In the first generation of MRAM (toggle MRAM), the writing process utilizes the Oersted field generated by a nearby current. However, this writing method requires a large current that does not scale with the MTJ size, limiting the bit density of toggle MRAM.

In 1996, Slonczewski and Berger independently predicted that a spin polarized current can induce a torque on the magnetization of the ferromagnetic layer of MTJ [20, 21] that can be used for magnetization switching. This phenomena is named as the spin-transfer torque (STT) with very promising implications. Three years after the theoretical prediction, STT effect has been experimentally demonstrated by Tsoi et al., Myers et al. and Wegrowe et al for the first time [30, 31, 32]. With this discovery, MRAM was pushed to the next generation where the magnetization of the recording layer can be manipulated by a spin polarized current, instead of an Oersted field. As illustrated in Fig. 1.4(b), when a charge current is passed through the MTJ, it will be polarized by the fixed layer to become the spin-polarized current and injected into the free layer to switch the magnetization of the free layer. STT-MRAM has evolved as the second generation MRAM.

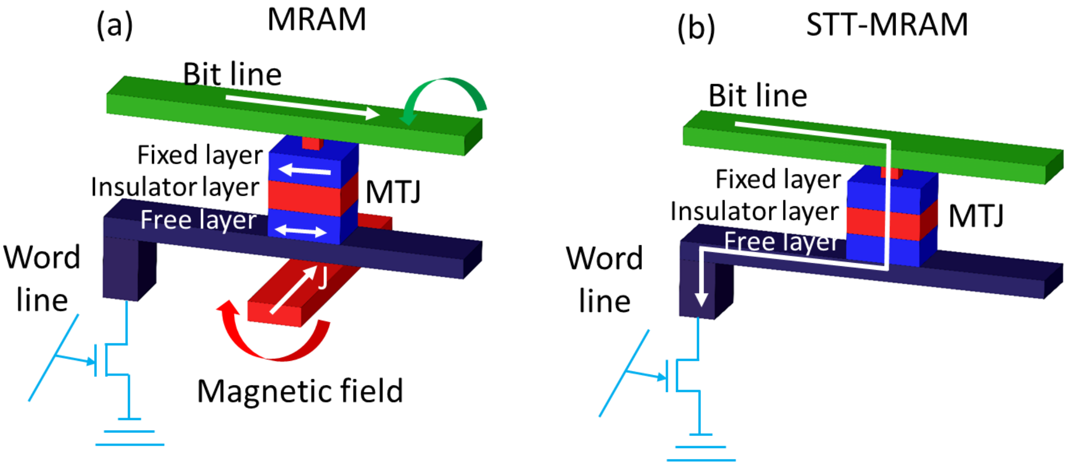

Figure 1.4: Schematic illustrates of (a) toggle magnetoresistive random access memory (MRAM) and (b) spin transfer torque (STT) – MRAM.

Although STT-MRAM shows the big advantage in higher bit density which can reach gigabits per chip storage capacity with lower writing power than that of toggle MRAM, the writing current and writing energy of MRAM is still worse than conventional volatile memory like SRAM or DRAM by one order of magnitude, as shown in Table 1.1. The large current in the writing process can lead to the breakdown of the tunnel barrier oxide. The read disturbance or accident switching of the magnetic states can also happen as the result of the read and write current path's coupling. In addition, high writing current requires large driving transistors, which makes it difficult to further increase the bit density of MRAM [23].

Table 1.1: Read latency (ns), write latency (ns), write energy (nJ) and device size (mm^2) of STT-MRAM, SRAM and DRAM.

	STT-MRAM	**SRAM**	**DRAM**
Read latency (ns)	**3.1**	4.5	4.3
Write latency (ns)	**11.2**	4.5	4.3
Write Energy (nJ)	**20.3**	2.2	1.8
Size (mm^2)	**16.4**	80.4	37.4

The reason of the high writing current in STT-MRAM is due to the limitation of the spin-polarization *P* of the reference layer. As illustrated in Fig. 1.5(a), the spin current generated by the injected charge current I_C is given by

$$I_S = (\hbar/2e)PI_C, \tag{1.1}$$

where $\hbar$ is the reduced Plank constant, and *e* is the elementary charge.

The fact that $P \le 1$ limits the amount of spin current I_S generated by a given I_C and makes it difficult to reduce the writing current. For the next generation of magnetic memory that can compete with commercial DRAM, MRAM must operate with shorter write latency, lower power consumption and higher bit density.

1.2.3. Spin-orbit torque (SOT)-MRAM

Recently, spin-orbit torque (SOT)-MRAM has emerged as an alternative magnetic memory which can overcome the big disadvantages of STT-MRAM. In SOT-MRAM, a spin Hall layer is in contact with the free magnetic layer. As illustrated in Fig. 1.5 (b), a charge current flowing in the spin Hall layer can generate a pure spin current perpendicular to the interface by the spin Hall effect. This pure spin current can exerts a spin torque (so called spin-orbit torque) on the free layer and switch its magnetization (this effect will be explained further in the chapter 2). The spin current generated by this way is given by

$$I_S = (\hbar/2e)(L/t)\theta_{SH} I_C \qquad \textbf{(1.2)}$$

where L is the MTJ size, t the thickness of the spin source layer, and θ_{SH} is the spin Hall angle.

Since L/t is about 10 in realistic MTJs, SOT switching may be more effective than STT switching if $\theta_{SH} > 0.1$.

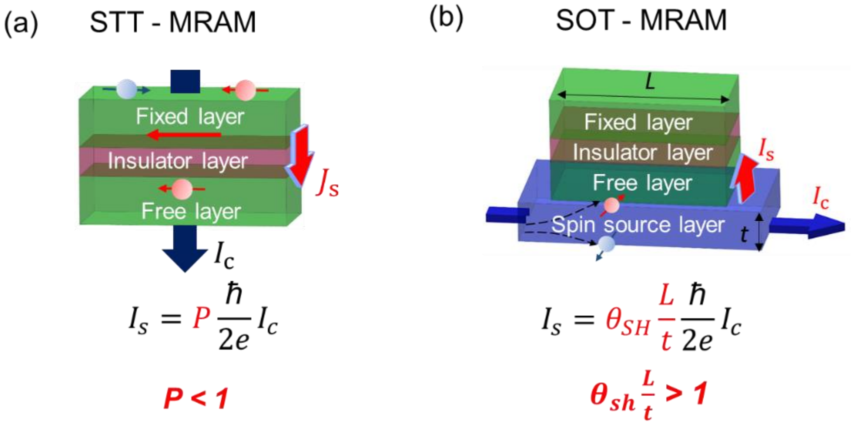

Figure 1.5: Schematic illustrates switching mechanism in writing process of (a) STT-MRAM and (b) SOT-MRAM.

The spin dynamics in STT-MRAM as well as SOT-MRAM is described by the Landau-

Liftshitz-Gilbert equation [33]

$$\frac{\partial m}{\partial t} = -\gamma m \times H_{eff} + \alpha m \times \frac{\partial m}{\partial t} + \beta(\mathrm{m} \times (\sigma \times \mathrm{m})) \qquad \textbf{(1.3)}$$

where ***m*** is free layer's magnetization vector, $\boldsymbol{H}_{\mathbf{eff}}$ is the sum of the anisotropy field, the demagnetizing field and the external field, α is the damping constant, β is the spin torque coefficient and σ is the spin polarization.

In the right hand side, the first term presents for precession of ***m*** under $\boldsymbol{H}_{\mathbf{eff}}$, the second term stand for the damping torque, the final term is the spin torque. In the case of STT-MRAM, the spin current injected into the free layer has the spin polarization in the same direction with the free layer's magnetization ($\boldsymbol{\sigma} \parallel \boldsymbol{m}$). As the results, at the beginning the spin torque is nearly zero, and the write speed is slow (~ 10 ns at acceptable current densities). In contrast, in the case of SOT-MRAM, the spin polarization of the pure spin current injected into the free layer is perpendicular to the magnetization. Thus, the spin torque gets maximum value, and the writing speed of SOT-RAM is at least 20 time larger than that of STT-MRAM (200-500 ps). Inheriting both the low write current and high speed, SOT-MRAM can significantly decrease the writing energy.

Moreover, SOT-MRAM has separated reading path and writing path as shown in Fig. 1.6. The writing current does not flow through the MTJ in the writing process, and this scheme can drastically enhance the MTJ's reliability. Moreover, because of the reduced charge current in the writing process, SOT-MRAM requires much smaller driving transistor and can increase the bit density. With these advantages, SOT-MRAM has become very attractive as the promising candidate for the third generation MRAM with fast writing, low writing energy and high bit density.

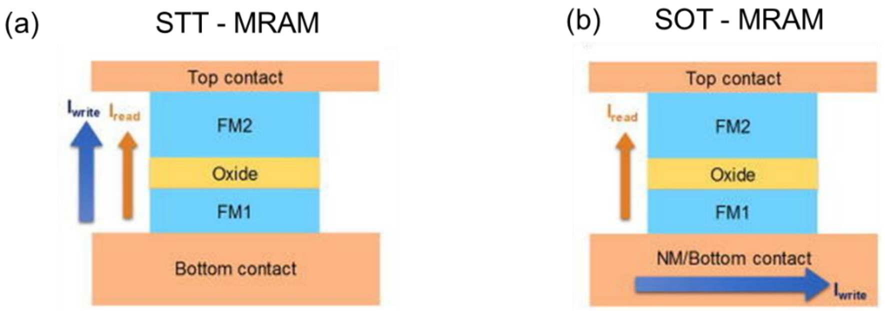

Figure 1.6: Schematic describing the read and write path in (a) STT-MRAM and (b) SOT-MRAM. Reproduced with permission [23].

1.2.4. Racetrack memory

In 2008, Parkin *et al.* proposed a new design of magnetic memory where information can be stored in magnetic domains of U-shaped nanowires, as shown in Fig. 1.7. This memory is called racetrack memory. The position of magnetic domains in racetrack memory is controlled by a pulse current injected from one terminal of the U-shaped nanowire. These magnetic domains can be read out by a MTJ device, while the writing process can be achieved by using STT or SOT in a similar way to STT-MRAM or SOT-MRAM, respectively. Its write and read latency can be less than a nano-second. Comparing with HDD, racetrack memory shows higher performance and greater reliability, since it does not rely on the mechanical mechanism.

One unique characteristic of racetrack memory is its 3D structure. A racetrack memory can use hundreds of millions of U-shaped nanowires arranged vertically like a forest in a very small area size [27]. This characteristic allows racetrack memory to store a vast amounts of data, and makes racetrack memory become a very attractive memory. As for today, intensive research studies are being carry out to further improve the device’s operating speed.

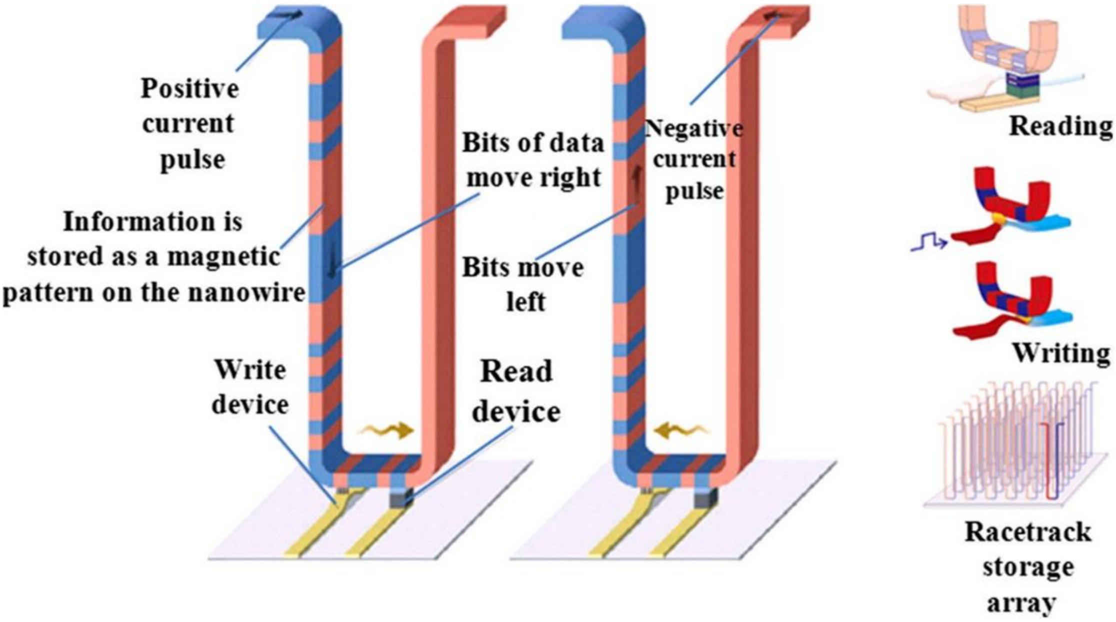

Figure 1.7: Schematic of racetrack memory in an array of U-shaped magnetic nanowires. Reproduced with permission [28].

1.3. Recent evolution of spintronics: Spin-orbitronics

Figure 1.8 summarizes the major achievements in thin film magnetism and spintronics researches in the last decades. Once can see that spintronics is not restricted to the GMR or TMR's concept discovered by previous pioneers, but this field has been steadily evolving in a new road thank to innovation in spin-orbit interaction (SOI) related phenomena. These phenomena can change direction of spintronics to a new line called spin-orbitronics. Instead of using the exchange interaction between conduction electron spin and local spin in magnetic material to create spin polarization, the spin-orbitronics exploits SOI in paramagnetic materials to generate or even detect the spin-polarized current. This idea has expanded spintronics to much broader spectra where spin devices employ not only magnetic materials but also nonmagnetic materials with strong SOI.

The Rashba effect, the spin Hall effect (SHE) or the helical surface states in topological insulators (TIs) is typical examples of SOI. In 1960, the Rashba effect was discovered in materials with broken inversion symmetry and uncompensated electric fields at the interface between two different materials. This leaded to new ideas of spin current generation by Edelstein [34] (thus called Rashba-Edelstein effect or REE for short) and experimentally confirmed in GaMnAs [35] by observing a field-like torque. Similarly, an antidamping-like torque in Pt/Co thin films [36] was reported as an evidence of a pure spin current generated by SHE. Comparing with $P < 1$ as the limitation of STT, both REE and SHE can generate spin currents more efficiently and can be directly applied to SOT-MRAM [36]. Because of these advantages, intense efforts from different groups have been carried out to understand SOI-related phenomena in various materials. Historically, SHE was first observed in 2004 by Y. K. Kato in a GaAs semiconductor layer [37]. Since then, numerous researches on SHE and related phenomena have been published for different kind of materials, such as heavy metal (Pt [36], Ta [38] or W [39]), anti-ferromagnet (PtMn [40] or IrMn [41]) and even oxidized material like W(O) [42].

SOT generated by REE or SHE can also play a central role in domain wall motion in racetrack memory by combining the magnetic layer with another material showing strong SOI. This can enhance the operating speed and further reduce the driving current density of the racetrack memory. There have been many experiments demonstrating this plausible structure in different kind of bilayers [43, 44, 45].

The chiral domain walls from Dzyaloshinskii-Moriya interaction (DMI) or the magnetic skyrmions [46] is another example of SOI. Because skyrmions (whose concept will be presented in more details in the chapter 2) have small size and ultra-low driven current density, they have become extremely popular recently for the next generation of racetrack memory [47].

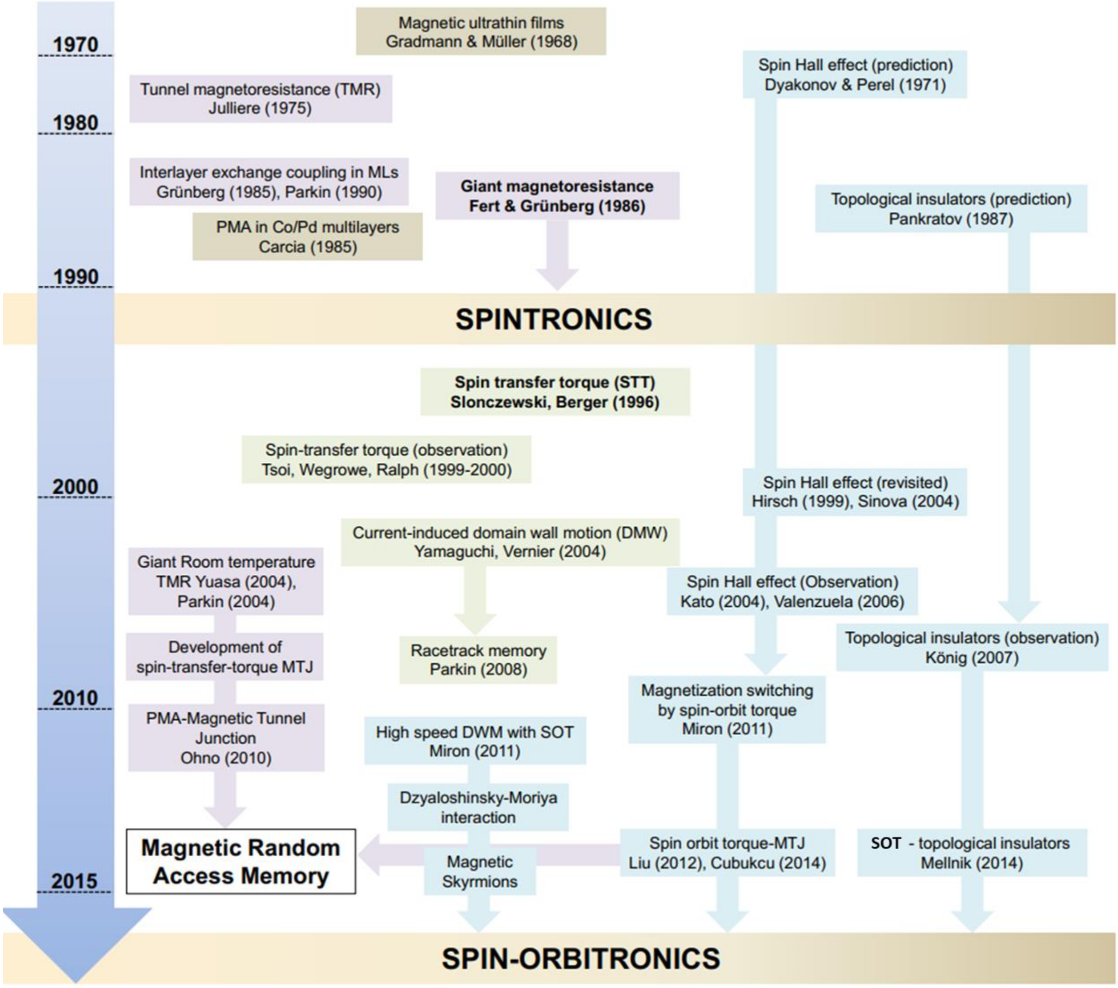

Figure 1.8: Summary of major achievements in the evolution of the thin film magnetism and spintronics research in the last decades. Reproduced with permission [48].

1.4. Topological insulator

Recently, topological insulator (TIs) have emerged as exotic materials possessing huge SOI. TIs are quantum materials with a band gap just like normal insulators but with topological protected conducting surface/edge states. Because their electrons in the valence band and conducting band are under a strong SOI, the conduction band bottom may become lower than the valence band top. This is called invert band structure. Although the inside of TI materials is similar to normal insulators, states related to the invert band structure are formed on the edges/surfaces for 2D/3D TIs. These states permit the emergence of a pair of electrical currents flowing with reverse direction and spin. This is called helicity and can be imaged as two-way highway where each spin flows in one direction and back scattering is prohibited, as illustrated in Fig. 1.9(b) and Fig. 1.9(c). The helical spin polarization of topological surface states on the surface Brillouin zone of 3D TIs with the electron spin orthogonal to direction of their motion is called spin-momentum locking, as shown in Fig. 1.9(d).

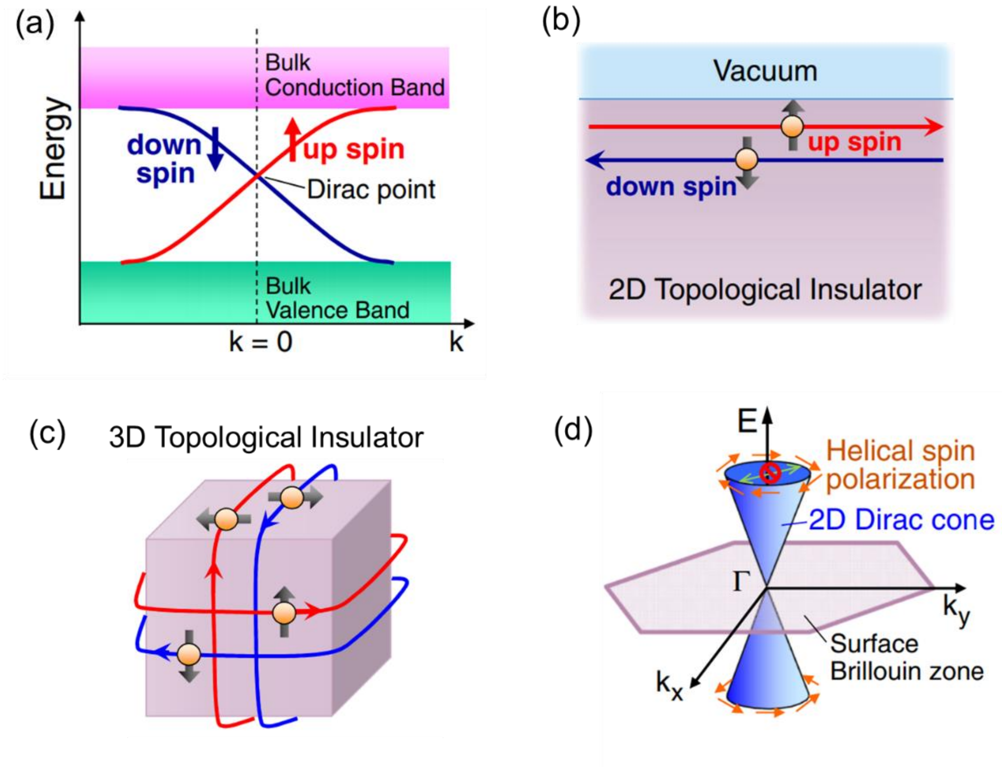

Figure 1.9: (a) Energy dispersion of the spin non-degenerate edge state of a 2D TI forming a 1D Dirac cone. (b) Schematic real-space picture of the 1D helical edge sate of a 2D TI. (c) Schematic real-space picture of the 2D helical surface state of 3D TI. (d) 2D Dirac cone. Reproduced with permission [49].

In 2007, the spin polarized topological edge states in 2D TIs was first observed in HgTe-based quantum wells by M. König [50]. 2D surface states of 3D TI were then observed directly using angle resolve photoemission spectroscopy (ARPES). Importantly, 3D TIs feature very large SHE. Giant spin Hall angle in TIs was observed in Bi_2Se_3 [51] and $(Bi_{0.5}Sb_{0.5})_2Te_3$ [52]. Their spin Hall angle is at least one order of magnitude larger than that of heavy metals, anti-ferromagnets or oxidized materials. That means TIs can provide much higher charge-to-spin conversion efficient than regular spin source materials due to their strong SOI. Figure 1.10(a) compares the power consumption of SOT switching by using TI and heavy metal as the spin source. SOT switching based on TIs can reduce the power consumption down to less than 25%. These results make TI become a very hot topic for spintronic applications.

Unfortunately, in spintronics application, TIs have a problem relating to their insulating nature. Because of their large band-gap and low carrier mobility, the conductivity σ of those TIs is limited to ~ $10^4\ \Omega^{-1}m^{-1}$, which is much lower than that of typical metallic ferromagnets (~ $6\times10^5\ \Omega^{-1}m^{-1}$) used in MRAM. This causes a serious problem for TIs as spin Hall materials. As illustrated in Figure 1.10(b), when attached to a metallic ferromagnet, most of the charge current is shunted through the recoding layer and does not contribute to generation of pure spin current in the spin Hall layer. Exploring new TI materials with both high conductivity and large spin Hall angle has been required.

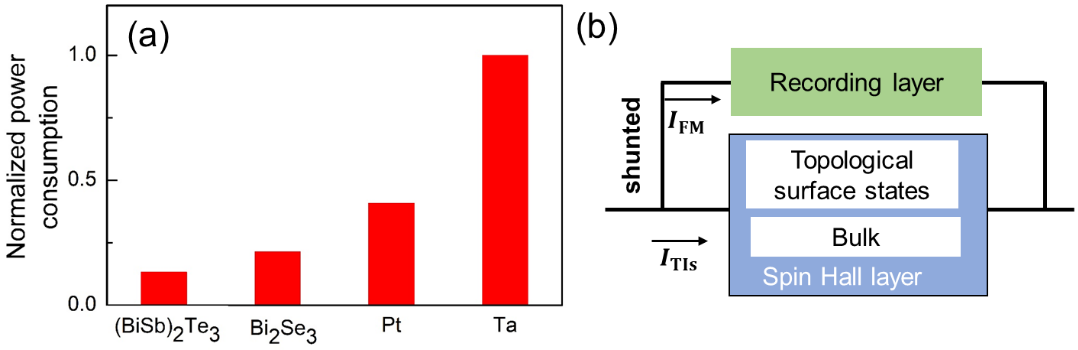

Figure 1.10: Normalized power consumption (with Ta set to be unity) for SOT switching using $(BiSb)_2Te_3$, Bi_2Se_3, Pt and Ta. Reproduced with permission [53]. (b) The shunting effect due to low electrical conductivity of TIs.

BiSb, a conductive TI

$Bi_{1-x}Sb_x$ ($0.07 \le x \le 0.22$) is a very narrow-gap TI [54]. Thanks to its high carrier mobility (~10^4 cmV^{-1}s^{-1}), its bulk conductivity is as high as 4×10^5~6.4×10^5 Ω^{-1}m^{-1}, compatible to other metallic materials used in realistic MRAM, as shown in Fig. 1.11(a). Recently, I and co-workers have developed epitaxial growth technique for high quality BiSb thin films using molecular beam epitaxy (MBE) [55] and obtained $\sigma = 4\times10^5$~6×10^5 Ω^{-1}m^{-1}for BiSb thin films thicker than 80 nm, and $\sigma=1\times10^5$~4×10^5 Ω^{-1}m^{-1} (average$\sigma \sim 2.5\times10^5$ Ω^{-1}m^{-1}) for BiSb thin films thinner than 25 nm in the TI region (0.07 $\le x \le$ 0.22).

On the other hand, BiSb shows strong SOI with topologically protected surface states as confirmed by ARPES [56, 57, 58] and shown in Fig. 1.11(b). These surface states were also confirmed by magneto-transport measurements [59, 60]. This promises the high charge-to-spin conversion efficient. From these reasons, BiSb emerges as the very promising candidate for spintronic applications.

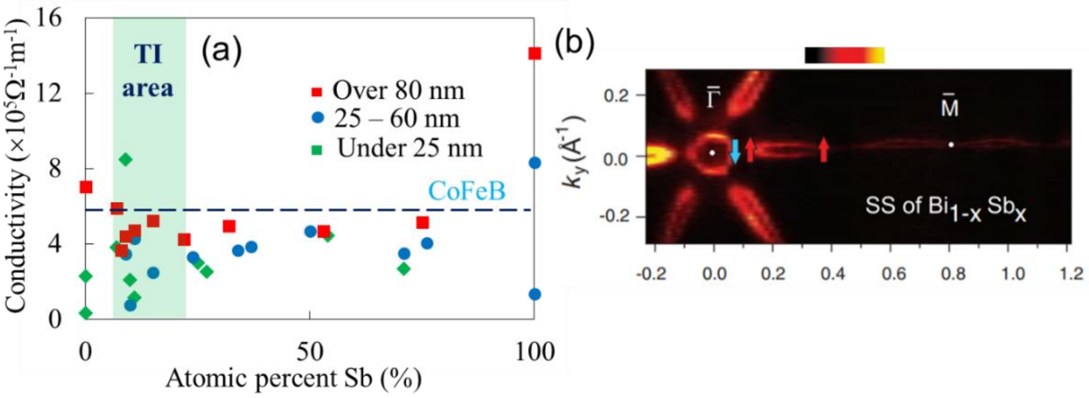

Figure 1.11: (a) Electrical conductivity at 270 K of various $Bi_{1-x}Sb_x$ samples with different Sb concentration and thickness. (b) Spin-integrated ARPES intensity map of the surface state of $Bi_{0.91}Sb_{0.09}$ at E_F. Arrows point in the measured direction of the spin. Reproduced with permission [55, 56].

1.5. Motivation

Because of the great interest of SOI-related effects in BiSb, it is my motivation to study various spin-related phenomena, including the SHE, the DMI and the unidirectional magnetoresistance (UMR), in BiSb-ferromagnet bilayers, as shown in Fig. 1. 12. These researches will not only provide useful information to deeply understand SOI-related effects in TIs but also open the pathway to improve the efficiency of spintronic memory and devices.

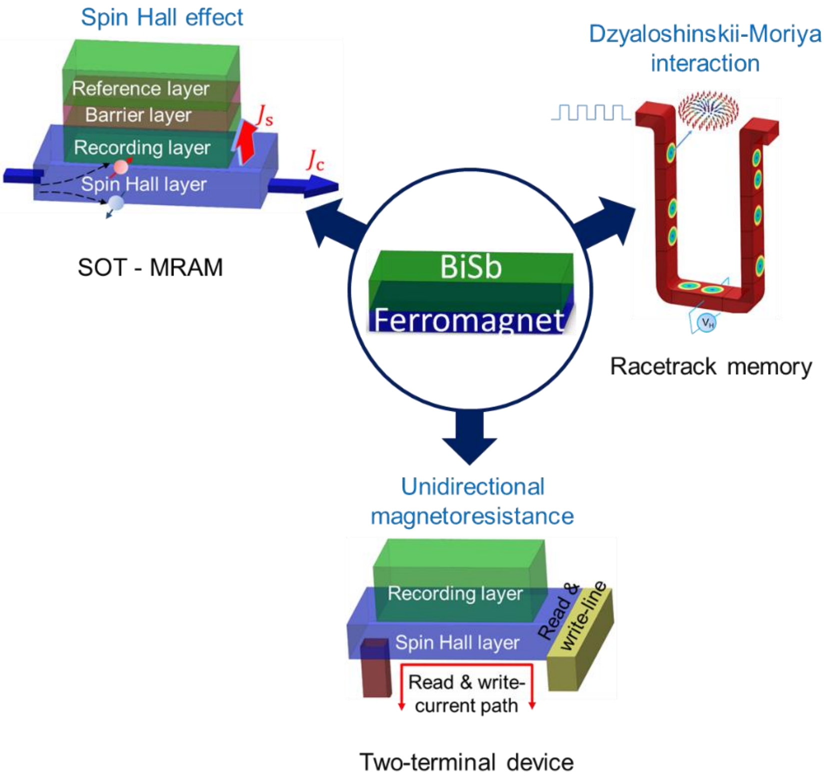

Figure 1.12: Spin-related phenomena in BiSb-ferromagnet bilayers and their applications to mainstream spintronic devices.

1.6. Thesis outline

My thesis is divided to 8 chapters.

Chapter 1 introduces the thesis background on spintronics in general, spintronic memory devices, recent evolution in spin-orbitronics, and topological insulators with emphasis on BiSb in particular. Based on these backgrounds, the motivation and thesis outline are described.

Chapter 2 presents the fundamental physics behind SOI-related phenomena, which are the main topic in this study.

Chapter 3 describes in details the experimental techniques used for sample preparation and characterization.

Chapter 4 focuses on the growth and characterization of MnGa thin films with perpendicular magnetic anisotropy on BiSb.

Chapter 5 describes the experiment results of the SHE in BiSb/MnGa bilayers.

Chapter 6 focuses on field-free ground-state skyrmions in BiSb/MnGa bilayers at room temperature revealed by the topological Hall effect (THE).

Chapter 7 presents the large UMR and its mechanism in GaMnAs/BiSb bilayers.

Chapter 8 summarizes the main results of this thesis and outlooks for future spintronic applications.

1.7. Summary

As the results of recent rapid developments in spintronics memory devices, spin-orbitronics appears as a novel concept that utilizes the SOI in spintronic memory devices. This makes spintronics not be restricted to conventional concepts of GMR, TMR or STT, and expand spintronics to much broader spectra where spin devices employ not only magnetic materials but also nonmagnetic materials with large SOI. Thus, efficient generation of pure spin current can be easily achieved by employing suitable spin source materials. As a consequence, spintronics researches have been shifted toward exploring the new materials with strong SOI and understanding their SOI-related effects. TIs and BiSb in particular appear as one of promising candidates for high efficient pure spin current source. Toward novel spintronic applications, further understanding of spin-related phenomena in bilayers of BiSb/ ferromagnetic material is the main purpose of this study.

References

1. J. Bardeen, and W. H. Brattain, Phys. Rev. **74**, 230 (1948).

2. G. E. Moore, Proc. IEEE **86**, 82 (1998).

3. G. E. Moore, IEEE S. S. Cir. Soc. News. **20**, 11 (2006).

4. S. A. Wolf, D. D. Awschalom, R. A. Buhrman, J. M. Daughton, S. von Molnár, M. L. Roukes, A. Y. Chtchelkanova, and D. M. Treger, Science **294**, 1488 (2001).

5. Akinaga, and H. Ohno, IEEE Trans. Nanotech. **1**, 19 (2002).

6. I. Žutić, J. Fabian, and S. D. Sarma, Rev. Mod. Phys. **76**, 323 (2004).

7. N. F. Mott, and H. H. Wills. Proc. R. Soc. A Math. Phys. Eng. Sci. **153**, 699 (1936).

8. N. F. Mott. Proc. R. Soc. A Math. Phys. Eng. Sci. **156**, 368 (1936).

9. I. A. Campbell, A. Fert, and A. R. Pomeroy, Philos. Mag. **15**, 977 (1967).

10. M. N. Baibich, J. M. Broto, A. Fert, F. Nguyen Van Dau, F. Petroff, P. Etienne, G. Creuzet, A. Friederich, and J. Chazelas, Phys. Rev. Lett. **61**, 2472 (1988).

11. Robert, E. Camley, and J. Barna´s, Phys. Rev. Lett. **63**, 664 (1989).

12. T. Valet, and A. Fert, Phys. Rev. B **48**, 7099 (1993).

13. B. Dieny, J. Magn. Magn. Mater. **136**, 335 (1994).

14. Randolph, Q. Hood, and L. M. Falicov, Phys. Rev. B **46**, 8287 (1992).

15. J. G. Zhu, and C. Park, Materialstoday **9**, 36 (2006).

16. K. Ono, N. Ohshima, K. Goto, H. Yamamoto, T. Morita, K. Kinoshita, T. Ishijima, and H. Toyoda, Jpn. J. Appl. Phys. **44**, L1442 (2005).

17. K. Tsunekawa, D.D. Djayaprawira, S. Yuasa, M. Nagai, H. Maehara, S. Yamagata, E. Okada, N. Watanabe, Y. Suzuki, K. Ando, IEEE Trans. Magn. **42**, 103 (2006).

18. B.N. Engel, N.D. Rizzo, J. Janesky, J.M. Slaughter, R. Dave, M. DeHerrera, M. Durlam, S. Tehrani, IEEE Trans. Nano. **1**, 32 (2002).

19. S. Tehrani, J.M. Slaughter, M. Deherrera, B.N. Engel, N.D. Rizzo, J. Salter,

M. Durlam, R.W. Dave, J. Janesky, B. Butcher, K. Smith, G. Grynkewich, Proc. IEEE **91**, 703 (2003).

20. J. C. Slonczewski, J. Magn. Magn. Mater. **159**, L1 (1996).

21. L. Berger, Phys. Rev. B **54**, 9353 (1996).

22. E. B. Myers1, D. C. Ralph, J. A. Katine, R. N. Louie, and R. A. Buhrman, Science **285**, 867 (1999).

23. R. Ramaswamy, J. M. Lee, K. Cai, and H. Yang, Appl. Phys. Rev. **5**, 031107 (2018).

24. S. V. Aradhya, G. E. Rowlands, J. Oh, D. C. Ralph, and R. A. Buhrman, Nano Lett. **16**, 5987 (2016).

25. K. Garello, C. O. Avci, I. M. Miron, M. Baumgartner, A. Ghosh, S. Auffret, O. Boulle, G. Gaudin, and P. Gambardella, Appl. Phys. Lett. **105**, 212402 (2014).

26. S. H. Yang, K. S. Ryu, and S. Parkin, Nat. Nanotechnol. **10**, 221 (2015).

27. S. S. P. Parkin, M. Hayashi, L. Thomas, Science **320**, 190 (2015)

28. J. S. Meena, S. M. Sze, U. Chand, and T. Y. Tseng, Nano. Re. Lett. **9**, 526 (2014).

29. Y. Ando, J. J. Appl. Phys. **54**, 070101 (2015).

30. M. Tsoi, A. G. M. Jansen, J. Bass, W. C. Chiang, M. Seck, V. Tsoi, and P. Wyder, Phys. Rev. Lett. **80**, 4281 (1998).

31. J. E. Wegrove, D. Kelly, P. Guitienne, Y. Jaccard, and J. P. Ansermet, Europhys. Lett. **45**, 626 (1999).

32. E. B. Myers, D. C. Ralph, J. A. Katine, R. N. Louie, and R. A. Buhrman, Science **285**, 867 (1999).

33. T. L. Gilbert, IEEE Tran. Magn. **40**, 3443 (2004).

34. V. M. Edelstein, S. S. Comm. **73**, 233 (1990).

35. A. Chernyshov, M. Overby, X. Liu, J. K. Furdyna, Y. L. Geller, and L. P, Nat. Phys., **5**, 656 (2009).

36. I. M. Miron, K. Garello, G. Gaudin, P. J. Zermatten, M. V. Costache, S. Auffret, S. Bandiera, B. Rodmacq, A. Schuhl, and P. Gambardella, Nature **476**, 189 (2011).

37. Y. K. Kato, R. C. Myers, A. C. Gossard, and D. D. Awschalom, Science **306**, 1910 (2004).

38. L. Liu1, C. F. Pai, Y. Li, H. W. Tseng, D. C. Ralph, R. A. Buhrman, Science **336**, 555(2012).

39. Q. Hao, and Xiao, Phys. Rev. Appl. **3,** 034009 (2015).

40. S. Fukami, C. Zhang, S. DuttaGupta, A. Kurenkov, H. Ohno, Nat. Mater. 15, 535 (2016).

41. Y. W. Oh, S. C. Baek, Y. M. Kim, H. Y. Lee, K. D. Lee, C. G. Yang, E. S. Park, K. S. Lee, K. W. Kim, G. Go, J. R. Jeong, B. C. Min, G.W. Lee, K. J. Lee, B. G. Park, Nat. Tech. **11**, 878 (2016).

42. K. U. Demasius, T. Phung, W. Zhang, B. P. Hughes, S. H. Yang, A. Kellock, W. Han, A. Pushp, and S. S. P. Parkin, Nat. Commun. **7**, 10644 (2016)

43. K. S. Ryu, L. Thomas, S. H. Yang, and S. Parkin. Nat. Nanotech. **8**, 527 (2013).

44. S. Emori, U. Bauer, S. M. Ahn, E. Martinez, and G. S. D. Beach. Nature Mater. 2, 611 (2013).

45. J. Torrejon, J. Kim, J. Sinha, S. Mitani, M. Hayashi, M. Yamanouchi, and H. Ohno, Nat. Commun., 5, 2014.

46. S. Mühlbauer, B. Binz, F. Jonietz1, C. Pfleiderer, A. Rosch, A. Neubauer, R. Georgii, P. Böni, Science **323**, 915 (2009).

47. W. Jiang, G. Chen, K. Liu, J. Zang, S. G.E. Velthuis, A. Hoffmann, Phys. Rep. **704**, 1 (2017).

48. C. O. Avci, “Current-induced effects in ferromagnetic heterostructures due to spin-orbit coupling”, PhD thesis, 7 (2015).

49. Y. Ando, J. Phys. Soc. J. **82**, 102001 (2013).

50. M. König, S. Wiedmann, C. Brüne, A. Roth, H. Buhmann, L. W. Molenkamp, X. L. Qi, and S. C. Zhang, Science **318**, 766 (2007).

51. A. R. Mellnik, J. S. Lee, A. Richardella, J. L. Grab, P. J. Mintun, M. H. Fischer, A. Vaezi, A. Manchon, E.-A. Kim, N. Samarth, and D. C. Ralph, Nature **511**, 449 (2014).

52. Y. Fan, P. Upadhyaya, X. Kou, M. Lang, S. Takei, Z. Wang, J. Tang, L. He, L. T. Chang, M. Montazeri, G. Yu, W. Jiang, T. Nie, R. N. Schwartz, Y. Tserkovnyak, and K. L. Wang, Nat. Mater. **13**, 699 (2014).

53. J. Han, A. Richardella, S. A. Siddiqui, J. Finley, N. Samarth, and L. Liu, Phys. Rev. Lett. **119**, 077702 (2017).

54. J. C. Y. Teo, L. Fu, C. L. Kane, Phys. Rev. B **78**, 045426 (2008).

55. Y. Ueda, N. H. D. Khang, K. Yao, P. N. Hai, Appl. Phys. Lett. **110**, 062401 (2017).

56. D. Hsieh, Y. Xia, L. Wray, D. Qian, A. Pal, J. H. Dil, J. Osterwalder, F. Meier, G. Bihlmayer, C. L. Kane, Y. S. Hor, R. J. Cava, and M. Z. Hasan, Science **323**, 919 (2009).

57. T. Hirahara, Y. Sakamoto, Y. Saisyu, H. Miyazaki, S. Kimura, T. Okuda, I. Matsuda, Phys. Rev. B. **81**, 165422 (2010).

58. A. Nishide, A. A. Taskin, Y. Takeichi, T. Okuda, A. Kakizaki, T. Hirahara, K. Nakatsuji, F. Komori, Y. Ando, and I. Matsuda, Phys. Rev. B **81**, 041309(R) (2010).

59. A. A. Taskin, and Y. Ando, Phys. Rev. B **80**, 085303 (2009).

60. A. A. Taskin, K. Segawa, and Y. Ando, Phys. Rev. B **82**, 121302 (R) (2010).

Chapter 2

Fundamental Physics of Spin-Orbit Interaction

In this chapter, overview of spin-orbit interaction will be presented as the key concept of many interesting phenomena observed in spintronics. As consequences of spin-orbit interaction, the spin Hall effect, the Dzyaloshinskii-Moriya interaction and the unidirectional magnetoresistance will be explained.

2.1. Spin-orbit interaction (SOI)

Spin-orbit interaction (SOI), also called as spin-orbit effect or spin-orbit coupling, is the concept describing the interaction between a particle's intrinsic angular momentum (spin) and its orbital degree of freedom. In the atomic regime, SOI is described in the picture of an electron motion around nucleus and its self-rotation. The orbiting of an electron around nucleus in the laboratory frame can be transferred to the orbiting of nucleus around the electron in the electron rest frame. As the results, the magnetic field B appearing in the rest frame of the electron can be expressed as

$$B = \frac{\mu_0 Zev}{4\pi r^2} \qquad \textbf{(2.1)}$$

where μ_0 is the permeability of free space, Ze and v are the charge and velocity of nucleus, respectively and r is the radius of nucleus motion. In the Lorentz transformation, the equation (2.1) is reformed as [1]

$$B = \frac{1}{2}\frac{E \times v}{c^2\sqrt{1 - v^2 / c^2}} \qquad \textbf{(2.2)}$$

where E is electric field, c is light velocity in free space.

Because the electron has a spin magnetic moment μ, it can interact with the magnetic field rising in the electron rest frame, and its energy E_{inter} is written as

$$E_{\text{inter}} = -\mu.B \tag{2.3}$$

This type of interaction is named as SOI. In the quantum mechanical description for the orbital angular momentum (L) and spin angular momentum (S) of the electron, SOI can be described by the following Pauli spin-orbit coupling term [2]

$$H_{SO} = \lambda L.S\, , \tag{2.4}$$

where λ is the SOC energy, $\hat{L}$ and $\hat{S}$ are the dimensionless operators of orbital angular momentum and spin angular momentum of the electron, respectively. As the consequence of SOI, the orbital degree of freedom can couple with the electron spin.

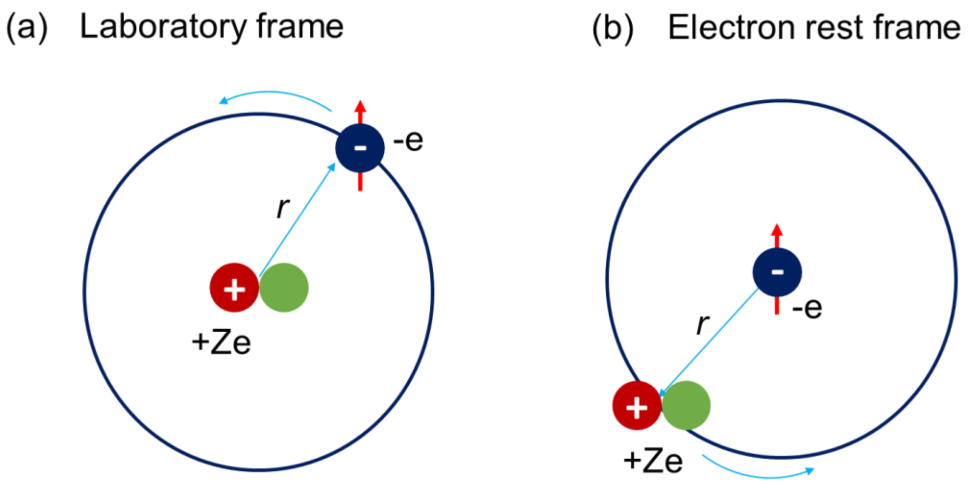

Figure 2.1: Schematic illustrations of (a) an electron orbiting around nucleus in the nucleus rest frame and (b) the nucleus orbiting around the electron in the electron rest frame. The electron in the rest frame of the electron feels the magnetic field B due to cyclic motion of the nucleus, while its spin is locked. This gives rise to the spin-orbit interaction.

2.2. Spin-orbit torque (SOT)

2.2.1. Spin current

Figure 2.2 illustrates one of the basic concepts of spintronics, the spin current. The flow of electrons will be merely a charge current, if their different directions of spins are mixed up and cannot be distinguished (Fig. 2.2(a)). However, there are situations that one spin population is larger than the other. The Figure 2.2(b) illustrates this kind of circumstance that the density of spin-up electrons is higher than the density of spin-down electrons. In this case, the charge current is accompanied by a spin current called "spin-polarized current". The net spin current will be the current of spin-up minus the current of spin-down.

More interestingly, Figure 2.2(c) shows a special case of spin current that the spin-up current flows to the right, while the spin-down current flows to the left. This situation makes the charge current, which is the total current of spin-up and spin-down in opposite direction, zero. In contrast, the net spin current is the sum of spin-up and spin-down current. This is called "pure spin current" [3] and poses new ideas about creating a spin current without a charge current.

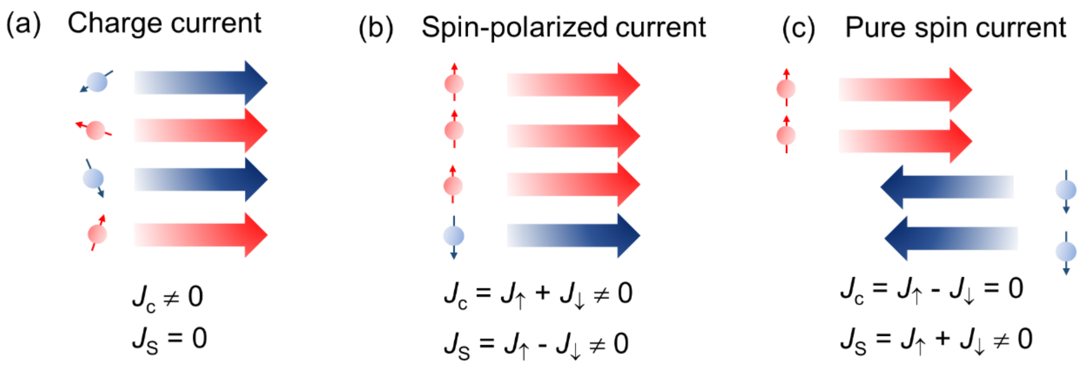

Figure 2.2: Schematic illustrations of (a) charge current, (b) spin-polarized current and (c) pure spin current.

So far, spin injection is a particular example of spin-polarized current generated by passing a charge current through a ferromagnetic layer, and can be directly applied to STT-MRAM. However, spin injection is limited by the maximum spin polarization P =

1 of the ferromagnetic layer. Recently, the Rashba-Edelstein effect or the spin Hall effect emerge as new ways to generate pure spin current with improved charge-to-spin conversion efficiency.

2.2.2. The Rashba-Edelstein effect

Under a broken inversion symmetry at the interface of NM/FM as shown in Fig. 2.3(a), an uncompensated electric field ***E*** appears along the ***z*** axis, and a conducting electron travelling with velocity ***v*** will experience an effective magnetic field ***B*** in the direction ***E***×***v***.

$$B = \gamma(v \times E) / c^2 \tag{2.5}$$

where $\gamma = 1/\sqrt{1 - v^2 / c^2}$ is the Lorentz factor. This field will couple to the electron spin, and its interaction can be expressed by the following Hamiltonian

$$H_R = \frac{\alpha_R}{\hbar}(E \times p)\sigma \tag{2.6}$$

where α_R is the Rashba parameter, $\hat{p}$ and $\hat{\sigma}$ are the momentum operator and electron spin operator, respectively. This type of interaction is named as the Rashba effect [4] originating from an interfacial SOI [5, 6, 7]. Under this situation, an in-plane current will be spin-polarized with the spin-polarization perpendicular to the current direction. This is called Rashba-Edelstein effect (REE) (Fig. 2.4).

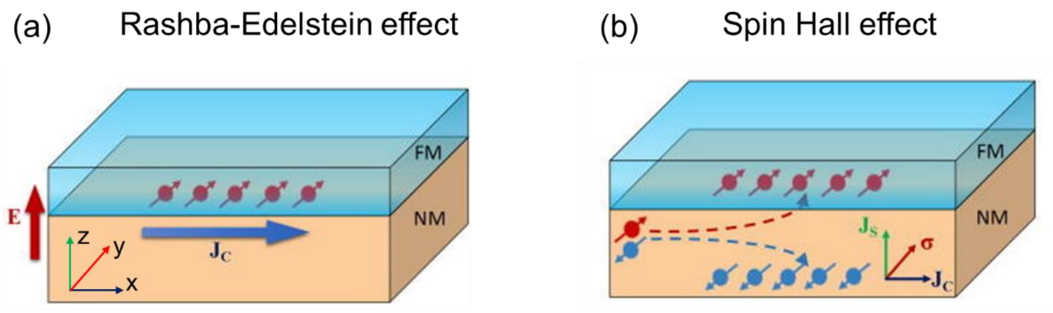

Figure 2.3: Schematic illustrations of (a) the Rashba-Edelstein effect and (b) the spin Hall effect. Reproduced with permission [8].

Figure 2.4 shows the spin redistribution under (a) the Rashba effect and (b) the Rashba-Edelstein effect with an electric current. The Rashba-Edelstein effect gives a non-equilibrium k-dependent spin polarization as the results of the electric field and scattering that leads to redistribution of carriers on the Fermi surface. The in-plane spin polarization is perpendicular to the direction of the charge current [9].

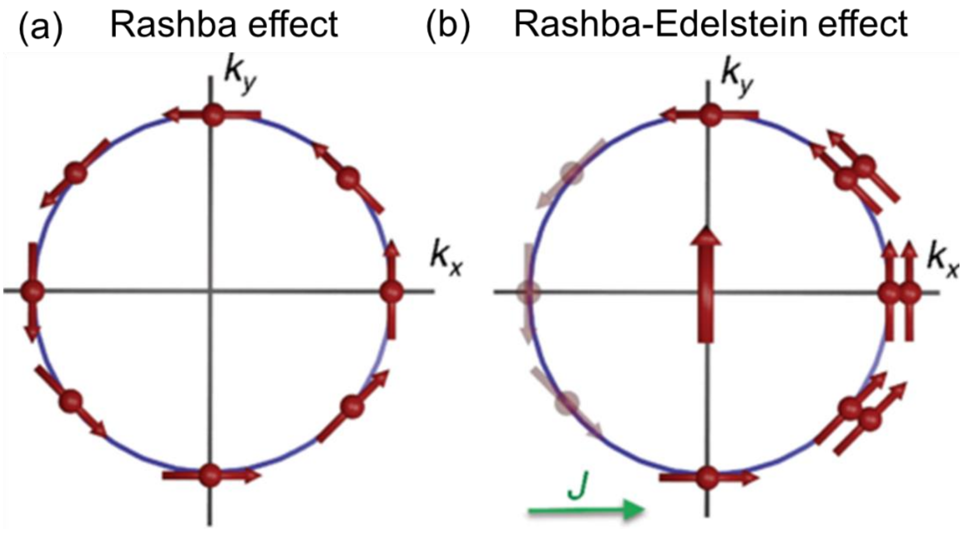

Figure 2.4: Schematic illustrates the microscopic picture of (a) the Rashba effect and (b) the Rashba-Edelstein effect. Reproduced with permission [9]

2.2.3. The spin Hall effect (SHE)

While the Rashba-Edelstein effect mainly exploits the interface SOI, a pure spin current can also arises inside NM thank to the bulk SOI. This effect is known as the spin Hall effect (SHE) with two main mechanisms: extrinsic mechanism (skew and side-jump scattering) and intrinsic mechanism (Berry phase of the band structure) [10, 11, 12]. Figure 2.3(b) illustrates the spin current generated from the spin Hall effect of NM. The direction of the spin polarization is perpendicular to the direction of the charge current.

The extrinsic contribution of SHE is from impurity SOI that leads to many spin-dependent scattering events. This SOI arises from the interaction between electrons with the electrostatic potential of the scatters $V(r)$ similar to the interaction between electrons with the Coulomb potential of nucleus in the atomic SOI. Therefore, this interaction can be expressed by the Hamiltonian

$$H_{scat} = \eta[\mathrm{k}\times V(r)]\sigma \qquad \textbf{(2.7)}$$

where η is the modified SOI parameter. The extrinsic contribution can be classified into skew-scattering or side-jump scattering. However, although the side-jump is classified as an extrinsic contribution, when addressing materials with strong SOI, the side-jump scattering is separated into two dependent sub-mechanisms: extrinsic side jump and intrinsic side jump. In the heavy metal such as Pt or Ta, intrinsic side jump is believed as the main contribution of SHE.

The contribution of SHE can also come from the Berry phase effect of the band structure (intrinsic contribution). This effect is first confirmed by observing polarized spin of GaAs though Kerr microscopy in 2004 [12, 13]. SHE from the bulk band structure due to strong SOI in TIs is also an example for the intrinsic contribution [14, 15,16].

In order to evaluate the intrinsic strength of SHE, the spin Hall angle θ_{SH} is defined

as

$$\theta_{\mathrm{SH}} = \frac{2e}{\hbar} J_s / J_c \tag{2.8}$$

where J_c is the charge current density, J_s is the spin current density. The magnitude of θ_{SH} gives the spin current generation efficiency in NM, and its sign defines the direction of spin accumulating at the in NM/FM interface.

If a pure spin current is created by a charge current by SHE, the reverse process can also happen and is called the inverse spin Hall effect (ISHE); that is, a charge current is generated by a spin current (Fig. 2.5). In general, the SHE can be considered as the concept borrowing from the well-established anomalous Hall effect (AHE) in ferromagnets. While a polarized transverse charge current is generated by a charge current in the case of AHE, a transverse pure spin current is generated in the case of SHE, and both of them arise from the same SOI mechanisms (Fig. 2.5). However, in contrast to AHE whose signal can be detected electrically in ferromagnet due to the difference between majority and minority spin population, the SHE required another ferromagnetic layer on which the spin current exerts a spin-orbit torque (SOT) that can be measured.

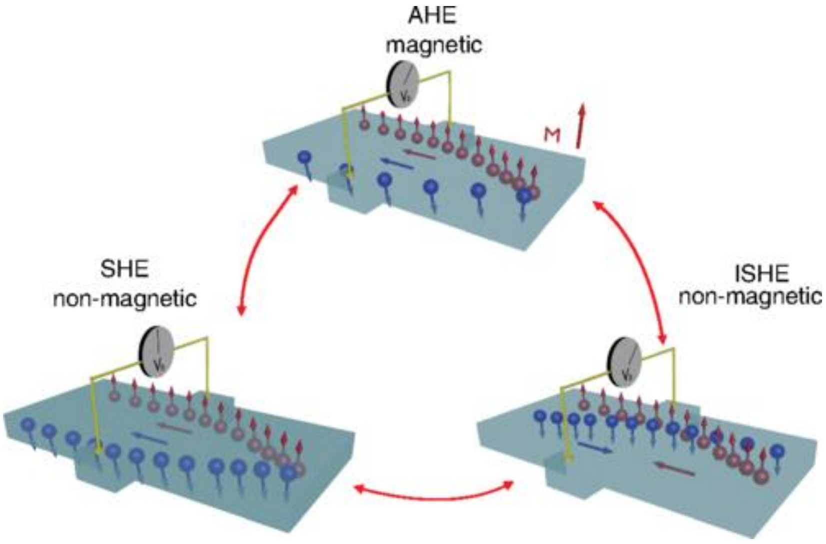

Figure 2.5: The schematic illustrates the connection between the anomalous Hall effect, the spin Hall effect and the inverse spin Hall effect. Reproduced with permission [9].

2.2.4. Spin orbit torque (SOT)

In NM/FM bilayers, spins can accumulate at the NM/FM interface and can exert an SOT on FM thanks to the REE or SHE. Depending on spin accumulation's mechanism, SOT (per unit moment) can be decomposed into two components, as shown in Fig. 2.6 [17, 18]:

(1) The field-like torque (FL) associated to Rashba-Edelstein effect can be written as

$$\tau_{\mathrm{FL}} = -m \times H_{FL} \qquad \textbf{(2.9)}$$

where H_{FL} is the field-like effective field ($H_{\mathrm{FL}}//\sigma$), and m is unit vector of FM magnetization.

(2) The antidamping-like torque (AD) associated to the SHE can be expressed by an antidamping-like effective field (H_{AD}) as following

$$\tau_{\mathrm{AD}} = -m \times H_{\mathrm{AD}} \qquad \textbf{(2.10)}$$

The antidamping-like effective field (H_{AD}) is given by

$$H_{\mathrm{AD}} = -\frac{\hbar}{2eM_{\mathrm{s}}t} J_{\mathrm{s}}(\sigma \times m) \qquad \textbf{(2.11)}$$

where σ is the spin polarization unit vector of the spin current, M_{s} and t are the saturation magnetization and thickness of FM, respectively.

Since both effects can generate SOT, classifying the contribution of these effects therefore, is necessary. There are many different techniques, such as spin torque ferromagnetic resonance (ST-FMR) [19, 20], differential planar Hall effect [21, 22] and harmonic voltage measurement [23, 24] that can be employed to evaluate their magnitudes.

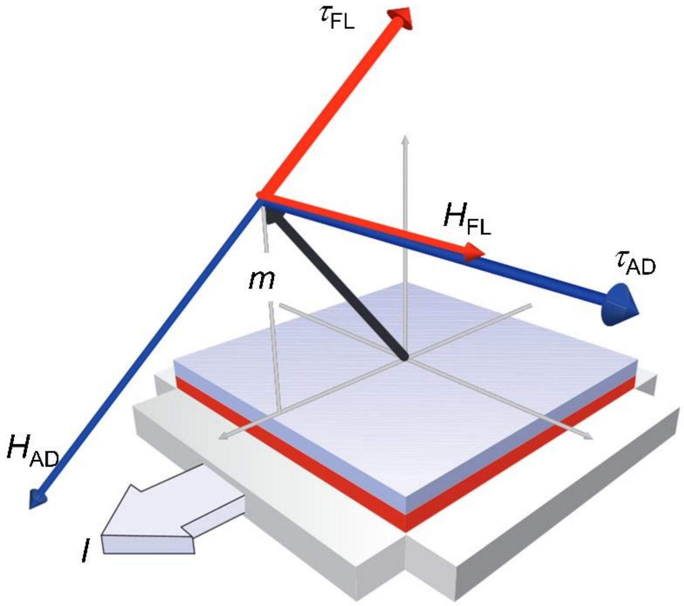

Figure 2.6: Schematic illustrates the field-like torque (FL) and antidamping-like torque (AD) with their respective effective field. Reproduced with permission [24].

2.3. The Dzyaloshinskii-Moriya interaction (DMI)

2.3.1. The Dzyaloshinskii-Moriya interaction (DMI)

In magnetic systems which lack inversion symmetry, SOI can combine with the exchange interaction to create the Dzyaloshinskii-Moriya interaction or antisymmetric exchange interaction which can be expressed by the following Hamiltonian

$$H_{DMI} = -D_{12}(S_1 \times S_2) \tag{2.12}$$

where D_{12} is the DMI characteristic vector, S_1 and S_2 are two neighboring atomic spins.

This type of interaction was discovered by I. Dzyaloshinskii in 1958 [25], and its mechanism based on SOI was completed by T. Moriya in 1960 [26]. The DMI can be classified into two types, as illustrated in Fig. 2.7: the bulk DMI and the interfacial DMI.

B20-type ferromagnets, such as MnSi, are examples of materials with bulk DMI. In these materials, the inversion symmetry is broken at each unit cell. This leads to the interplay of two atomic spins with a neighboring atom having strong SOI, and the DMI vector D_{12}, as a result, will point out of the film's plane. Comparing with the Heisenberg exchange interaction which prefers the parallel or antiparallel configuration, DMI energy is minimized when neighboring spins are perpendicular to each other. As a consequence, a finite angle between each atomic spin arises and plays as the origin of non-collinear spin textures, such as spin spirals, chiral magnetic domain walls, and skyrmions.

The domain wall energy with DMI can be expressed as [27]

$$\sigma = 4\sqrt{AK} - \pi D \qquad \textbf{(2.13)}$$

where A is the exchange constant, K is the anisotropy constant, and D is the DMI energy constant. In the normal case when D is small, the domain wall energy σ is positive. However, when D is large enough, σ can be negative and chiral domain walls emerge. If those chiral domain walls are rounded in space, they form skyrmions. However, skyrmions due to bulk DMI usually exist at low temperatures and need an external magnetic field to be stable.

The situation is little different for the interfacial DMI. Although the inversion symmetry can be maintained in each layer (FM or NM), it is broken at the interface of NM/FM. This makes two atomic spins in the FM layer exchange with a neighboring atom having strong SOI in the NM layer resulting in the interfacial DMI. The strength of DMI can be drastically enhanced by utilizing multilayers of NM/FM. DMI in these cases thus, can be strong and can compete with other exchange interactions even at room temperature. The domain wall energy will become zero or even negative leading to the turbulence of spin geometry mainly governed by the interfacial DMI.

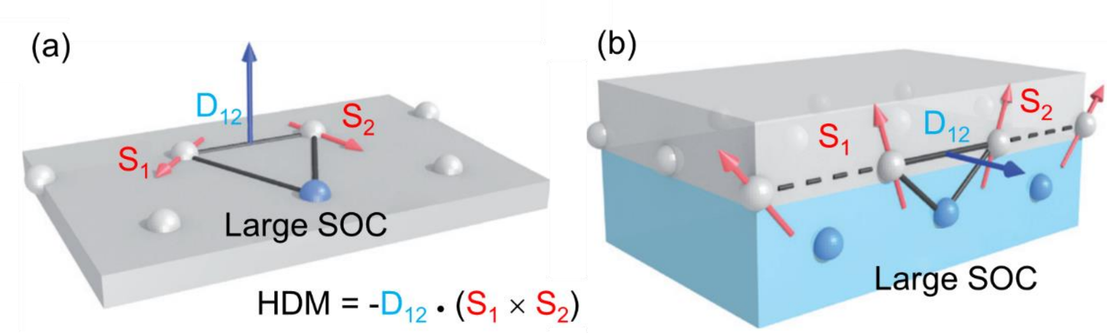

Figure 2.7: The schematic illustrations of (a) DMI generated by indirect exchange in a triangle composed of two atomic spins and an atom with strong SOC (bulk DMI) and (b) DMI generated by indirect exchange in a triangle composed of two atomic spins in ferromagnetic layer and an atom with strong SOC in the non-ferromagnetic layer (interfacial DMI). Reproduced with permission [28].

2.3.2. Skyrmion

Skyrmion or topologically protected spin texture is a key results of spin reconfiguration to minimize the system energy under strong DMI. The easiest way to evaluate skyrmion state is based on the skyrmion number *S* which can be written as

$$S = \frac{1}{4\pi}\int m \cdot \left(\frac{\partial m}{\partial x} \times \frac{\partial m}{\partial y} \right) dxdy \qquad \textbf{(2.14)}$$

where *m* is normalized magnetic vector. In one dimension, this function can be simplified as

$$S = \frac{1}{2\pi}\int \frac{\partial \theta}{\partial x} dx \qquad \textbf{(2.15)}$$

where θ is the angle between adjacent moments.

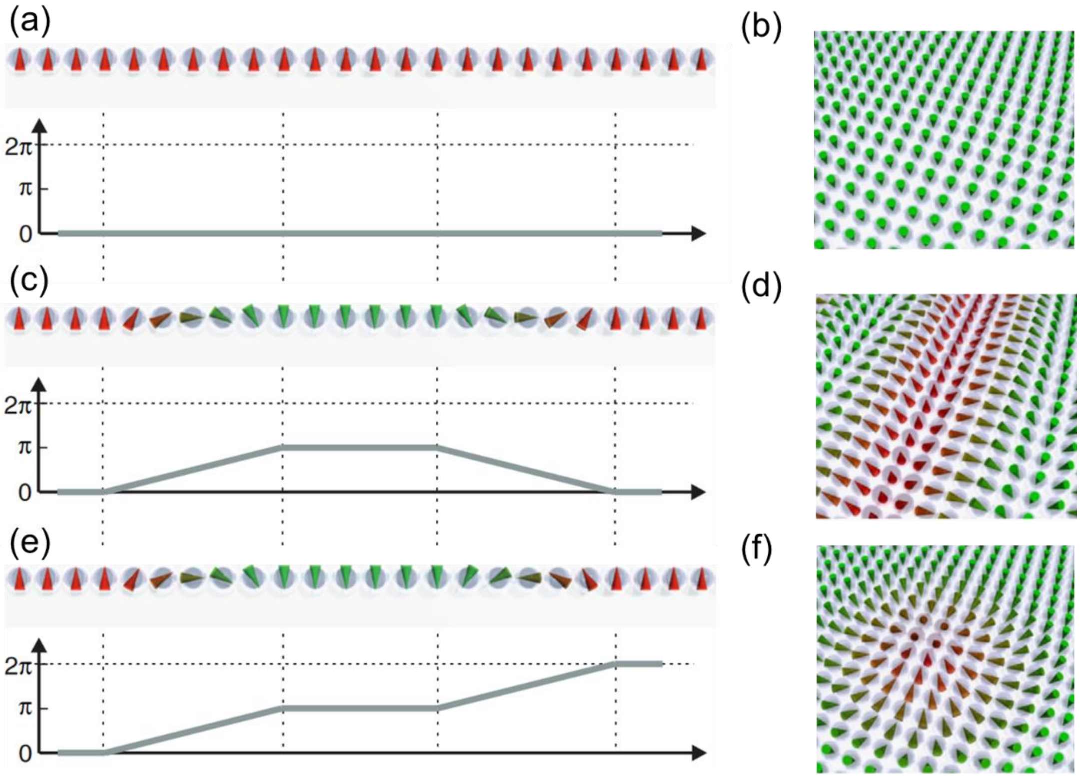

Figure 2.8: Skyrmion number in one-dimension (left side) and in two-dimension (right side) of (a-b) the ferromagnetic system, (c-d) the ferromagnetic system with two opposite domain walls and (e-f) the skyrmion system. Reproduced with permission [29].

Figure 2.8 illustrates the spin profile of three different magnetic sates in the one-dimension (left figure) and in two-dimension (right figure). In the ferromagnetic system, magnetization is homogeneous as illustrated by the gray line in the below graph, and the skyrmion number S is zero. The situation is same in the case of the ferromagnetic system with two opposite domain walls that cancels each other. However, the circumstance is completely different in the skyrmion state with two chiral domain walls, whose skyrmion number is non-zero ($S = 1$). Its inner domain can be shrunk but it is very hard to annihilate even by applying a magnetic field. This is known as topological protection, which means a small deformation of the system cannot change its spin structure. Moreover, skyrmions have small size (~5-80 nm [30, 31]) and can be moved with an ultra-low driving current density (~10^2 A/cm^2 [32]). Thus, skyrmions can enable the manipulation of information with high bit density and low power consumption. As a consequence, it has become very attractive candidate for the next generation magnetic memory, especially in racetrack memory.

2.3.3. Topological Hall effect (THE)

The non-collinear topological spin texture of skyrmions gives rise to an extra fictitious field. Interestingly, conduction electrons can also “feel” this fictitious field. In the Hall effect measurement, besides the ordinary Hall effect due to the Lorentz force and the anomalous Hall effect (AHE) driven by magnetization, there is an additional analogous component known as the topological Hall effect (THE) [33].

The THE resistivity can be phenomenologically expressed as

$$\rho_{\mathrm{THE}} = PR_0H_{\mathrm{fic}} \tag{2.16}$$

where P is the spin polarization, R_0 is the normal Hall coefficient, and H_{fic} is the fictitious magnetic field.

Comparing with other techniques of probing skyrmion, such as Lorentz transmission electron microscopy (TEM) [34] or X-ray microscopy [35], the THE has received a lot of attention due to its simplicity. The fictitious field is theoretically estimated around 1000 kOe for a 10-nm size skyrmion [36] and experimentally confirmed to be approximately 600 kOe [37].

2.4. The unidirectional magnetoresistance (UMR)

2.4.1. Magnetoresistance

In a perfect crystal at zero temperature, electrons move in the periodic potential of lattices and experience no collision. However, at temperature above zero with imperfection of crystal, electrons often collisions with other carriers or atoms and as the results, give rise to non-zero resistivity. The resistance of material also can be changed by applying a magnetic field (Lorentz force) or by spin-disorder scattering that originates from the *s*, *p*-*d* exchange interactions in magnetic materials. Magnetoresistance (MR) is named as a result of the dependence of resistance on the external magnetic field.

The Lorentz force mechanism occurs in both ferromagnetic and paramagnetic materials because of the electron's cyclotron motion under external magnetic field. On the other hand, the spin-disorder MR arises from suppression of the electron-magnon scattering at high external magnetic field. This mechanism therefore, occurs only in ferromagnets. In addition, there is another MR effect, whose magnitude depends on the relative orientation between the magnetization direction and the current called anisotropic magnetoresistance (AMR). Figure 2.9 illustrates the microscopic origin of AMR. Its origin can be simply considered as a results of SOI and reorientation of the atomic orbitals. The AMR resistivity ρ_{xx} can be expressed as

$$\rho_{\mathrm{xx}} = \rho_{\perp} + (\rho_{\parallel} - \rho_{\perp})\sin^2\theta\cos^2\varphi \qquad \textbf{(2.17)}$$

where $\rho_{\perp}$ and $\rho_{\perp}$ are the resistivity when magnetization *M* is perpendicular and parallel with current direction, respectively, θ and φ are the polar and azimuthal angle of magnetization direction.

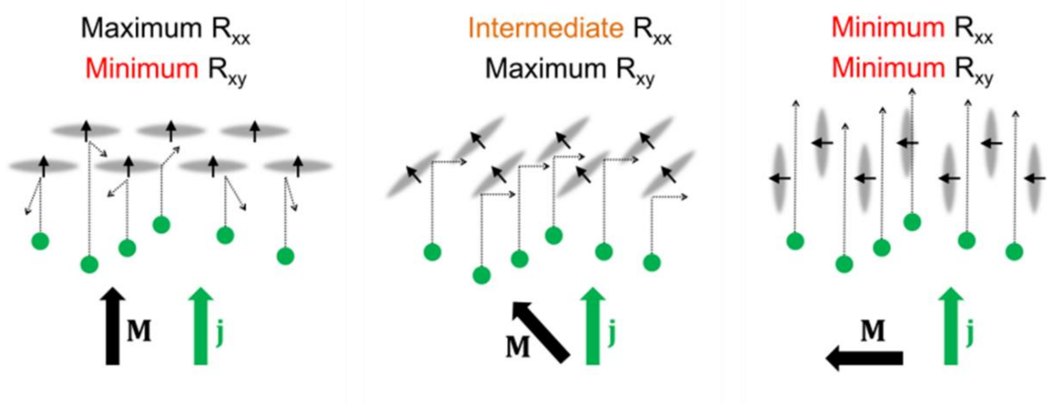

Figure 2.9: Schematic illustrates the microscopic of anisotropic magnetoresistance (AMR). The changing of atomic orbital's shape changes the number of scattering between electron and atom. Reproduced with permission [38].

2.4.2. The spin Hall magnetoresistance (SMR)

The MR effect becomes much more interesting in bilayers of a paramagnetic material with strong SOI and a ferromagnetic material. One example is the spin Hall magnetoresistance (SMR), as shown in Fig. 2.10. The spin current created by SHE in the NM layer accumulates at the interface of NM/FM. Depending on the relative direction between the polarization direction of spins at interface and the magnetization direction in the FM layer, the spin current is partly absorbed in the FM layer, and the rest of spin current will be reflected back to NM layer. This backflow of spin current generates an electric current by the inverse spin Hall effect (ISHE), which contributes to the longitudinal current and gives rise to the SMR. Since the SMR effect originates from the backflow of spins, its magnitude can be enhanced by using insulator ferromagnets, such as the yttrium iron garnet (YIG) [39].

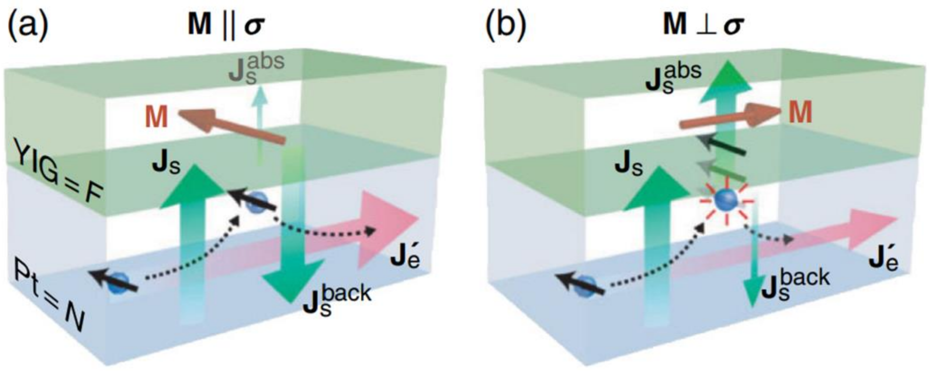

Figure 2.10: Illustration of spin Hall magnetoresistance as the result of the backflow of the spin current and the inverse spin Hall effect when (a) magnetization aligns with polarization of spin current, (b) magnetization is perpendicular with the polarization of spin current. Reproduced with permission [39].

2.4.3. The unidirectional magnetoresistance (UMR)

Recently, there is a new effect relating to an unusual behavior of MR occurring in FM/NM system such as Co/Pt or Co/Ta [40] named as unidirectional magnetoresistance (UMR). This effect poses the features of the GMR effect that the spin accumulation at the interface of FM/NM can be considered as an FM layer. However, unlike the GMR effect and the SMR effect, the dependence of resistance on the charge current in UMR is nonlinear. In the metallic bilayers, such as Co/Pt, UMR is classified into two types [41]: spin-dependent scattering and magnon scattering mechanism as shown in the Fig. 2.11. In the first mechanism, a pure spin current generated from the SHE or REE is injected to FM layer and accumulates at the near interface. A GMR-like UMR signal is generated as the result of the spin transmission and reflection depending on direction of the spin polarization σ and magnetization M. The second mechanism on the other hand, comes from the spin-disorder scattering generated from absorption or emission of magnon, a quantized spin wave in ferromagnets as illustrated in Fig. 2.12.

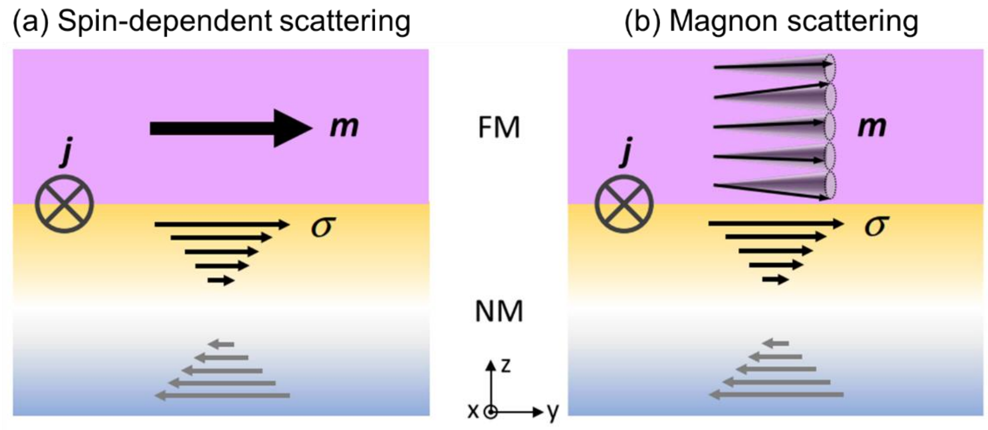

Figure 2.11: The schematic illustrates (a) the spin-dependent scattering mechanism and (b) the magnon scattering mechanism. Reproduced with permission [41].

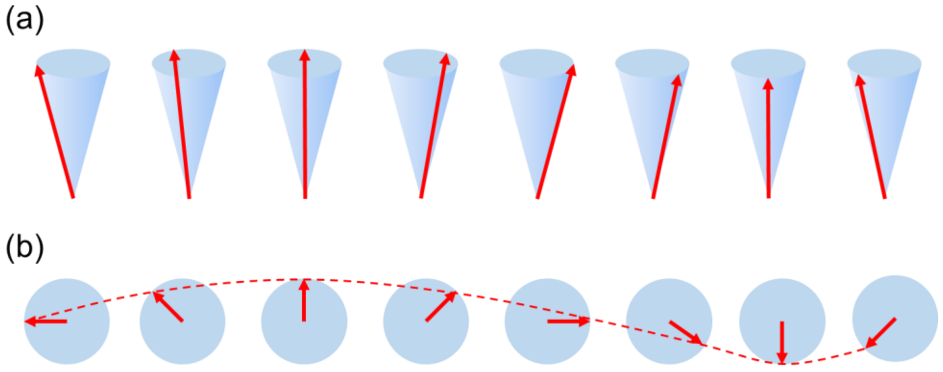

Figure 2.12: The schematic illustrates the simple picture of magnon in (a) side view and (b) top view.

UMR not only provides useful information that shed light on the SOI properties but also plays as a new method to detect the magnetization direction. By utilizing UMR for readout, the reference layer and the tunnel barrier in SOT-MRAM can be completely omitted. Thus, UMR can greatly simplify the structure of SOT-MRAM.

2.5. Summary

In this chapter, the concept of SOI and related effects, such as the Rashba-Edelstein effect, the spin Hall effect, etc. were introduced. Each of them gives spintronics (spin-orbitronics in particular) novel ideas that can improve or even completely change spintronic device technologies. For example, the SHE can improve the power consumption, the writing speed, and the bit density in STT-MRAM. The THE can help detect skyrmions for the racetrack memory, and UMR can be employed to greatly simply the structure of SOT-MRAM devices. Further study to fully understand their characteristics as well as enhance their performances, especially in new materials, play a vital role. For this reason, study of spin-related phenomena in BiSb-ferromagnet bilayers is the main topic in the rest parts of this thesis.

References

1. L. H. Thomas, Nature **117**, 514 (1926).

2. J. M. D. Coey, Cam. Uni. Pre. **3**, 66 (2010).

3. Y. Ando, J. J. Appl. Phys. **54**, 070101 (2015).

4. V. M. Edelstein, Solid State Commun. **73**, 233 (1990).

5. G. Dresselhaus, Phys. Rev. **100**, 580 (1955).

6. Yu. A. Bychkov, and E. I. Rashba, JETP Lett. **39**, 78 (1984).

7. A. Manchon, H. C. Koo, J. Nitta, S. M. Frolov, and R. A. Duine, Nat. Mater. 14, 871 (2015).

8. R. Ramaswamy, J. M. Lee, K. Cai, and H. Yang, Appl. Phys. Rev. **5**, 031107 (2018).

9. J. Sinova, S. O. Valenzuela, J. Wunderlich, C. H. Back, T. Jungwirth, Rev. Mod. Phys. **87**, 1213 (2015).

10. M. I. Dyakonov, and V. I. Perel, Phys. Lett. A **35**, 459 (1971).

11. J. E. Hirsch, Phys. Rev. Lett. **83**, 1834 (1999).

12. Y. K. Kato, R. C. Myers, A. C. Gossard, and D. D. Awschalom, Science **306**, 1910 (2004).

13. J. Sinova, and T. Jungwirth, Phys. Today **70**, 38 (2017).

14. D. Hsieh, Y. Xia, L. Wray, D. Qian, A. Pal, J. H. Dil, J. Osterwalder, F. Meier, G. Bihlmayer, C. L. Kane, Y. S. Hor, R. J. Cava, and M. Z. Hasan, Science **323**, 919 (2009).

15. T. Hirahara, Y. Sakamoto, Y. Saisyu, H. Miyazaki, S. Kimura, T. Okuda, I. Matsuda, Phys. Rev. B. **81**, 165422 (2010).

16. N. H. D. Khang, Y. Ueda, and P. N. Hai, Nat. Mater. **17**, 808 (2018).

17. K. W. Kim, S. M. Seo, J. Ryu, K.-J. Lee, and H. W. Lee, Phys. Rev. B **85**, 180404 (2012).

18. P. M. Haney, H. W. Lee, K.-J. Lee, A. Manchon, and M. D. Stiles, Phys. Rev. B **87**, 174411 (2013).

19. L. Q. Liu, T. Moriyama, D. C. Ralph, and R. A. Buhrman, Phys. Rev. Lett. **106**, 036601 (2011).

20. A. R. Mellnik, J. S. Lee, A. Richardella, J. L. Grab, P. J. Mintun, M. H. Fischer, A. Vaezi, A. Manchon, E. A. Kim, N. Samarth, and D. C. Ralph, Nature **511**, 449 (2014).

21. M. Kawaguchi, K. Shimamura, S. Fukami, F. Matsukura, H. Ohno, T. Moriyama, D. Chiba, and T. Ono, Appl. Phys. Exp. **6**, 113002 (2013).

22. M. Jamali, Z. Zhao, DC. Mahendra, D. Zhang, H. Li, A. K. Smith, and J. P. Wang, J. Appl. Phys. 119, 133902 (2016).

23. J. Kim, J. Sinha, M. Hayashi, M. Yamanouchi, S. Fukami, T. Suzuki, S. Mitani, and H. Ohno, Nat. Mater. **12**, 240 (2013).

24. K. Garello, I. M. Miron, C. O. Avci, F. Freimuth, Y. Mokrousov, S. Blugel, S. Auffret, O. Boulle, G. Gaudin, and P. Gambardella, Nat. Nanotechnol. **8**, 587 (2013).

25. I. Dzyaloshinskii, J. Phys. Chem. Solids **4**, 241 (1958).

26. T. Moriya, Phys. Rev. **120**, 91 (1960).

27. S. Rohart, and A. Thiaville, Phys. Rev. B **88**, 184422 (2013).

28. A. Fert, V. Cros, and J. Sampaio, Nat. Nanotech. **8**, 152 (2013).

29. K. Bergman, A. Kubetzka, O. Pietzsch, and R. Wiesendanger, J. Phys. Condens. Matter. **26**, 394002 (2014).

30. G. Chen, A. Mascaraed, A.T. N'Diaye, A.K. Schmid, Appl. Phys. Lett. **106**, 242404 (2015).

31. O. Boulle, J. Vogel, H. Yang, S. Pizzini, D. de Souza Chaves, A. Locatelli, T.O. Mentes, A. Sala, L.D. B. Prejbeanu, O. Klein, M. Belmeguenai, Y. Roussigne, A.

Stashkevich, S.M. Cherif, L. Aballe, M. Foerster, M. Chshiev, S. Auffret, I.M. Miron, G. Gaudin, Nat. Nanotechnol. **11**, 449 (2016).

32. F. Jonietz, S. Mühlbauer, C. Pfleiderer, A. Neubauer, W. Münzer, A. Bauer, T. Adams, R. Georgii, P. Böni, R. A. Duine, K. Everschor, M. Garst, A. Rosch, Science **17**, 1648 (2010).

33. A. Neubauer, C. Pfleiderer, B. Binz, A. Rosch, R. Ritz, P. G. Niklowitz, and P. Bo¨ni, Phys. Rev. Lett. 102, 186602 (2009).

34. W. Wang, Y. Zhang, G. Xu, L. Peng, B. Ding, Y. Wang, Z. Hou, X. Zhang, X. Li, E. Liu, S. Wang, J. Cai, F. Wang, J. Li, F. Hu, G. Wu, B. Shen, and X. X. Zhang, Adv. Mat. **28**, 6887 (2016).

35. K. Litzius, I. Lemesh, B. Krüger, P. Bassirian, L. Caretta, K. Richter, F. Büttner, K. Sato, O. A. Tretiakov, J. Förster, R. M. Reeve, M. Weigand, I. Bykova, H. Stoll, G. Schütz, Geoffrey, S. D. Beach, and M. Kläui, Nat. Phys. **13**, 170 (2017).

36. P. Bruno, V.K. Dugaev, and M. Taillefumier, Phys. Rev. Lett. **93**, 096806 (2004).

37. K. K. Meng, X. P. Zhao, P. F. Liu, Q. Liu, Y. Wu, Z. P. Li, J. K. Chen, J. Miao, X. G. Xu, J. H. Zhao, and Y. Jiang, Phys. Rev. B **97**, 060407 (2018).

38. C. O. Avci, “Current-induced effects in ferromagnetic heterostructures due to spin-orbit coupling”, PhD thesis, 7 (2015).

39. H. Nakayama, M. Althammer, Y. T. Chen, K. Uchida, Y. Kajiwara, D. Kikuchi, T. Ohtani, S. Gepra¨gs, M. Opel, S. Takahashi, R. Gross, G. E. W. Bauer, S. T. B. Goennenwein, and E. Saitoh, Phys. Rev. Lett. **110**, 206601 (2013).

40. C. O. Avci, K. Garello, A. Ghosh, M. Gabureac, S. F. Alvarado, and P. Gambardella, Nat. Phys. **11**, 570 (2015).

41. C. O. Avci, J. Mendil, G. S. D. Beach, and P. Gambardella, Phys. Rev. Lett. **121**, 087207 (2018).

Chapter 3

Sample Preparation and Characterization Techniques

In this chapter, fabrication and characterization techniques of BiSb-ferromagnet bilayers will be described in details. Section 3.1 gives details of sample preparation's procedure, and the characterization as well as experimental setup will be shown in Section 3.2.

3.1. Sample preparation

3.1.1. Molecular beam epitaxy (MBE)

In order to fabricate high quality BiSb-ferromagnet bilayers, the molecular beam epitaxy (MBE) was employed in this study for sample preparation. MBE is a crystal growth technique that can grow atomic layer by atomic layer in an ultra-high vacuum (UHV) condition and based on reaction of molecular (or atomic beam) with a heated substrate [1]. Here, the term "epitaxy" describes the ordered growth of crystalline layers. Unlike other crystal-growth methods, MBE allows to fabricate samples with precise composition, high purity and real-time monitoring. As a consequence, MBE can produce samples with extremely high crystal quality, and is employed to grow metals, insulators or semiconductors with sharp interfaces and precise composition.

Figure 3.1 shows the schematic illustration of the growth chamber of a MBE system (Fig. 3.1(a)) and the real image of the Anelva MBE-620 system used in my study (Fig. 3.1(b)). The UHV (~10^{-7} Pa) in this MBE was achieved by employing an ion pump, an Ti-sublimation pump and a liquid nitrogen shroud to prevent atom's re-evaporation. The samples, mounted to molybdenum holders by indium, were loaded to the growth chamber by a transfer rod. The samples were heated by a resistance-type heater and their temperature was controlled by thermal couple feedback. The grown materials (Ga, As, Bi, Sb and Mn) were stored in Knudsen cells (or K-cells) and deposited on sample's substrate by heating the materials to given temperatures.

Reflection high-energy electron diffraction (RHEED)

The layer-by-layer growth also permits real-time *in situ* surface observation by RHEED [2, 3]. The electrons emitted from a heated tungsten filament are accelerated to high speed and energy (~20 – 23 keV), strike and diffract on the sample's surface at a grazing angle of less than a few degree, and form the RHEED patterns on a fluorescent screen. From the position and shape of the streaks in the RHEED patterns, the information of surface crystallography such as the surface orientation and the surface roughness can be observed in real-time. RHEED as the results, has become an indispensable tool in MBE systems.

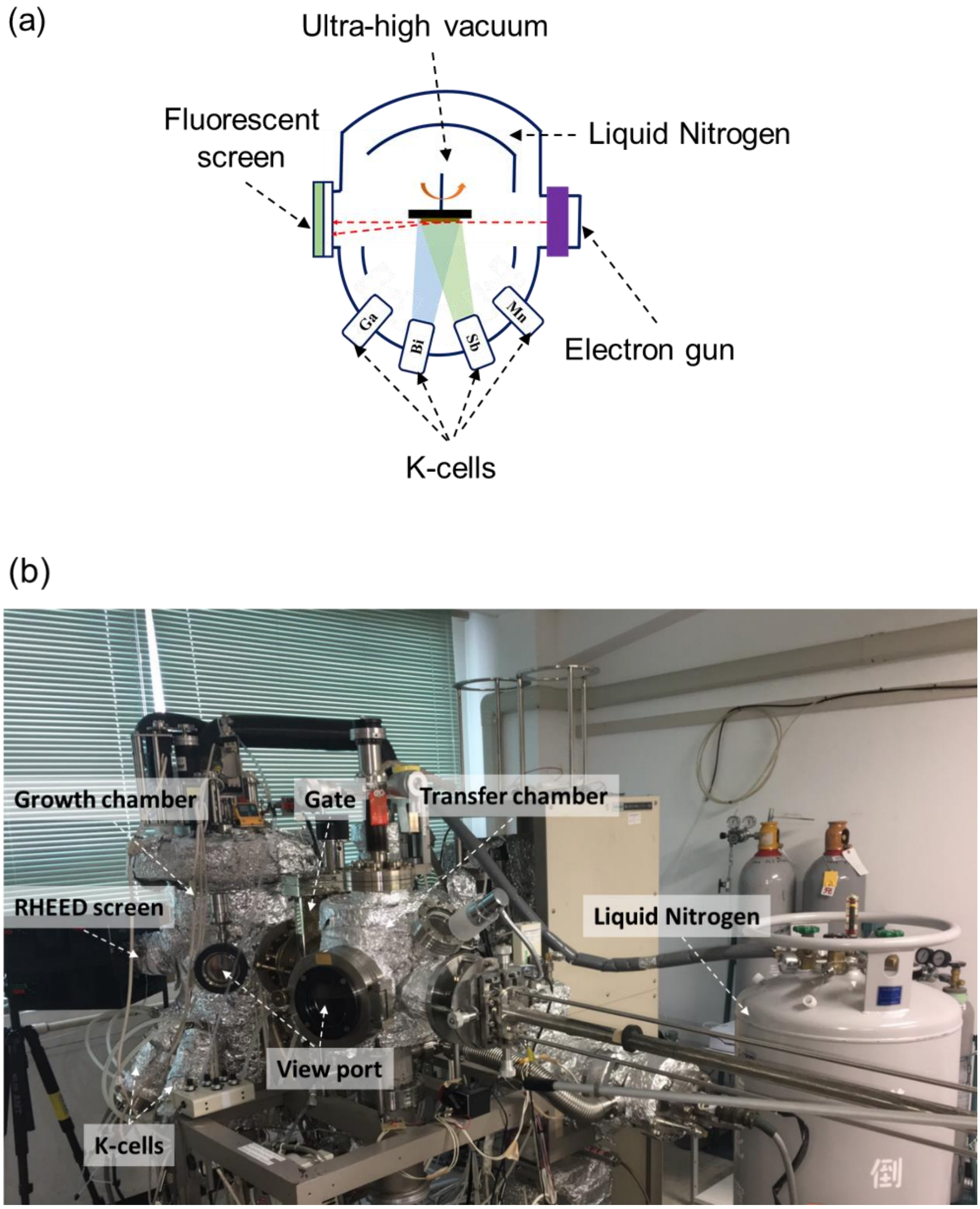

Figure 3.1: (a) Schematic illustration of the growth chamber of a MBE system. (b) Photograph of the Anelva MBE-620 system used in this work.

GaAs buffer layer's preparation

Because the surface condition of the starting crystal (substrate) plays a vital role in epitaxial growth by MBE, preparing the substrate surface with high crystal quality is necessary in my experiments. The GaAs substrates were used for all fabricated samples, and the substrate preparation is described as follows

(1) Heat the GaAs substrates from 150^{o}C to 580^{o}C at a ramping rate of 20^{o}C/min to remove the oxidized layer ($GaAsO_3$ and $GaAsO_4$ [4]) (Fig. 3.2(a) and Fig. 3.2(d)).

(2) Keep GaAs at 580^{o}C under As exposure to completely remove oxidized layer and compensate the lost As atoms from the substrate (Fig. 3.2(b) and Fig. 3.2(e)).

(3) Grow a thick GaAs film (~ 80 – 100 nm) until high quality of GaAs surface was confirmed (Fig. 3.2(c) and Fig. 3.2(f)).

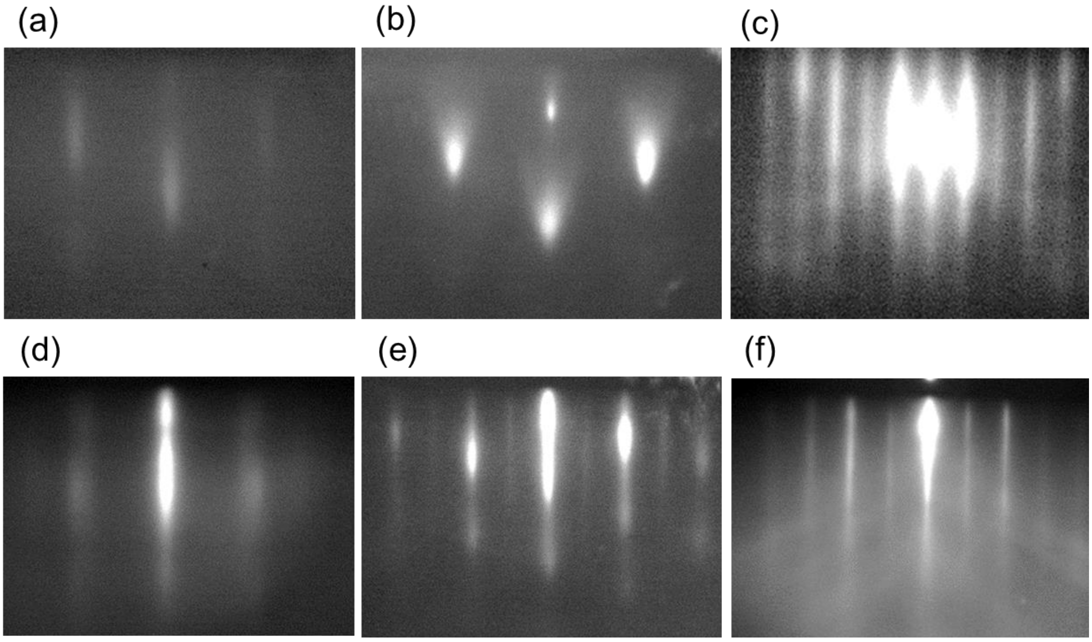

Figure 3.2: RHEED patterns of a GaAs(001) substrate taken along $[\bar{1}10]$ azimuth (a) before deoxidation, (b) after deoxidation, and after growing a thick buffer GaAs layer. (d-f) same as (a-c) but for a GaAs(111)A substrate.

3.1.2. Hall bar device fabrication

For the electrical measurement, Hall bar devices were fabricated with the process shown in Fig. 3.3.

(1) In the first step, the Hall bar pattern, made from a positive photoresist (OFPR) mask was formed on the sample's surface by conventional photolithography process. After milling process (Ar^+ ion), the photoresist mask was removed by gentle ultrasonic cleaning in warm acetone. The Hall bars with size of 100 μm × 50 μm or 100 μm × 25 μm were fabricated as shown in Fig. 3.4(a).

(2) In the second step, the electrode mask, made from OFPR was formed on the sample's surface by the same photolithography process. After that, Cr (5 nm)/Au (50~150 nm) bilayers were deposited on the sample by electron-beam evaporation. Finally, the electrode was obtained by lift off as shown in Fig. 3.4(b).

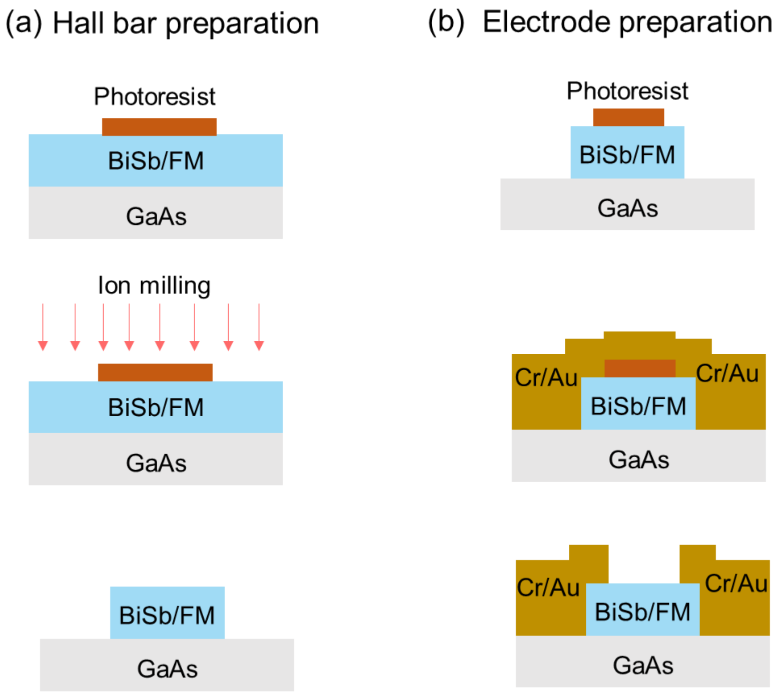

Figure 3.3: Schematic illustrates (a) Hall bar preparation and (b) electrode preparation for a Hall bar device.

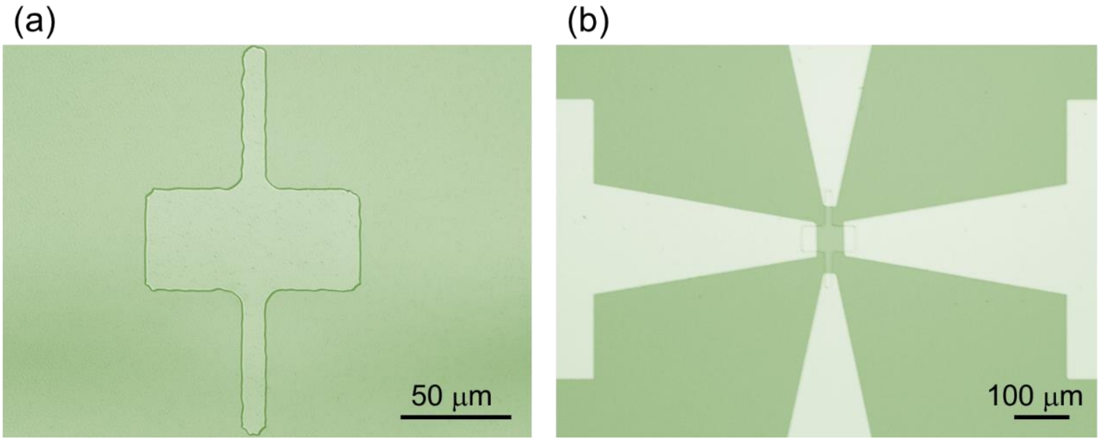

Figure 3.4: (a) Micrograph of a 100 μm × 50 μm Hall bar after the milling process. (b) Final device after deposition of a Cr (5 nm)/Au (50 nm) pad for the contact electrodes.

3.2. Characterization techniques

3.2.1. X-ray diffraction (XRD) measurement

To evaluate the crystal characteristics, X-ray diffraction (XRD), a non-destructive technique for analyzing material's structure, was employed. As its name implies, XRD is based on diffraction of X-rays that are irradiated toward the sample. The XRD peak positions satisfy the Bragg' law (Fig. 3.5(a)):

$$2d\sin\theta = k\lambda \tag{3.1}$$

where d is the distance between diffraction planes, λ and θ are the wavelength (λ = 0.15406 nm for Kα1 of Cu) and its incident angle, respectively, and k is an integer (k = 1, 2, 3,…).

The 2θ scanning (Fig. 3.5(a)) measures the dependence of the XRD intensity on θ and gives the basic information of the sample's crystal characteristics. For the detailed crystal characterization, ϕ-χ scanning (Fig. 3.5(b)) is used. By measuring the XRD intensity at each ϕ and χ value, the crystallography of sample can be determined.

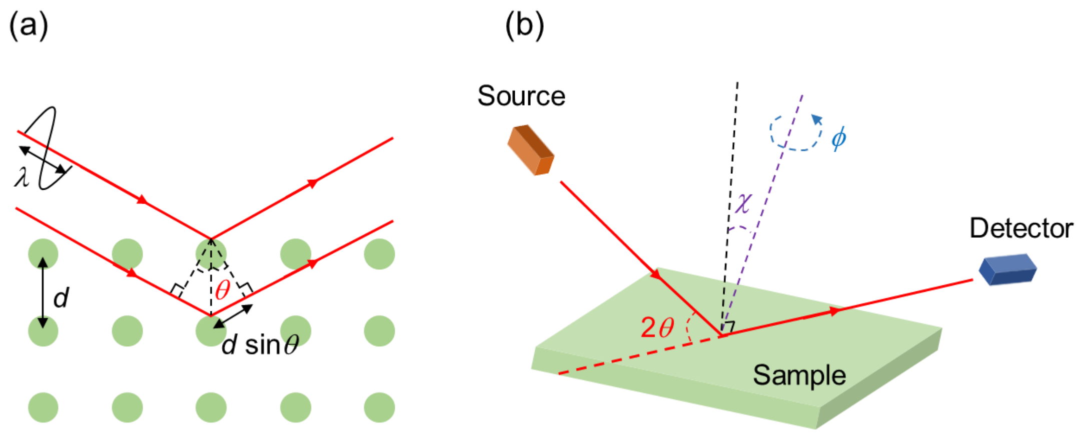

Figure 3.5: (a) Illustration of the Bragg equation. (b) Schematic of XRD measurement setup (2θ scanning and ϕ-χ scanning).

3.2.2. Magnetotransport measurement

Sample characterization by magnetotransport measurement is an indispensable step for all topics of spin-related phenomena in BiSb/FM bilayers. Fig. 3.6 (a) illustrated the schematic setup of Hall measurement, and its actual experiment setup is shown in Fig. 3.6(b). In these measurements, the samples are biased with a DC current (or a pulse current), and the V_{xx} or V_{xy} signal are measured by voltmeters under a magnetic field. Moreover, for the measurements at low temperatures, the samples were cooled down by a cryogenic system. There are three types of magnetotransport measurement performed in my study:

(1) Hall effect measurement

This measurement was employed in order to detect the normal Hall effect as well as the anomalous Hall and the topological Hall effect. The DC current was applied in the longitudinal direction, and the transverse V_{xy} voltage was detected as the output signal.

The Hall resistivity ρ_H can be expressed as

$$\rho_H = \rho_{\mathrm{O}} + \rho_{\mathrm{AHE}} = R_{\mathrm{O}} H_{\mathrm{eff}} + R_{\mathrm{AHE}} M \tag{3.2}$$

where ρ_{O} is the ordinary Hall resistivity, ρ_{AHE} is the anomalous Hall resistivity, R_{O} and R_{AHE} are the coefficient of the ordinary Hall and anomalous Hall effects, respectively, H_{eff} is the effective magnetic field, and M is the sample's magnetization. For the SOT switching in BiSb/MnGa bilayers, pulse currents (τ = 100 ms) were applied. The final state of the MnGa magnetization was confirmed by Hall measurement with a small DC current.

There is a third term, the topological Hall effect, in the case of skyrmions. The Hall resistivity therefore, can be rewritten as

$$\rho_H = \rho_{\mathrm{O}} + \rho_{\mathrm{AHE}} + \rho_{\mathrm{THE}} \tag{3.3}$$

where ρ_{THE} is the topological Hall resistivity.

(2) UMR measurement

This measurement was used to evaluate the UMR ratio. The DC current was applied in the longitudinal direction, while MR was measured by the longitudinal V_{xx} voltage. UMR was defined as the difference of MR between positive and negative current.

(3) Differential planar Hall effect measurement

This measurement was used in order to separate SOT and thermal effect's contribution. The external magnetic field H_{ext} was rotated when a DC current was applied, and the differential planar Hall effect was measured as the difference of planar Hall resistivity between the positive and negative current.

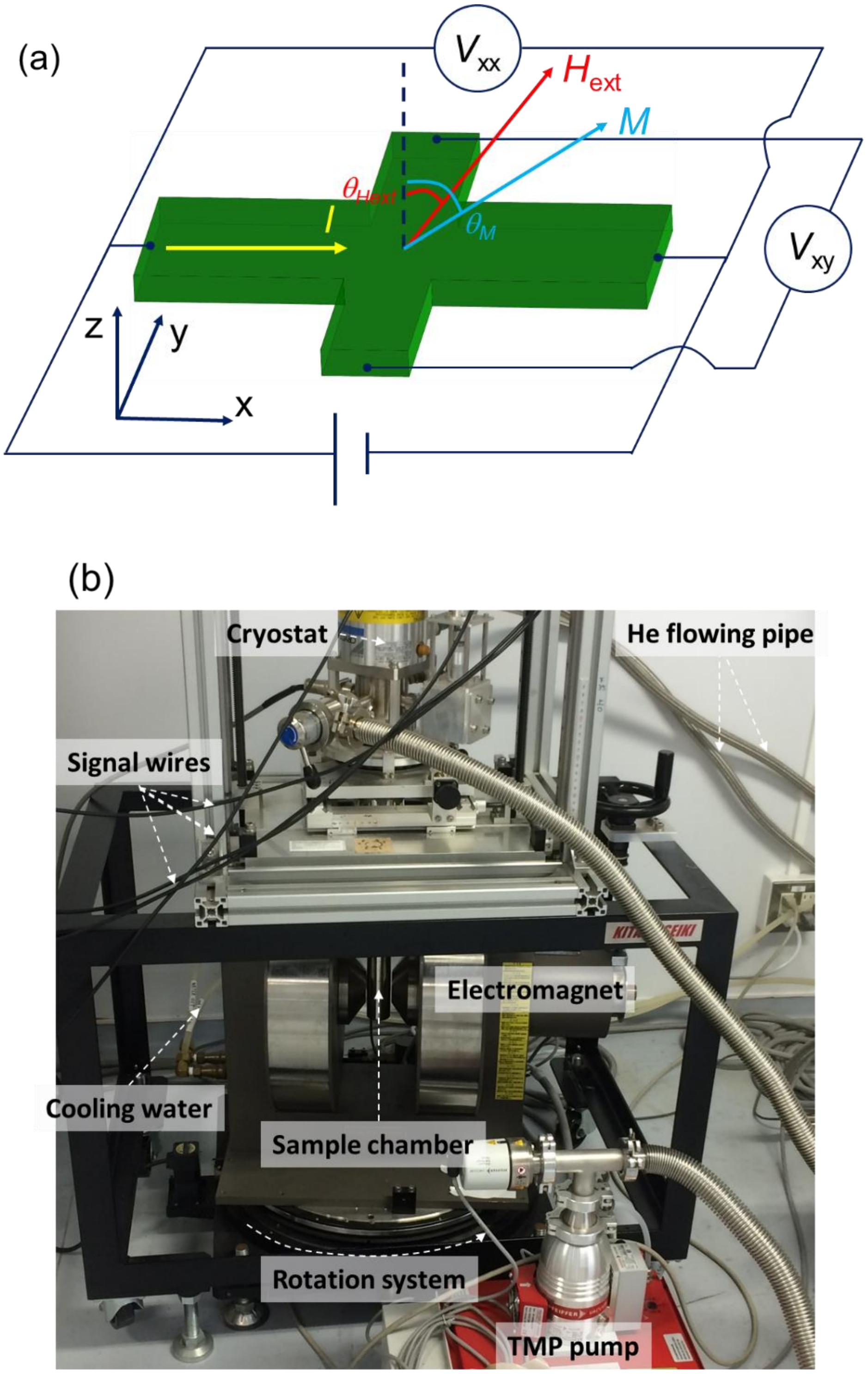

Figure 3.6: (a) Schematic illustration of the Hall effect measurement. (b) Photograph of the Hall effect measurement system.

3.2.3. Magneto-optical measurement

(1) Magnetic circular dichroism (MCD)

Figure 3.7 shows the schematic setup of the MCD measurement. The light generated from a Xenon lamp is passed through a monochromator toward the surface of sample. The light is modulated by a photoelastic modulator (PEM). The detector collects the intensity of reflected light, and measures the difference in optical reflectivity between right and left circular polarization. This measurement gives information of spin splitting of the band structure under an external magnetic field applied perpendicular to the film plane, and its intensity is written as

$$\mathrm{MCD} \approx \frac{90}{\pi}\frac{dR}{dE}\Delta E \tag{3.4}$$

where R is the optical reflectivity, E is the photon energy and ΔE is the spin-splitting energy by the Zeeman effect [5]. Because the MCD intensity is proportional to sample's perpendicular magnetization ($\Delta E \propto M$), MCD measurement is used to evaluate the magnetization of samples.

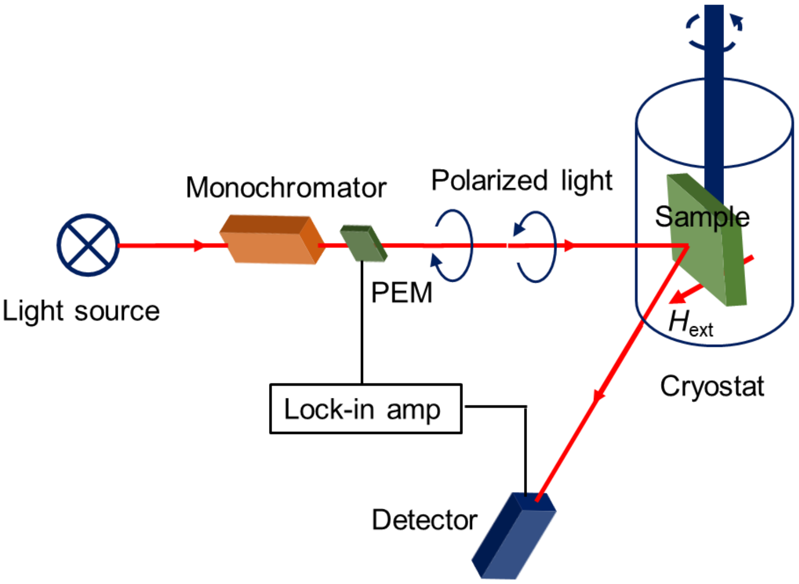

Figure 3.7: Schematic illustration of MCD measurement

(3) Longitudinal magneto-optic Kerr effect (in-plane MOKE)

To confirm the titling magnetization of $Mn_{0.45}Ga_{0.55}$ thin film in chapter 5, in-plane MOKE, a unique tool for the determination of the in-plane magnetization is employed [6]. A linearly polarized light is focused on the sample's magnetic domains by an objective lens. This light is reflected off the sample surface, and its polarization direction is rotated by the interaction with the sample's magnetic domains. The detector will collect the reflected light, and analyses the local magnetization by the magnitude of the polarized light's rotation.

3.2.4. Magnetization measurement

In order to evaluate the magnetization of samples, superconducting quantum interface device (SQUID), a very sensitive device based on the Josephson effect was used in my measurement. Figure 3.8 shows the schematic diagram of magnetic property measurement system (MPMS-5S Quantum Design). The SQUID is located in the bottom position of the MPMS system and detects the sample's magnetization through superconducting detection coils, which are connected to the SQUID. The current generated by the magnetization of the sample flows in this detection coil, and as consequence, an output voltage proportional to the detection coil's current is evaluated by SQUID [7].

3.2.5. Atomic force microscopy (AFM) measurement

AFM was employed in my measurement to observe the surface morphology of MnGa thin films. Figure 3.9 illustrates its operation mechanism. An oscillating cantilever with a sharp tip in nanometer, is brought near the sample surface. According to Hooke's law, the cantilever is deflected due to the atomic force between the tip and sample. The deflection of the cantilever is measured by a laser beam system. AFM can map the surface sample without using a conductive surface as in scanning tunneling microscope (STM). AFM therefore, can image almost any type of surface and has been widely used.

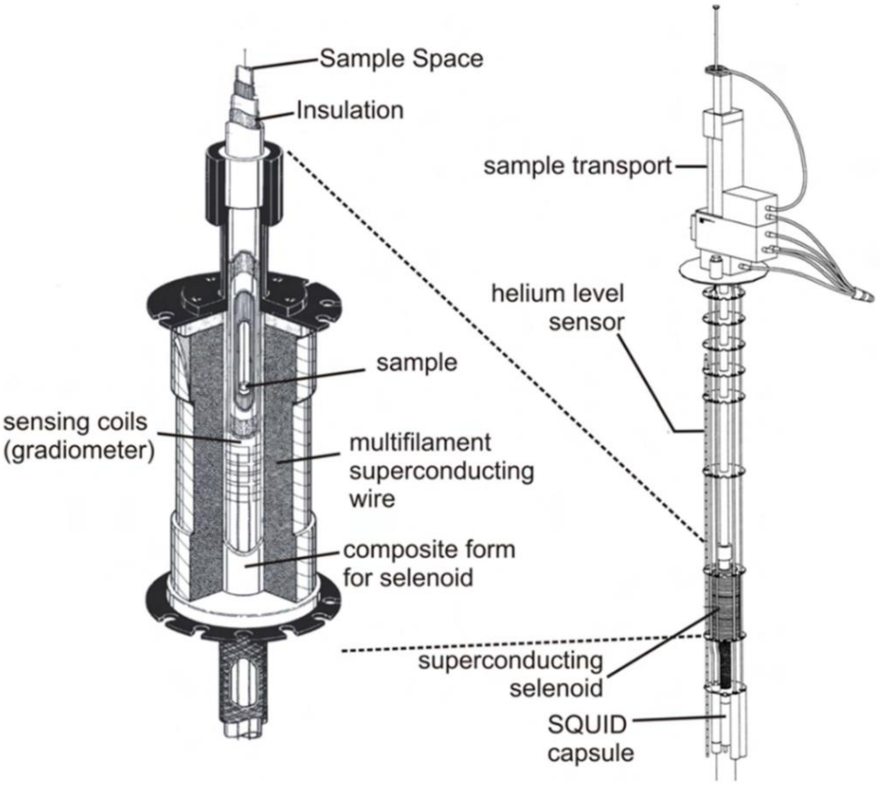

Figure 3.8: The schematic diagram of SQUID magnetometer MPMS XL-5S. Reproduced with permission [8].

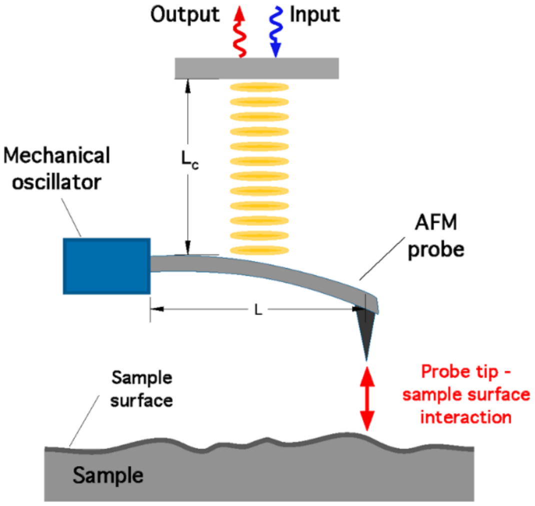

Figure 3.9: The schematic illustration of AFM measurement. Reproduced with permission [9].

3.3. Summary

In this chapter, the fabrication process of BiSb/FM bilayers and characterization techniques were presented. Fabrication based on MBE and real-time RHEED observation help us ensure the best crystal growth condition. Hall bar devices were fabricated for magnetotransport measurement. To fully understand the characteristics of samples, various kinds of measurements were used.

References

1. K. Alavi, Ency. Mater. Sci. Tech., 5765 (2001).

2. F. Tang, T. Parker, G. C. Wang, and T. M. Lu, J. Phys. D: Appl. Phys. **40**, R427 (2007).

3. M. D. Szata, Mater. Chem. Phys. **81**, 257 (2003).

4. D. A. Allwooda, R. T. Carlineb, N. J. Masona, C. Pickering, B. K. Tannerc, P. J. Walker, Th. Sol. Fil. **364**, 33 (2000).

5. P. N. Hai, L. D. Anh, S. Mohan. T. Tamegai, M. Kodzuka, T. Ohkubo, K. Hono, and M. Tanaka, Appl. Phys. Lett. **101**, 182403 (2012).

6. T. Haider, Inter. J. Elec. Appl. **7**, 17 (2017).

7. R. L. Fagaly, Rev. Sci. Instrum. **77**, 101101 (2006).

8. A. Barth, "Magnetic and structural properties of the Gd/Ni-bilayer-system", PhD thesis, 32 (2007).

9. A. Passian, and G. Siopsis, Phys. Rev. A **95**, 043812 (2017).

Chapter 4

MnGa Thin Films with Perpendicular Magnetic Anisotropy Grown on BiSb Topological Insulator

In order to study spin-related phenomena in BiSb/FM bilayers, the first step in my Ph.D. thesis is to grow a FM layer on BiSb. Here, MnGa was chosen as a candidate for the FM layer, because of its unique characteristics. MnGa shows small magnetization (M_s < 400 emu/cm^3) [1-12] and small damping factor ($\alpha < 0.008$) [13], which are promising for low-power magnetization switching. Furthermore, Mn_xGa_{1-x} thin films also show large PMA (K_u > 10 Merg/cm^3) and high T_C [1], which are essential for long time thermal stability. Recent studies have shown that Mn_xGa_{1-x} is a potential candidate not only for conventional STT-MRAM [14] but also for SOT-MRAM with heavy metal (Pt or Ta) / MnGa bilayers [15,16].

In this chapter, the crystal growth, structural and magnetic properties of $Bi_{0.8}Sb_{0.2}$ topological insulator (TI) / Mn_xGa_{1-x} bilayers grown on GaAs(111)A substrates by molecular beam epitaxy (MBE) will be reported. By optimizing the growth condition and Mn composition, I show that Mn_xGa_{1-x} thin films can be grown on $Bi_{0.8}Sb_{0.2}$ with crystallographic orientation of $Bi_{0.8}Sb_{0.2}(001)[1\bar{1}0]$ // MnGa (001)[100]. Using MCD spectroscopy, both L1$_0$ phase ($x < 0.6$) and D0$_{22}$ phase ($x > 0.6$) of Mn_xGa_{1-x} was detected. For $0.50 \le x \le 0.55$, ferromagnetic L1$_0$-MnGa thin films with clear perpendicular magnetic anisotropy (PMA) were confirmed by MCD hysteresis, anomalous Hall effect (AHE) as well as SQUID measurement.

4.1. Growth of BiSb - Mn_xGa_{1-x} bilayers by MBE

There are two main concerns about the growth of BiSb/Mn_xGa_{1-x} bilayers by MBE. First, the crystal structure of BiSb and Mn_xGa_{1-x} is completely different from each other. BiSb has a three-fold symmetric crystal structure as shown in Figure 4.1(a) [17]. In contrast, Mn_xGa_{1-x} has two phases: the $L1_0$ ferromagnetic phase for $0.43 \le x < 0.66$ ($Mn_{2-\sigma}Ga$) and the $D0_{22}$ ferrimagnetic phase for $0.66 \le x < 0.75$ (Mn_2Ga, Mn_3Ga), but both of them have four-fold symmetric tetragonal crystal structure [1], as shown in Figure 4.1(b). While there are several attempts for growth of MnGa thin films on various substrates, such as GaAs(001) [2], GaN(0001) [18, 19], GaSb(111) or Al_2O_3(0001) [20], MgO [1, 6], and ScN [21], only a few of those thin films grown on four-fold symmetric GaAs(001) and MgO(001) substrates show clear PMA. In addition to difference in crystal symmetry, the lattice mismatch between Mn_xGa_{1-x} (a_{MnGa} ~ 0.39 nm) [22, 23] and BiSb (a_{BiSb} ~ 0.46 - 0.43 nm) [24] is larger than 10%. These pose a big challenge for growing Mn_xGa_{1-x} thin film with high PMA on BiSb.

To overcome these problems, I employed a growth technique of the BiSb/MnGa bilayers on GaAs(111)A substrates by the MBE method as shown in Fig. 4.2(a). After removing the surface oxide layer of GaAs(111)A substrate at 570°C, a 40 nm-thick GaAs buffer layer was grown to obtain an atomically smooth surface. Then, the substrate was cooled to 150°C for growing a 20 nm-thick $Bi_{0.8}Sb_{0.2}$ layer at a rate of 8 nm/min. For growing Mn_xGa_{1-x} thin films on top of the $Bi_{0.8}Sb_{0.2}$ layer, the template method, originally developed by M. Tanaka *et. al* [25] for growth of MnGa thin films on GaAs(001) substrates, was employed. First, the substrate temperature T_{sub} was reduced to 40°C, and 4 monolayers (MLs) of Mn-Ga-Mn-Ga were deposited on top of $Bi_{0.8}Sb_{0.2}$. Then, the 4 MLs were heated up to 230°C for crystallization so as a thin $Mn_{0.5}Ga_{0.5}$ template was formed on the surface of $Bi_{0.8}Sb_{0.2}$. Finally, Mn_xGa_{1-x} thin films with the total thickness of 8 nm and the Mn composition between 0.45 and 0.74 were grown at a rate of 0.5 nm/min. The growth process was monitored *in situ* by RHEED. Figure 4.2(b) shows the RHEED patterns observed along the GaAs$[1\ \bar{1}\ 0]$ direction during the growth of BiSb/Mn_xGa_{1-x} bilayers on GaAs(111)A substrates for x = 0.74, 0.55 and 0.45. The $Bi_{0.8}Sb_{0.2}$ thin films show bright RHEED with Kikuchi lines, confirming that the $Bi_{0.8}Sb_{0.2}$ thin films were epitaxially grown on GaAs (111)A as reported in [26]. The RHEED patterns of 4 MLs of Mn-Ga-Mn-Ga deposited on top of $Bi_{0.8}Sb_{0.2}$ at 40°C were weak, but becomes bright with mixing streaky and dotty patterns after annealing at 230°C. This indicates that a crystallized template of $Mn_{0.5}Ga_{0.5}$ was formed. The Mn_xGa_{1-x} layers grown on this template remain crystalline, but their RHEED patterns become dim with increasing the Mn_xGa_{1-x} thickness. The RHEED pattern of the 8 nm-thick Mn_xGa_{1-x} can still be observed for x = 0.74 and 0.55, but disappears for x = 0.45.

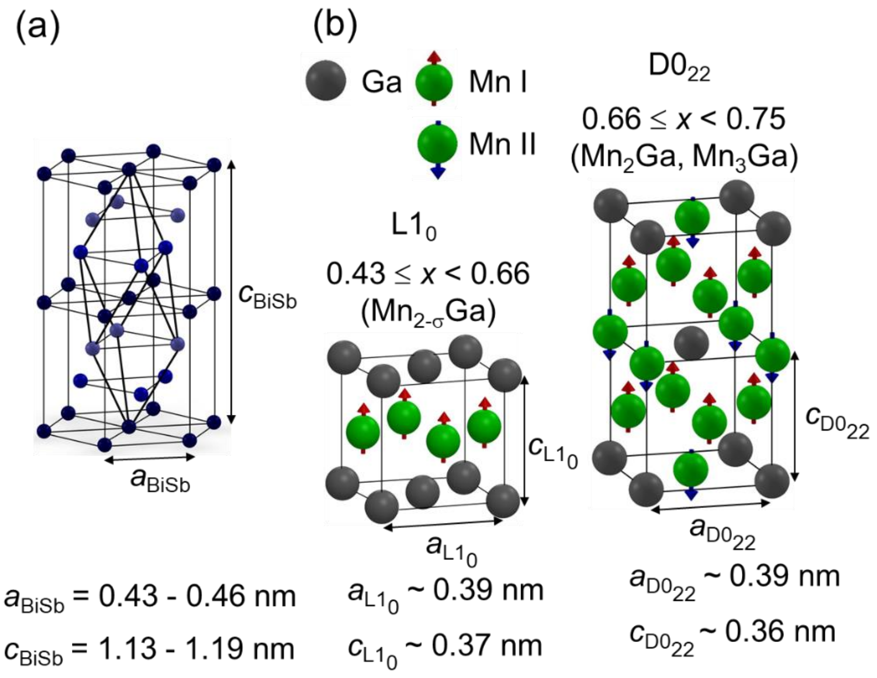

Figure 4.1: (a) Crystal structure of BiSb. (b) Crystal structures of $L1_0$ ferromagnetic phase (left) and $D0_{22}$ ferrimagnetic phase (right) of MnGa. The red and blue arrows represent the direction of Mn atoms' magnetic moments.

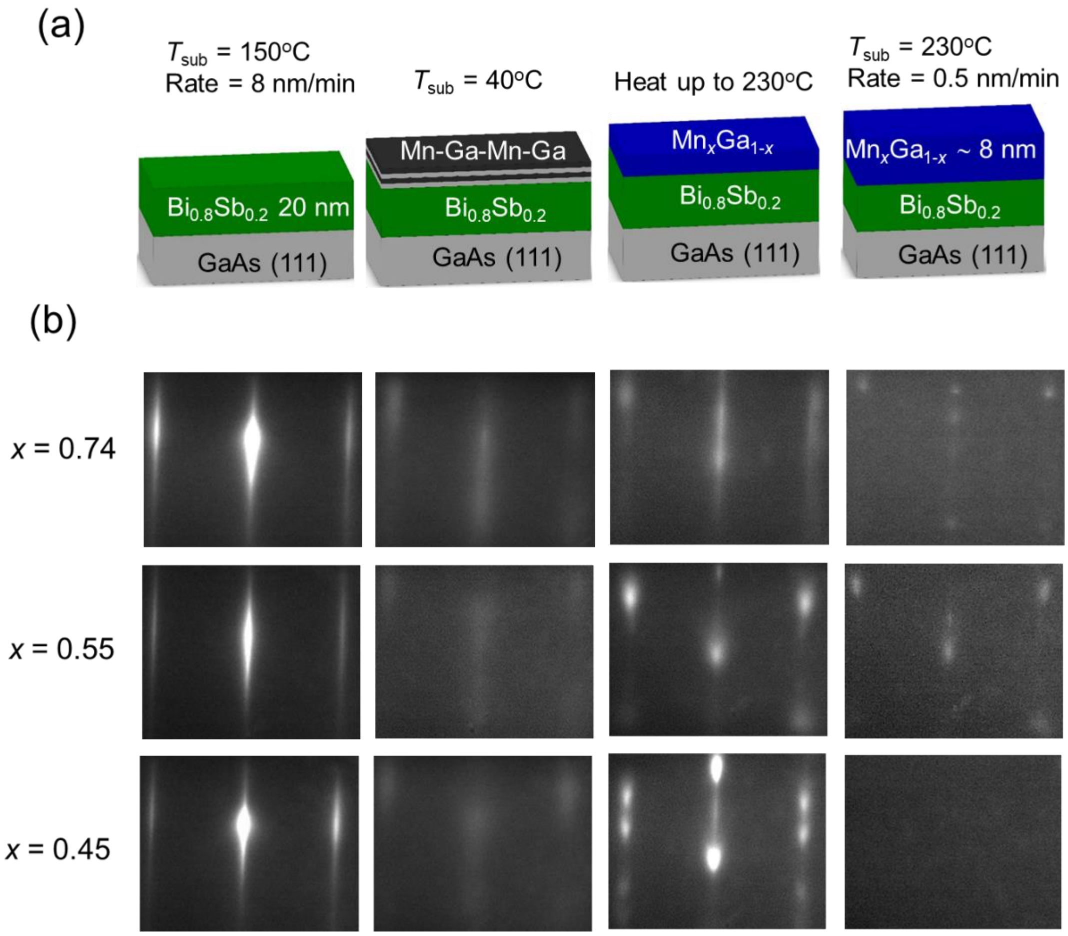

Figure 4.2: (a) Growth condition of $Bi_{0.8}Sb_{0.2}/Mn_xGa_{1-x}$ bilayers on GaAs(111)A substrates. (b) RHEED patterns observed along GaAs$[1\bar{1}0]$ direction during the growth of $Bi_{0.8}Sb_{0.2}/Mn_xGa_{1-x}$ bilayers.

4.2. Crystal structure analysis

4.2.1. Crystal orientation of Mn_xGa_{1-x} on BiSb thin films

After the growth, the crystal orientation of Mn_xGa_{1-x} thin films was evaluated by XRD measurements. Figure 4.3(a) shows the θ-2θ XRD spectra of $Bi_{0.8}Sb_{0.2}/Mn_xGa_{1-x}$ bilayers with different Mn composition x ranging from 0.45 to 0.74. Here, the hexagonal coordinate indexing was used for BiSb, and cubic coordinate indexing was used for GaAs and MnGa. Besides the $Bi_{0.8}Sb_{0.2}$(003), $Bi_{0.8}Sb_{0.2}$ (006), and (009) peaks, clear Mn_xGa_{1-x}(001) and Mn_xGa_{1-x}(002) peaks for all x was observed. A Mn_xGa_{1-x}(200) peak was also observed for high Mn composition ($x > 0.6$), but gradually decreases to the noise level for low Mn composition ($x < 0.6$). This indicates that it is possible to grow MnGa(001) on top of $Bi_{0.8}Sb_{0.2}$(001) despite their differences in crystal symmetry and lattice constant.

4.2.2. In-plane crystallographic relationships

In order to investigate the in-plane crystallographic relationship between MnGa(001) and BiSb(001), I measured the ϕ–scan XRD pattern of the $Mn_{0.5}Ga_{0.5}$ thin film at $\psi = 43.7^{\circ}$ and $2\theta = 36.6^{\circ}$ (Fig. 4.3(b)), and compare it to that of GaAs(111) at $\psi = 70.3^{\circ}$ and $2\theta = 27.3^{\circ}$ (Fig. 4.3(c)). As shown in Fig. 4.3(b), three equivalent sets of four-fold symmetric $Mn_{0.5}Ga_{0.5}$(011), (101), $(0\bar{1}1)$ and $(\bar{1}01)$ peaks were observed with each set shifted by 60° from each other. Comparing these peaks with those of GaAs$(1\bar{1}1)$, GaAs$(11\bar{1})$, and GaAs$(\bar{1}11)$, and taking into account the fact that BiSb$[1\bar{1}0]$(001)//GaAs$[1\bar{1}0]$(111) [26], the in-plane crystallographic relationships between MnGa and BiSb as MnGa[100]//BiSb $[1\bar{1}0]$ can be identified.

This relationships is reasonable because the lattice constant of BiSb along the BiSb$[1\bar{1}0]$ direction ($d \sim 7.8$Å) is exactly twice of $a_{\mathrm{MnGa}} \sim 3.9$Å, as shown in Fig. 4.3(d). Note that there are also two other equivalent MnGa in-plane crystallographic orientation, shifted by ±60° from that illustrated in Fig. 4.3(d), reflecting the three-fold symmetry of the hexagonal BiSb(001) surface. Figure 4.3(e) shows the measured lattice constant c of Mn_xGa_{1-x} grown on $Bi_{0.8}Sb_{0.2}$ as a function of x, compared with those of bulk [27, 28] and Mn_xGa_{1-x} thin films grown on MgO(001) [1] and GaAs(001) substrates [29]. At high x, c of Mn_xGa_{1-x} grown on $Bi_{0.8}Sb_{0.2}$ is close to those of bulk or thin films grown on MgO and GaAs. However, at low x, c of Mn_xGa_{1-x} grown on $Bi_{0.8}Sb_{0.2}$ is significantly smaller than the others. This suggests that Mn_xGa_{1-x} grown on $Bi_{0.8}Sb_{0.2}$ at low x may be under tensile-stress, i.e. the relationships $2a_{\mathrm{MnGa}} = d$ was kept even for low x.

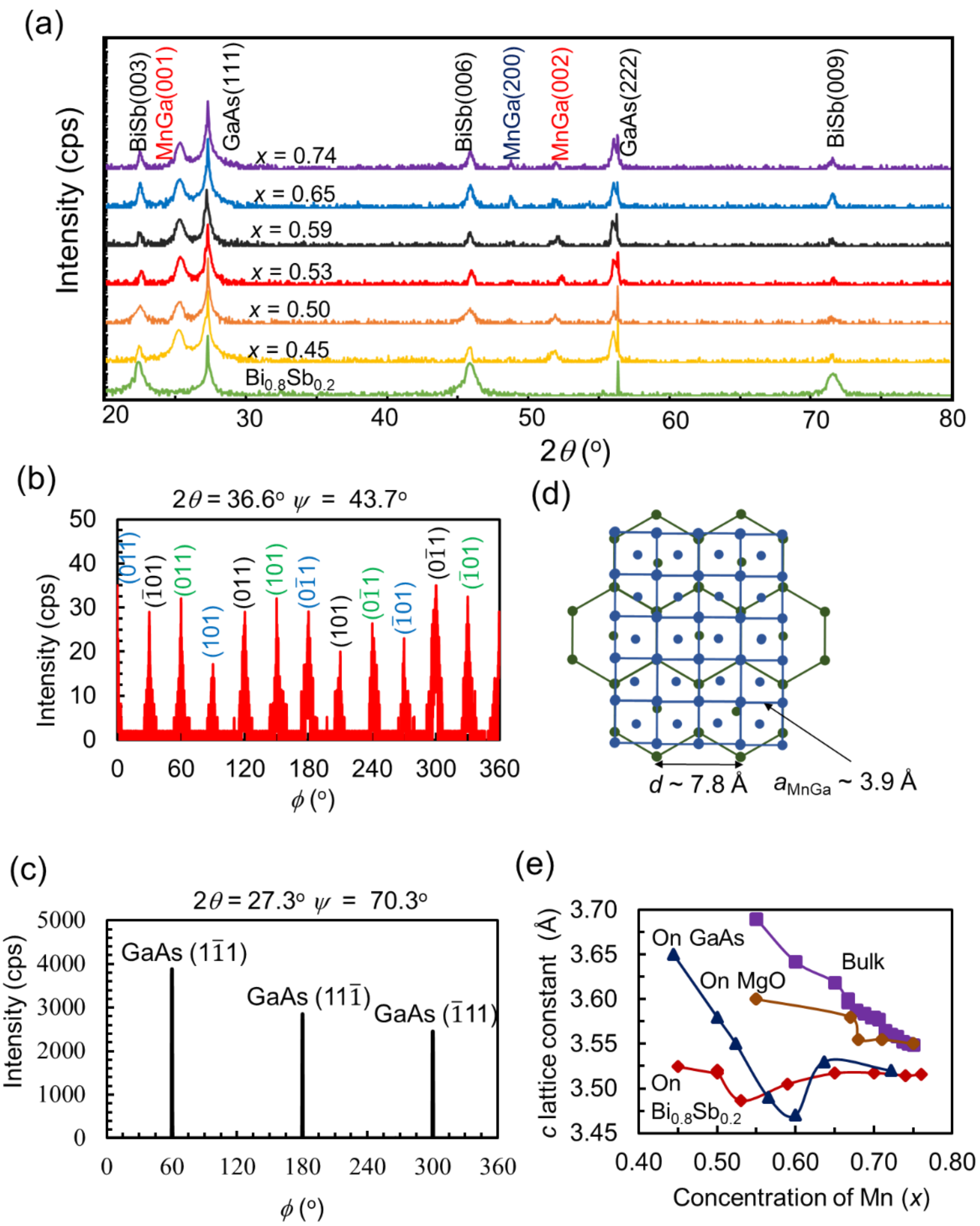

Figure 4.3: (a) θ - 2θ XRD spectra of $Bi_{0.8}Sb_{0.2}/Mn_xGa_{1-x}$ bilayers with Mn composition x ranging from 0.45 to 0.74. The XRD spectrum of a single $Bi_{0.8}Sb_{0.2}$ layer (bottom) is shown for reference. (b), (c) ϕ–scan XRD pattern of the $Mn_{0.5}Ga_{0.5}$ thin film and GaAs(111) substrate, respectively. (d) In-plane crystallographic orientation of MnGa (blue) on BiSb (green). (e) c lattice constant of Mn_xGa_{1-x} grown on $Bi_{0.8}Sb_{0.2}$ thin films as a function of x (this work), compared with those of bulk [22, 23], and Mn_xGa_{1-x} thin films grown on MgO(001) [11] and GaAs(001) substrate [29].

4.3. Magnetic properties

4.3.1. Magneto-optical properties

Next, the magnetic properties of Mn_xGa_{1-x} thin films grown on $Bi_{0.8}Sb_{0.2}$ were investigated. It is known that there is a magnetic phase transition from the DO_{22} ferrimagnetic phase ($x \geq 0.66$) to the $L1_0$ ferromagnetic phase ($x < 0.66$). In this study, the MCD spectroscopy technique was used to investigate such a magnetic phase transition. Here, MCD measures the difference between the reflectivity for right (R_{σ^+}) and left (R_{σ^-}) circular polarizations: $\mathrm{MCD}(E) = \frac{90}{\pi}\frac{\left(R_{\sigma^+}(E) - R_{\sigma^-}(E)\right)}{2R(E)}$, where R is the optical reflectivity, and E is the photon energy. Here, $R_{\sigma^+}(E)$ is determined by the optical transitions from the occupied spin-down band to the unoccupied spin-up band, while $R_{\sigma^-}(E)$ is determined by the optical transitions from the occupied spin-up band to the unoccupied spin-down band. That means the MCD spectrum reflects the spin-polarized band structure, and each specific magnetic material has its own MCD signature. Thus, it is possible to distinguish the DO_{22} ferrimagnetic phase ($x \geq 0.66$) and the $L1_0$ ferromagnetic phase ($x < 0.66$) of MnGa, even when their crystal structure and lattice constant are very similar. Furthermore, since the MCD intensity is proportional to z-direction magnetization M_z, it is also possible to measure the magnetization hysteresis by investigating the magnetic field dependence of the MCD intensity. Note that the MCD spectrum of the $D0_{22}$ and $L1_0$ phase of MnGa have never been reported so far.

Figures 4.4(a) and 4.4(b) show the normalized MCD spectra of various Mn_xGa_{1-x} thin films with $x = 0.74$ and 0.65, and $x = 0.59$, 0.55, 0.50, and 0.45, respectively. Here, the spectra were measured at 300 K with a magnetic field of 1 T applied perpendicular to the film plane. Two different spectral shapes were confirmed. The spectra of thin films with $x = 0.74$ and 0.65 show a broad plateaus at 3.5 ~ 5 eV, while those with $x = 0.59$, 0.55, 0.50, and 0.45 show a peak around 3.2-3.5 eV. The transition of the MCD spectral shape at about $x \sim 0.6$ agrees well with that of magnetic phase transition between the $D0_{22}$ and $L1_0$ phase of MnGa. These indicate that the spectral shape of thin films with $x = 0.65$, 0.74 reflects the $D0_{22}$ phase, while that of thin films with $x = 0.59$, 0.55, 0.50, and 0.45 reflects the $L1_0$ phase. Here, once can see that the spectral shapes in Figs. 4.4(a) and 4.4(b) are consistent with the band structures of $D0_{22}$ and $L1_0$-MnGa. Figures 4.4(c) and 4.4(d) show the spin-resolved density of states (DOS) of $D0_{22}$ and $L1_0$-MnGa, respectively, calculated by first principles [6]. The arrows in those figures indicate the optical transitions from the occupied spin-down band to the unoccupied spin-up band under irradiation of right circular polarized photons (σ^+). (For clarity, the optical transitions from the occupied spin-up band to the unoccupied spin-down band under irradiation of left circular polarized photons (σ^-) are omitted). For the $D0_{22}$-MnGa phase, the spin-down DOS under the Fermi energy spread over a broad band from -1 eV to -4 eV, while the spin-up DOS above the Fermi energy spread over a small band centering at about 1.5 eV. Therefore, the corresponding spectra of the optical transitions between them are broad, which explains the observed broad plateaus at 3.5 ~ 5 eV in Fig. 4.4(a). In contrast, the spin-down DOS of the $L1_0$-MnGa phase is localized around -1.3 eV, which explains the observed peaks around 3.2-3.5 eV in Fig. 4.4(b). These results show that MCD is a powerful tool to distinguish the $L1_0$ and the $D0_{22}$ phase of MnGa.

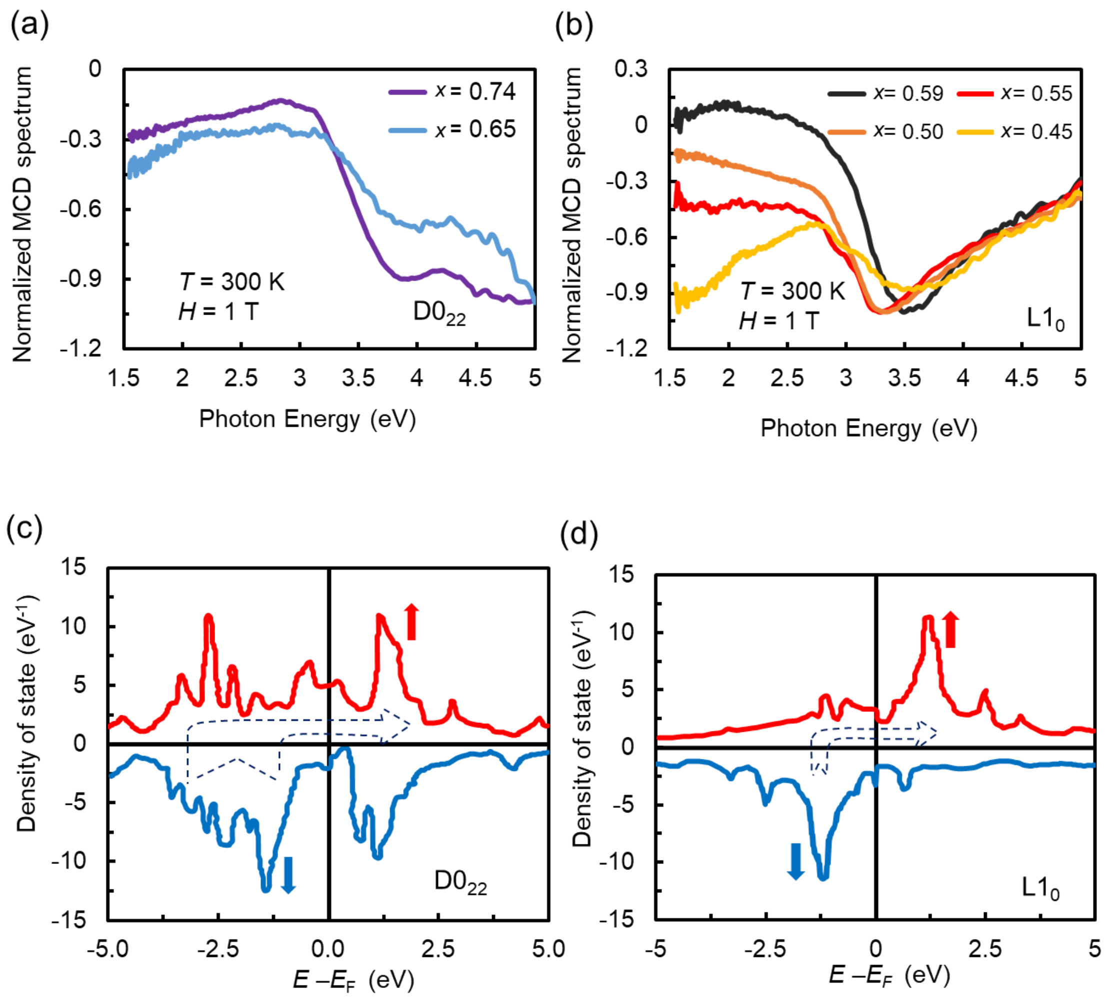

Figure 4.4: Normalized MCD spectra of BiSb/Mn_xGa_{1-x} bilayers for (a) $x = 0.74$ and 0.65, and (b) x = 0.59, 0.55, 0.50, and 0.45. Spin-resolved density of states (DOS) of (c) $D0_{22}$ and (d) $L1_0$-MnGa, calculated by first principles.

4.3.2. Magnetization properties

Next, the MCD intensity-magnetic field (MCD-H) characteristics were investigated, which reflects the hysteresis of perpendicular magnetizations M_z. Figure 4.5(a) shows the normalized MCD-H hysteresis for various Mn_xGa_{1-x} thin films. Poor squareness of the hysteresis of DO_{22}-Mn_xGa_{1-x} thin films ($x = 0.65, 0.74$) was observed. In contrast, good squareness of the hysteresis of $L1_0$-Mn_xGa_{1-x} thin films was obtained. In particular, the Mn_xGa_{1-x} thin films with $x = 0.50$ and 0.55 exhibit good PMA characteristics with 100% of remanence factor. We also evaluated the hysteresis of these two samples by using SQUID and AHE measurements. Figures 4.5(b) and 4.5(c) compare the normalized hysteresis obtained by MCD, SQUID, and AHE measurements for sample with $x = 0.50$ and 0.55, respectively. The hysteresis curves obtained by different methods agree well with each other. The coercive force is about 0.6 T for $x = 0.50$, and 0.5 T for $x = 0.55$, which are close to those reported for Pt/MnGa or Ta/MnGa bilayers [30, 16].

Figure 4.6(a) and 4.6(b) show the out-of-plane and in-plane M-H curves up to 70 kOe of two BiSb/Mn_xGa_{1-x} bilayers with $x = 0.50$ and 0.55. From these data, the uniaxial magnetic anisotropy constant (K_u) of the Mn_xGa_{1-x} layers was calculated to be around 2.2 Merg/cc and 2.3 Merg/cc for $x = 0.50$ and 0.55, respectively. Those values of K_u are small compared with those of stand-alone MnGa layers grown on MgO(001). Note that reduction of K_u is due to the small saturation magnetization M_S of the MnGa layers (87 emu/cc and 78 emu/cc for $x = 0.50$ and 0.55, respectively), rather than by reduction of the uniaxial anisotropy magnetic field. Indeed, the in-plane saturation magnetic field is as high as 55 ~ 60 kOe, which is similar to those of high-quality stand-alone MnGa thin films grown on MgO(001).

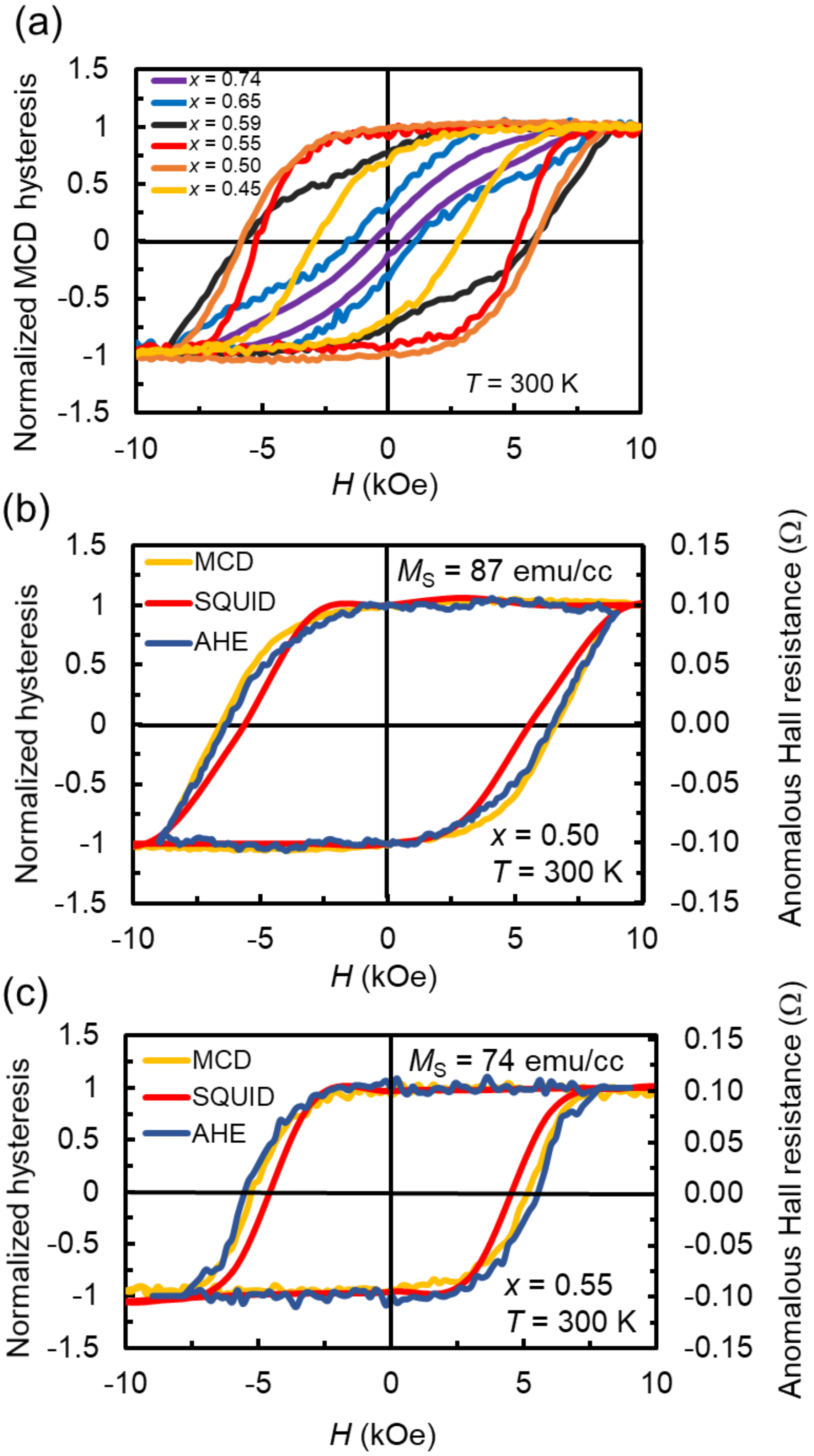

Figure 4.5: (a) Normalized MCD hysteresis of BiSb/Mn_xGa_{1-x} bilayers. (b) and (c) Normalized hysteresis obtained by MCD, SQUID, and AHE measurements for BiSb/Mn_xGa_{1-x} bilayer with $x = 0.50$ and 0.55, respectively.

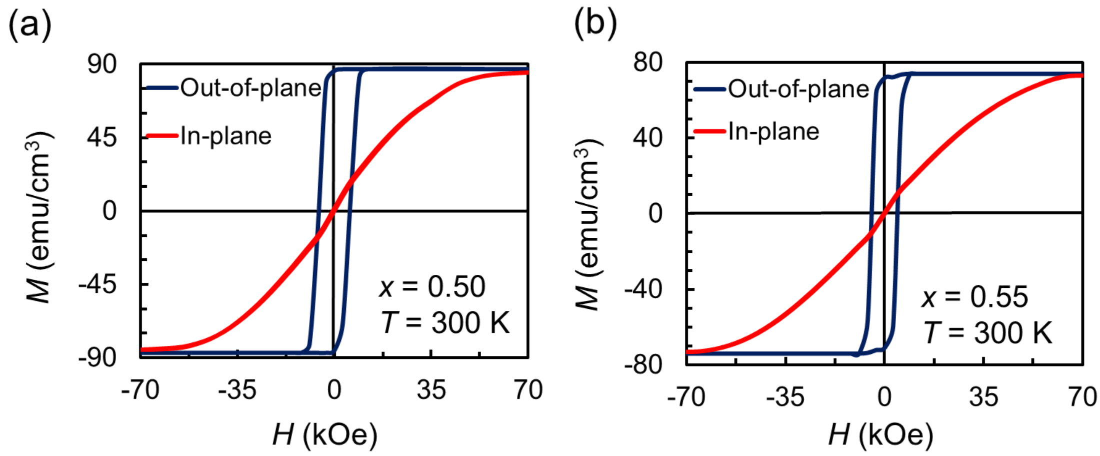

Figure 4.6: Out-of-plane (blue) and in-plane (red) *M*-*H* curves of BiSb/Mn_xGa_{1-x} bilayers with (a) x= 0.50 and (b) x = 0.55 at room temperature.

4.3.3. Discussion

There are two reasons for the small M_S observed in BiSb/Mn_xGa_{1-x} bilayer system. First, it is known that high substrate temperature of 450–500°C is needed for obtaining high-quality MnGa thin films with high M_S [13]. However, the melting temperature of BiSb is low (280°C for $Bi_{0.9}Sb_{0.1}$), thus low substrate temperature of 230°C had to be used to grow MnGa layers on top of BiSb, resulting in low chemical ordering of MnGa as indicated by the dim RHEED patterns in Fig. 4.2(b). One solution of this problem is to grow a high-quality MnGa layer first on suitable substrates, such as GaAs(001) or MgO(001), and then grow the BiSb layer on top of the high-quality MnGa layer. Another problem is the existence of the three equivalent in-plane crystallographic domains of MnGa on BiSb, each shifted by 60° from each other, as indicated by the ϕ–scan XRD pattern in Fig. 4.3(b). Because MnGa has a tetragonal crystal structure, a large amount of crystal defects would exist at the interfaces between neighboring MnGa domains to absorb this 60° shift. Such crystal defects at various MnGa domain boundaries would significantly reduce the crystal quality and the M_S of the overall MnGa layer. To solve this problem, it is necessary to break the in-plane three-fold symmetry of the BiSb(001) surface. This may be done by applying an in-plane uniaxial stress to the substrates, or using substrates with lower crystal symmetry, such as those with orthorhombic crystal structures.

4.4. Summary

In conclusion, crystalline Mn_xGa_{1-x} thin films was grown on $Bi_{0.8}Sb_{0.2}$ layer despite their differences in crystal symmetry and lattice constant. XRD analysis indicates that Mn_xGa_{1-x} grows on $Bi_{0.8}Sb_{0.2}$ with the crystallographic orientation of $Bi_{0.8}Sb_{0.2}(001)[1\bar{1}0]$//MnGa(001)[100]. In addition, $L1_0$ ($x < 0.6$) and $D0_{22}$ phase ($x > 0.6$) of Mn_xGa_{1-x} were distinguished by using MCD spectroscopy. For $0.50 \le x \le 0.55$, MnGa thin films showed large PMA characteristics confirmed by MCD, AHE, and SQUID measurements. These results show that BiSb/Mn_xGa_{1-x} bilayer system is promising for perpendicular magnetization switching using giant spin Hall effect in TIs. This technique can possibly be applied to growth of other ferromagnetic materials with a similar crystal structure and high PMA, such as FePt, FePd, MnGe, and MnAl, on other TIs, such as Bi_2Se_3 and Bi_2Te_3.

References

1. L. J. Zhu, S. H. Nie, and J. H. Zhao, Chin. Phys. B **22**, 118505 (2013).

2. M. Tanaka, J. P. Harbison, J. DeBoeck, T. Sands, B. Philips, T. L. Cheeks, and V. G. Keramidas, App. Phys. Lett. **62**, 1565 (1993),

3. S. Zhao, and T. Suzuki, AIP Adv. **6**, 056025 (2016).

4. W. Y. Zhang, P. Kharel, S. Valloppilly, R. Skomski, and D. J. Sellmyer, J. Appl. Phys. **117**, 17E306 (2015).

5. K. Wang, E. Lu, J. W. Knepper, F. Yang, and A. R. Smith, Appl. Phys. Lett. **98**, 162507 (2011).

6. S. Mizukami, T. Kubota, F. Wu, X. Zhang, T. Miyazaki, H. Naganuma, M. Oogane, A. Sakuma, and Y. Ando, Phys. Rev. B 85, 014416 (2012).

7. F. Wu, E. P. Sajitha, S. Mizukami, D. Watanabe, T. Miyazaki, H. Naganuma, M. Oogane, and Y. Ando, Appl. Phys. Lett. **96**, 042505 (2010).

8. M. Tanaka, Mater. Sci. Eng. B **31**, 117 (1995).

9. A. Köhler, I. Knez, D. Ebke, C. Felser, and S. S. P. Parkin, Appl. Phys. Lett. **103**, 162406 (2013).

10. J.N. Feng, W. Liu, W.J. Gong, X.G. Zhao, D. Kim, C.J. Choi and Z.D. Zhang, J. Mater. Sci. Tech. **33**, 291 (2017).

11. L. J. Zhu, S. Nie, K. Meng, D. Pan, J. Zhao, and H. Zheng, Adv. Mater. **24**, 4547 (2012).

12. W. Feng, D. V. Thiet, D. D. Dung, Y. Shin, and S. Cho, J. Appl. Phys 108, 113903 (2010).

13. S. Mizukami, F. Wu, A. Sakuma, J. Walowski, D. Watanabe, T. Kubota, X. Zhang, H. Naganuma, M. Oogane, Y. Ando, and T. Miyazaki, Phys. Rev. Lett. **106**, 117201 (2011).

14. K. Z. Suzuki, R. Ranjbar, J. Okabayashi, Y. Miura, A. Sugihara, H. Tsuchiura, and S. Mizukami, Sci. Rep. **6**, 30249 (2016).

15. R. Ranjbar, K. Z. Suzuki, Y. Sasaki, L. Bainsla, and S. Mizukami, Jpn. J. Appl. Phys 55, 120302 (2016).

16. K. K. Meng, J. Miao, X. G. Xu, J. X. Xiao, J. H. Zhao, and Y. Jiang, Phys. Rev. B **94**, 214413 (2016).

17. B. Stegemann, C. Ritter, B. Kaiser, and K. Rademann, Phys. Rev. B **69**, 155432 (2004).

18. E. Lu, D. C. Ingram, A. R. Smith, J. W. Knepper, and F. Y. Yang, Phys. Rev. Lett. **97**, 146101 (2006).

19. A. Bedoya-Pinto, C. Zube, J. Malindretos, A. Urban, and A. Rizzi, Phys. Rev. B **84**, 104424 (2011).

20. W. Fenga, D. V. Thiet, D. D. Dung, Y. Shin, and S. Chob, J. Appl. Phys. **108**, 113903 (2010).

21. K. Wang K, A. Chinchore A, W. Lin, D.C. Ingram, A. R. Smith, A. J. Hauser, and F. Yang, J. Cryst. Growth **311**, 2265 (2009).

22. T. A. Bither and W. H. Cloud, J. Appl. Phys. **36**, 1501 (1965).

23. J. Winterlik, B. Balke, G. H. Fecher, C. Felser, M. C. M. Alves, F. Bernardi, and J. Morais, Phys. Rev. B **77**, 054406 (2008).

24. H. Berger, B. Christ, and J. Troschke, Crys. Res. Tech. **17**, 1233 (1982).

25. M. Tanaka, J. P. Harbison, J. DeBoeck, T. Sands, B. Philips, T. L. Cheeks, and V. G. Keramidas, Appl. Phys. Lett. **62**, 1565 (1993).

26. Y. Ueda, N. H. D. Khang, K. Yao, and P. N. Hai, Appl. Phys. Lett. **110**, 062401 (2017).

27. T. A. Bither and W. H. Cloud, J. Appl. Phys. **36**, 1501 (1965).

28. J. Winterlik, B. Balke, G. H. Fecher, C. Felser, M. C. M. Alves, F. Bernardi, and J. Morais, Phys. Rev. B **77**, 054406 (2008).

29. L. J. Zhu, D. Pan, S. H. Nie, J. Lu, and J. H. Zhao, Appl. Phys. Lett. **102**, 132403 (2013).

30. K. Meng, J. Miao, X. Xu, Y. Wu, J. Xiao, J. Zhao and Y. Jiang, Sci. Rep. **6**, 38375 (2016).

Chapter 5

Spin Hall Effect in BiSb Topological Insulator

SOT using the SHE in heavy metal and topological insulators has great potential for ultra-low power SOT-MRAM. To be competitive with conventional STT-MRAM, a pure spin current source with large spin Hall angle ($\theta_{SH} > 1$) and high electrical conductivity ($\sigma > 10^5\ \Omega^{-1}m^{-1}$) is required. However, this requirement cannot be satisfied in heavy metals (such as Pt, Ta, and W) with high σ but small θ_{SH} (~ 0.1) [1, 17, 23], and TIs with large θ_{SH} but low σ [2, 3]. There is no spin Hall material so far that can satisfy both conditions simultaneously.

This chapter will focus on evaluation of the SHE in the topological insulator $Bi_{1-x}Sb_x$ ($0.07 \leq x \leq 0.22$) with strong spin orbit coupling [4]. Thanks to its high carrier mobility (~10^4 cmV^{-1}s^{-1}), our previous work showed that the average conductivity of BiSb thin films is as large as $2.5\times10^5\ \Omega^{-1}m^{-1}$ [5], which is compatible to other metallic materials used in realistic MRAM. On the other hand, its non-trivial topologically protected surface states have been confirmed by the angle-resolved photoemission spectroscopy (ARPES) [6, 7, 8] and magneto-transport measurements [9, 10]. Thus, BiSb promises large SHE. In this work, the performance of thin BiSb films as a pure spin current source in various BiSb / MnGa bilayers will be investigated. The large spin Hall angle in BiSb will be evaluated and compared with other spin Hall materials. Finally, prospective applications of SOT-MRAM based on BiSb will be discussed.

5.1. Thin film growth and crystal structure characterizations

The BiSb / MnGa bilayer thin films were grown on semi-insulating GaAs(001) substrates by using ultrahigh vacuum MBE system. After removing the surface oxide layer of the GaAs substrate at 580^{o}C, a 100 nm-thick GaAs buffer layer was grown to obtain an atomically smooth surface. The substrate was cooled down to room temperature for deposition of a 4 monolayer Mn-Ga-Mn-Ga template. Then, the substrate was heated up to 250^{o}C for deposition of a MnGa thin film with the total thickness of 3 nm. A $Bi_{0.1}Sb_{0.9}$ layer was grown on top of the MnGa layer at 200^{o}C with the rate of 1 nm/min. Finally, the samples were cooled down again to room temperature for deposition of an As thin cap layer. The growth process was monitored *in situ* by reflection high energy electron diffraction.

By optimizing the growth condition, high quality BiSb / MnGa bi-layers with smooth interface can be obtained, despite the large lattice mismatch between MnGa(001) and BiSb(012). Figure 5.1 shows the RHEED patterns during growth of the BiSb / MnGa bi-layers. The RHEED patterns of both MnGa (3) and BiSb (10) are streaky (the numbers in parentheses present layer's thickness in nanometers), indicating good crystal quality. To check the crystallographic orientation of the BiSb / MnGa bilayers, a thick BiSb (20) / MnGa (10) bilayer was grown in the same condition and checked by X-ray diffraction measurements. Figure 5.2 shows the θ-2θ XRD spectrum of the BiSb (20) / MnGa (10) bi-layer. The XRD spectrum indicates that the crystallographic orientation is BiSb(012)//MnGa(001)//GaAs(001).

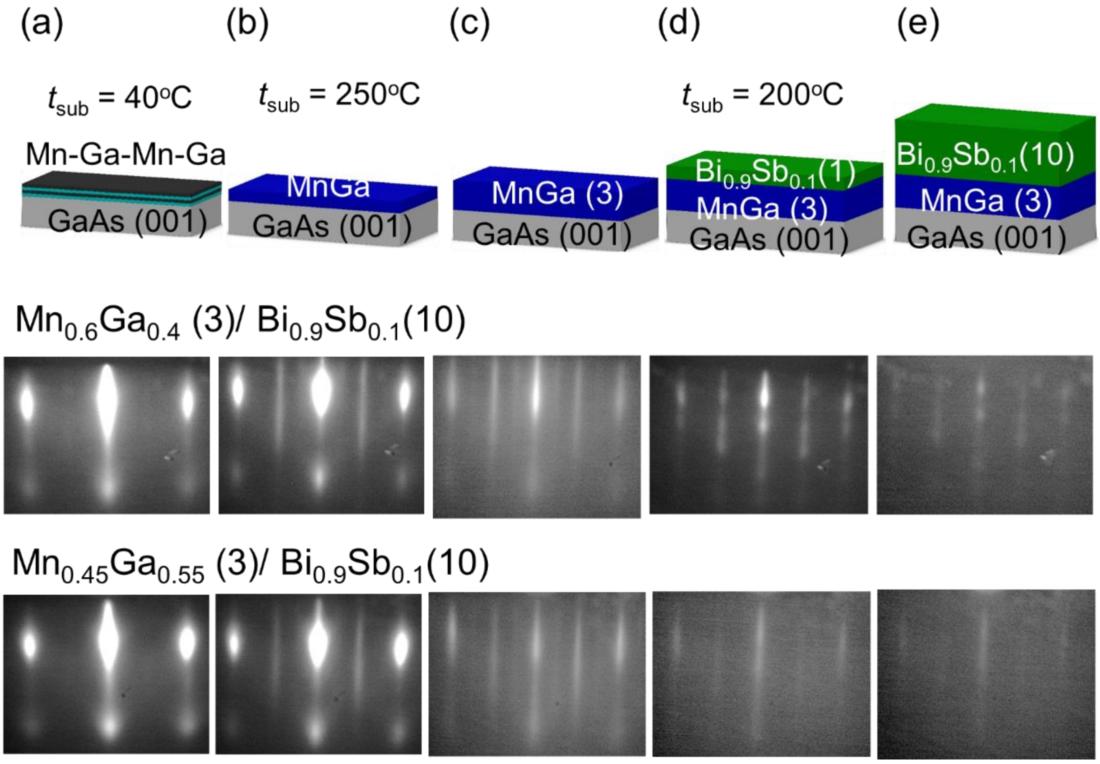

Figure 5.1: RHEED patterns during growth of the BiSb / MnGa bilayers (a) after deposition of the 4 monolayer Mn-Ga-Mn-Ga template, (b) after annealing the template at 250°C, (c) after growth of the 3 nm-thick MnGa layer, (d) after growth of a 1 nm-thick BiSb layer at 200°C, and (e) after growth of the 10 nm-thick BiSb layer.

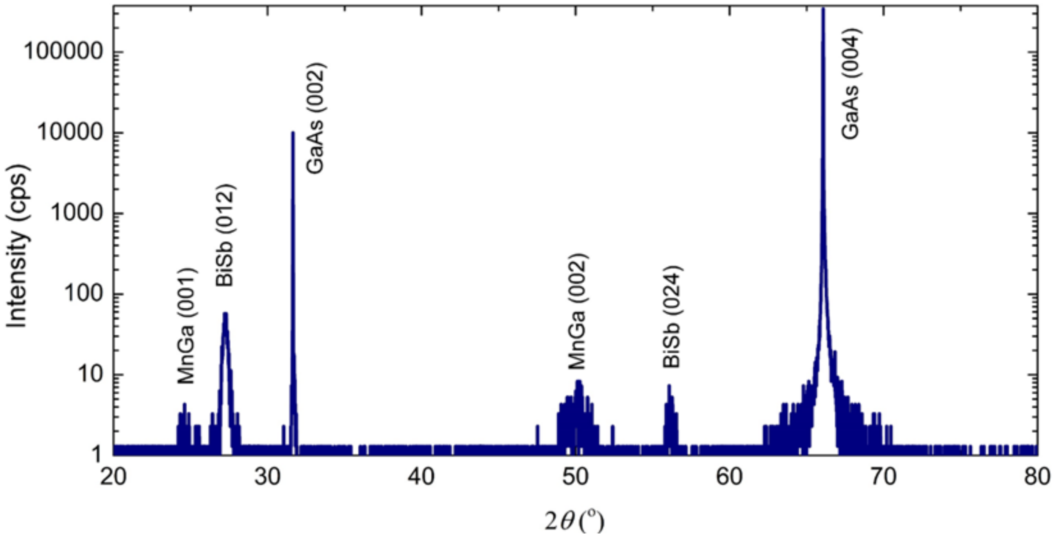

Figure 5.2: θ-2θ XRD spectrum of a BiSb (20) / MnGa (10) bilayer. The crystallographic orientation is BiSb(012)//MnGa(001)//GaAs(001).

5.2. Magnetic properties and SOT effect in $Bi_{0.9}Sb_{0.1}$-$Mn_{0.6}Ga_{0.4}$ bilayers

5.2.1. Magnetic properties

MnGa was employed as a model ferromagnet because its large perpendicular magnetic anisotropy (> 10 Merg/cc), large uniaxial anisotropy field (> 40 kOe), large coercive force (> 1.5 kOe), and high conductivity ($5\times10^5\ \Omega^{-1}m^{-1}$) represent well those would be used in futuristic ultra-high density SOT-MRAM [11]. Furthermore, by adjusting the Mn composition, I can grow $Mn_{0.6}Ga_{0.4}$ layers with perfect perpendicular magnetization and $Mn_{0.45}Ga_{0.55}$ layers with titling magnetization which are convenient for evaluation of the spin-orbit field generated by the BiSb layer.

Figure 5.3 (a) shows the schematic $Bi_{0.9}Sb_{0.1}$ (10) / $Mn_{0.6}Ga_{0.4}$ (3) (thickness in nm) bi-layer and the coordinate system used in this work. An electric current was applied along the x direction, while an external magnetic field H_{ext} was applied in the z-x plane at an angle θ with respect to the z axis. Figure 5.3 (c) shows the out-of-plane magnetization curve of the bilayer measured at various temperatures. The magnetization of the 3 nm-thick $Mn_{0.6}Ga_{0.4}$ layer in this bi-layer is the same as that of high quality stand-alone $Mn_{0.6}Ga_{0.4}$ thin films grown on GaAs(001), indicating that there is no interfacial magnetic dead layer.

5.2.2. SOT effect

The bi-layers are then patterned into 100 μm-long and 50 μm-wide Hall bars for transport measurements, as one shown in Fig. 5.3(b). The Hall bars are mounted inside a liquid nitrogen cryostat which acts as a heat sink to minimize the effect of Joule heating. Figure 5.3 (d) shows the Hall resistance R_H of a Hall bar under a perpendicular magnetic field ($\theta = 0$) at 150 K, measured with various current density $J = 0.2 – 15.4\times10^5$ A/cm^2. Here, J is the nominal current density of the Hall bar, defined as

$$J = I / [w(t_{\mathrm{BiSb}} + t_{\mathrm{MnGa}})] \qquad \textbf{(5.1)}$$

where I is the applied current (10 mA maximum), $w = 50$ μm is the width of the Hall bar, $t_{\mathrm{BiSb}} = 10$ nm and $t_{\mathrm{MnGa}} = 3$ nm are the thickness of the BiSb and MnGa layer, respectively.

The Hall resistance is dominated by the anomalous Hall effect which reveals the perpendicular magnetization component of the $Mn_{0.6}Ga_{0.4}$ layer. A systematic reduction of the coercive force H_c of the $Mn_{0.6}Ga_{0.4}$ layer was observed with increasing J. The reduction ΔH_c is as large as 2 kOe at a modest $J =15.4\times10^5$ A/cm^2. To make sure that this reduction of H_c is not the result of Joule heating of the $Mn_{0.6}Ga_{0.4}$ layer, a Hall bar from a stand-alone $Mn_{0.6}Ga_{0.4}$ (3) layer was prepared, and its Hall resistance was measured under various J. As seen in Fig. 5.3(e), no clear change of H_c up to $J = 46.7\times10^5$ A/cm^2 was confirmed, which is 3 time higher than the highest current density applied in Fig. 1(d). This indicates that the reduction of H_c shown in Fig. 5.3(d) is not the result of Joule heating. Indeed, for the Joule heating to be the origin of the large $\Delta H_c = 2$ kOe, the $Mn_{0.6}Ga_{0.4}$ layer temperature had to increase from 150 K to 250 K (see Fig. 5.3(c)), which is unlikely given the very small J used in our experiments, comparing with $J \sim 10^7$ - 10^8 A/cm^2 used in previous studies using heavy metals as the spin Hall layer. Furthermore, a significant reduction of the remanent R_H at $J =15.4\times10^5$ A/cm^2 was observed. This was not observed in the magnetization curve at 250 K. Therefore, the large reduction of H_c is the result of an in-plane spin-orbit field generated by spin current injection from the BiSb layer. Figure 5.3(f) shows ΔH_c as a function of the current density J_{BiSb} in the BiSb layer. Here, J_{BiSb} is calculated using $\sigma_{\mathrm{BiSb}} = 2.5\times10^5$ Ω^{-1}m^{-1}and $\sigma_{\mathrm{MnGa}} = 5\times10^5$ Ω^{-1}m^{-1}. The gradient $\Delta H_c/\Delta J_{\mathrm{BiSb}}$ is as large as 3700 Oe/(MA/cm^2) at high J_{BiSb} (dashed line in Fig. 5.3(f)).

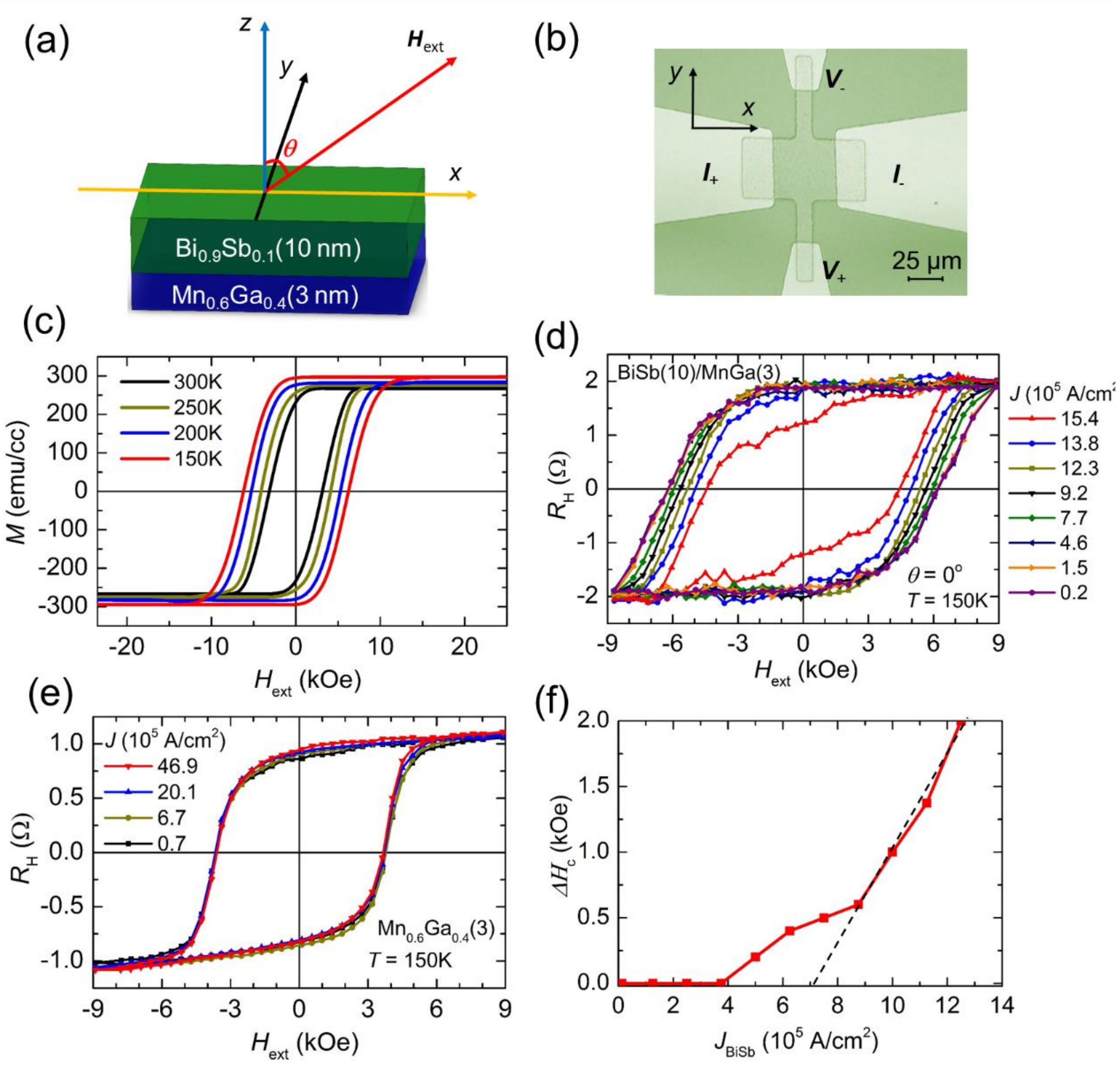

Figure 5.3: (a) Schematic structure of the $Bi_{0.9}Sb_{0.1}$ (10) / $Mn_{0.6}Ga_{0.4}$ (3) (thickness in nm) bi-layer and the coordinate system used in this work. (b) Micrograph of a 100 μm × 50 μm Hall bar device. (c) Out-of-plane magnetization curves of the bilayer at different temperatures. (d) Hall resistance R_H of a Hall bar under a perpendicular magnetic field H_{ext} ($\theta = 0$) at 150 K, measured with various current density $J = 0.2 – 15.4 \times 10^5$ A/cm^2. (e) R_H of a Hall bar of a stand-alone MnGa (3) layer. (f) Reduction of the coercive force ΔH_c of the bi-layer as a function of the current density J_{BiSb} in the BiSb layer.

5.3. Magnetic properties and SOT effect in $Bi_{0.9}Sb_{0.1}$-$Mn_{0.45}Ga_{0.55}$ bilayers

5.3.1. Magnetic properties

In order to quantitatively evaluate the spin Hall angle of BiSb, another bilayer $Bi_{0.9}Sb_{0.1}$ (10) / $Mn_{0.45}Ga_{0.55}$ (3) with tilting magnetization was prepared. The blue and the red curves in Fig. 5.4(a) show the in-plane and out-of-plane magnetization curve of $Bi_{0.9}Sb_{0.1}$ (10) / $Mn_{0.45}Ga_{0.55}$ (3) bilayers. Because of the tilting magnetization, the out-of-plain magnetization does not saturate until a perpendicular H_{ext} ~ 20 kOe is applied. The in-plane magnetization shows small remanence, but rapidly increases up to an in-plane H_{ext} ~ 4 kOe, then slowly increases and saturates at an in-plane H_{ext} ~ 50 kOe.

The magnetic domains of the $Mn_{0.45}Ga_{0.55}$ layer was investigated by an in-plane magneto-optical Kerr effect (MOKE) microscope. Unfortunately, the MOKE effect of MnGa is weaker than the resolution of the MOKE microscope, thus individual magnetic domains of the $Mn_{0.45}Ga_{0.55}$ layer could not be distinguished. Indeed, the magnetic circular dichroism (MCD) intensity (equivalent to MOKE ellipticity) of the $Mn_{0.45}Ga_{0.55}$ is only 20 mdeg, while the MOKE microscope requires at least 100 mdeg for working.

However, the horizontal component of the stray field from the $Mn_{0.45}Ga_{0.55}$ layer can be detected, indicating the existence of tilting domains. The experiment setup is as follows. First, a MOKE sensor with large MOKE effect was prepared, so that individual domains of the sensor are visible under our in-plane MOKE microscope. The in-plane magnetization of the sensor is known to saturate at about 400 Oe, and the sensor is used to visualize magnetic fields larger than 400 Oe. Then, the domains of the sensor was observed with and without contact with the $Mn_{0.45}Ga_{0.55}$ layer under in-plane magnetic fields. Figure 5.4(b) show the MOKE images of the sensor in contact with the $Mn_{0.45}Ga_{0.55}$ layer, while Figure 5.4(c) show those of the sensor without contact with the $Mn_{0.45}Ga_{0.55}$

layer. In Fig. 5.4(b), the sensor is saturated (i.e. all domains disappear and the MOKE image becomes dark) when an in-plane magnetic field of ±300 Oe is applied. In contrast, in Figs. 5.4(c), the sensor is saturated at ±400 Oe. This indicates that there is an in-plane component of the stray field from $Mn_{0.45}Ga_{0.55}$ when an external H_{ext} = 300 Oe is applied, which gives evidence that the tilting domains in the $Mn_{0.45}Ga_{0.55}$ layer rapidly reorientate toward the magnetic field direction.

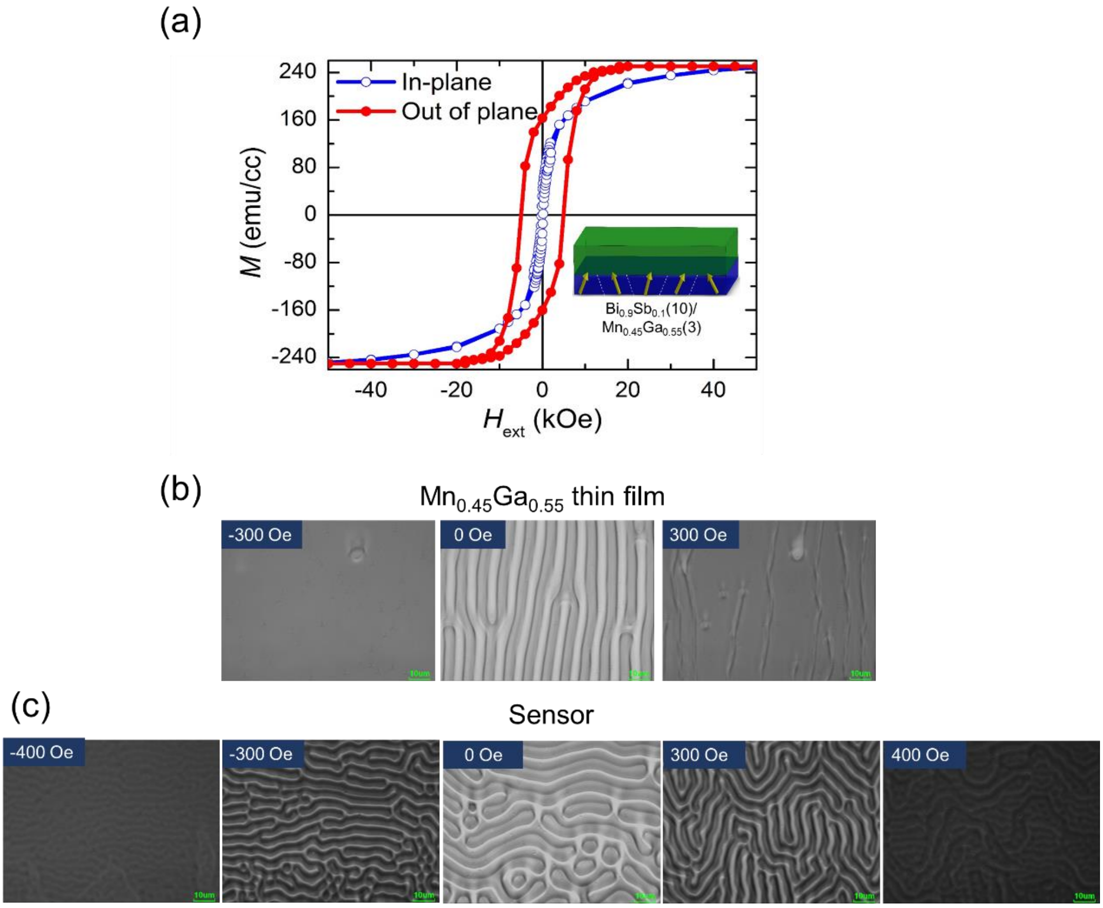

Figure 5.4: (a) In-plane (blue) and out-of-plane (red) magnetization curve of $Bi_{0.9}Sb_{0.1}$ (10) / $Mn_{0.45}Ga_{0.55}$ (3) bilayers. Inset shows the tilting magnetic domains of the $Mn_{0.45}Ga_{0.55}$ layer. (b) In-plane MOKE images of the sensor in contact with the $Mn_{0.45}Ga_{0.55}$ layer. (c) In-plane MOKE images of the sensor without contact with the $Mn_{0.45}Ga_{0.55}$ layer. Here, the magnetic field is applied in-plane.

5.3.2. Magnetic anisotropy of the tilting magnetic domains in $Mn_{0.45}Ga_{0.55}$

In order to see the detail picture of the tilting magnetization in the $Mn_{0.45}Ga_{0.55}$ (3) layer, the anisotropy magnetic energy density of a single domain is studied. It can be expressed by

$$E_{\mathrm{ani}} = -\frac{K_{\mathrm{u}}}{2}\cos 2\phi + \frac{K_4}{4}\cos 4\phi \qquad \textbf{(5.2)}$$

where ϕ is the angle between the magnetization vector of the domain and the z axis, K_{u} is the anisotropy constant (including the shape anisotropy) representing the uniaxial easy axis along the z axis, and K_4 is the anisotropy constant representing the biaxial easy axes at $\phi = \pm 45°$, respectively.

K_{u} and K_4 can be estimated as follows. When the magnetic field is applied in-plane ($H//x$), the total magnetic energy density is given by

$$E = -\frac{K_{\mathrm{u}}}{2}\cos 2\phi + \frac{K_4}{4}\cos 4\phi - MH\sin\phi \qquad \textbf{(5.3)}$$

At a given H, ϕ is determined by solving the equation

$$\frac{dE}{d\phi} = K_{\mathrm{u}}\sin 2\phi - K_4\sin 4\phi - MH\cos\phi = 0 \qquad \textbf{(5.4)}$$

or $$2K_{\mathrm{u}}\sin\phi - 4K_4\cos 2\phi\sin\phi - MH = 0 \qquad \textbf{(5.5)}$$

which is further simplified to

$$H_{\mathrm{u}}\sin\phi - H_4\cos 2\phi\sin\phi - H = 0 \qquad \textbf{(5.6)}$$

where H_{u} the uniaxial anisotropy field and H_4 the biaxial anisotropy field defined by $K_{\mathrm{u}} = \frac{1}{2}H_{\mathrm{u}}M$, $K_4 = \frac{1}{4}H_4M$. When H approaches the in-plane saturation magnetic field $H_{\mathrm{s\text{-}x}}$, ϕ reaches 90°, thus

$$H_{\mathrm{u}} + H_{4} = H_{\text{s-x}} \tag{5.7}$$

Similarly, when the magnetic field is applied out-of-plane ($H//z$), the total magnetic energy density is given by

$$E = -\frac{K_{\mathrm{u}}}{2}\cos 2\phi + \frac{K_{4}}{4}\cos 4\phi - MH\cos\phi \tag{5.8}$$

Solving $\frac{\mathrm{d}E}{\mathrm{d}\phi} = 0$, Eq. 5.8 can be rewritten as

$$2K_{\mathrm{u}}\cos\phi - 4K_{4}\cos 2\phi\cos\phi + MH = 0 \tag{5.9}$$

or

$$H_{\mathrm{u}}\cos\phi - H_{4}\cos 2\phi\cos\phi + M = 0 \tag{5.10}$$

When H approaches the out-of-plane saturation magnetic field $H_{\text{s-z}}$, ϕ reaches 0°, thus

$$-H_{\mathrm{u}} + H_{4} = H_{\text{s-z}}\,. \tag{5.11}$$

H_{u} = 10 kOe and H_{4} = 30 kOe were obtained by solving Eq. 5.7 and Eq. 5.11 using $H_{\text{s-x}}$ = 40 kOe, and $H_{\text{s-z}}$ = 20 kOe (see Fig. 5.4(a)).

This magnetic energy density function captures most of the important features of the magnetization curves in Fig. 5.4(a). Figure 5.5(a-d) plot the E/M of the domain as a function of ϕ when (a) no magnetic field is applied, (b) an in-plane magnetic field of 4 kOe is applied, (c) an in-plane magnetic field of 40 kOe is applied, and (d) an out-of-plane magnetic field of 20 kOe is applied. In Fig. 5.5(a), the magnetization vector has 4 equivalent stable positions at ϕ = ±35° and ±145°. The potential barrier between +35°/ -35° domains is much smaller than that between 35°/145° domains. This suggests the coexistence of ±35° domains as schematically shown in the inset of Fig. 5.4(a). Figure 5.5(b) shows that when an in-plane magnetic field of 4 kOe is applied, the barrier between +35°/ -35° domains disappears. Thus, Figs. 5.5(a) and 5.5(b) explain the observation that the in-plane magnetization shows small remanence, but rapidly increases up to an in-plane magnetic field of 4 kOe. When a large in-plane magnetic field of 40 kOe is applied, the magnetization vector approaches 90° as shown in Fig. 5.5(c). Similarly, when a large out-of-plane magnetic field of 20 kOe is applied, the magnetization vector approaches 0° as shown in Fig. 5.5(d).

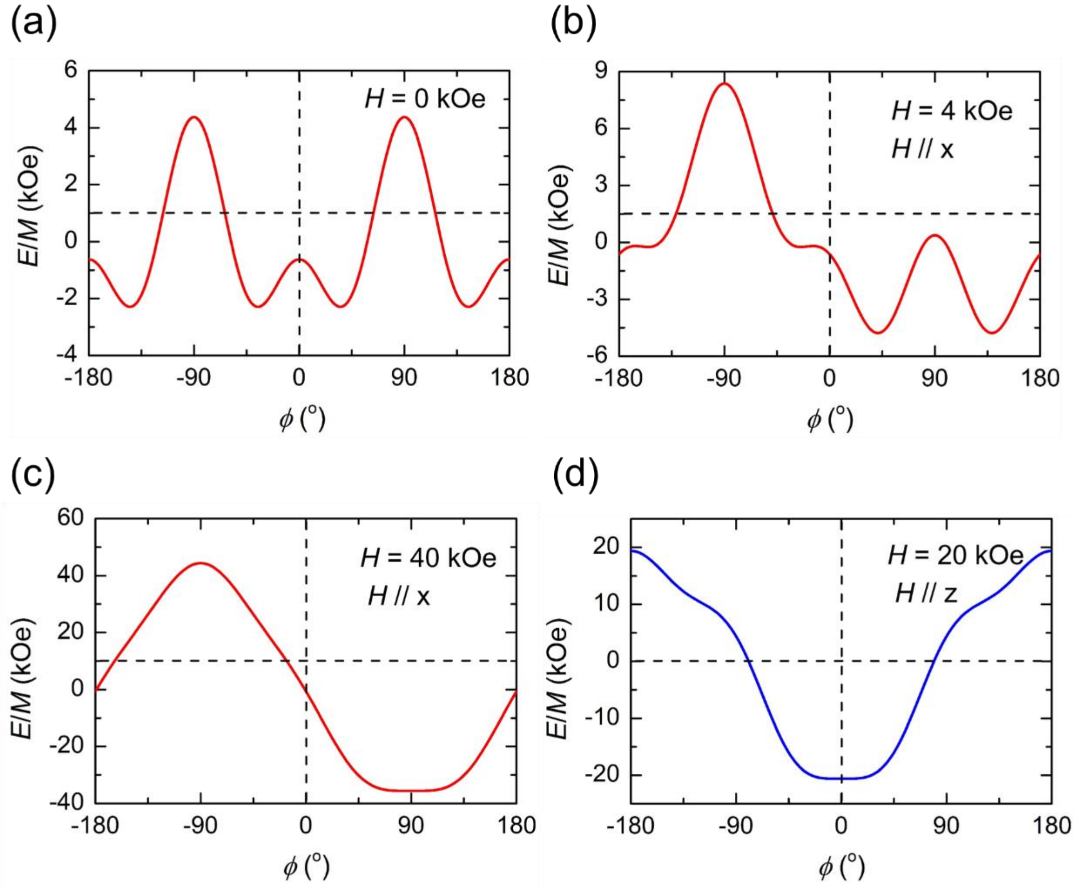

Figure 5.5: E/M of a single domain of the $Mn_{0.45}Ga_{0.55}$ layer as a function of ϕ, when (a) no magnetic field is applied, (b) an in-plane magnetic field of 4 kOe is applied, (c) an in-plane magnetic field of 40 kOe is applied, and (d) an out-of-plane magnetic field of 20 kOe is applied.

Figures 5.6(a) and 5.6(b) compare the magnetization hysteresis curves of the $Mn_{0.45}Ga_{0.55}$ layer in Fig. 5.4(a), measured by SQUID (circles) and theoretical calculation results using the single domain model (solid lines), when the magnetic field was applied in-plane and out-of-plane, respectively. One can see that the theoretical curves reproduce the experiment results when the magnetic field is higher than 4 kOe (in-plane) or 12 kOe (out of plane). However, at low magnetic fields, clear deviation from the single domain model is observed. Particularly, the remanences and the coercive forces are smaller than those predicted by the single domain model. These indicates that the sample should be in the multi domain structure at low magnetic fields so that the static magnetic energy can be reduced, and the magnetization reversal process occurs through domain wall movement rather than single domain coherent rotation.

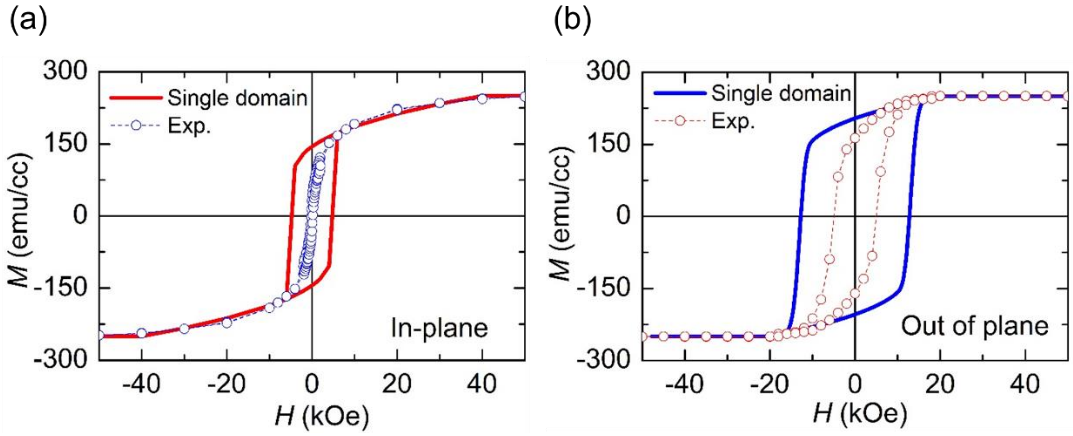

Figure 5.6: Magnetization hysteresis curves of the $Mn_{0.45}Ga_{0.55}$ layer measured by SQUID (circles) and theoretical calculation results (solid lines) using the single domain model, when the magnetic field is applied (a) in-plane and (b) out-of-plane, respectively.

5.3.3. SOT effect in $Bi_{0.9}Sb_{0.1}$ - $Mn_{0.45}Ga_{0.55}$ bilayers under a titling external magnetic field

The initial rise of the in-plane magnetization at the small in-plane H_{ext} indicates reorientation of the magnetic domains toward the in-plane H_{ext} direction, while the slow increase at the in-plane H_{ext} > 4 kOe reflects their tilting toward the horizontal direction. This unique magnetic behaviors of the $Mn_{0.45}Ga_{0.55}$ layer allow us to directly evaluate H_{so}. Figure 5.7(a) shows the R_H of a 100 μm × 50 μm Hall bar made from the bilayer in Fig. 5.4(a) under nearly perpendicular H_{ext} at room temperature. Before the measurements, an in-plane magnetic field of +8 kOe is applied to induce a small remanent in-plane M_x component of the $Mn_{0.45}Ga_{0.55}$ layer (see Fig. 5.3(a) and the inset in Fig. 5.4(a)), then θ was reduced to ~ 2° and the magnetic field was swept from +8 kOe to – 8 kOe and vice-verse. Since the direction of the damping-like spin-orbit field H_{so} is given by $-\sigma \times m$, where σ is the spin polarization unit vector of the spin current along the *y* direction and *m* is the unit vector of the magnetization direction, there is an out-of-plane component $H_{so\text{-}z}$ of the spin-orbit field associating with M_x.

The existence of such $H_{so\text{-}z}$ component can be seen in Fig. 5.7(a); the remanence and coercive force of the R_H hysteresis systematically increase with increasing positive *J*. This clearly cannot be explained by Joule heating which can only reduce but not enhance the remanent R_H and coercive force. On the other hand, the R_H hysteresis was reduced remanence and coercive force at a negative $J = -7.7\times10^5$ A/cm^2.

In addition to the damping-like spin-orbit field H_{so}, there is possibly a field-like spin-orbit field H_{FL} generated by BiSb. However, H_{FL} can be neglected by analyzing the magnitude of the R_H loops of the $Bi_{0.9}Sb_{0.1}$ (10) / $Mn_{0.45}Ga_{0.55}$ (3) Hall bar under a slightly tilting perpendicular magnetic field (θ = 2° toward the *x* direction). Here, a situation was considered when H_{FL} was comparable with H_{so}, i.e. its strength was ~ 1 kOe at the highest

J = 13.8×10^5 A/cm^2. Since H_{FL} is along the y direction, it can generate a non-zero M_{y} component for the $\mathrm{Mn_{0.45}Ga_{0.55}}$ (3) layer. Therefore, there would be contribution from the planar Hall resistance R_{PHE} in addition to the anomalous Hall resistance R_{AHE} to the total Hall resistance R_{H}. Unlike H_{so}, however, the direction of H_{FL} depends only on the direction of J, but not M. Figures 5.7(c) and 5.7(d) show the direction of M_{x}, M_{y}, and M_{z} at a perpendicular H_{ext} = 8 kG and -8 kG, respectively. In Fig. 5.7(c), $M_{\mathrm{x}} > 0$, $M_{\mathrm{y}} > 0$, and $M_{\mathrm{z}} > 0$, thus

$$R_{\mathrm{H}}(8\ \mathrm{kOe}) = R_{\mathrm{PHE}} \sin 2\phi + R_{\mathrm{AHE}} \qquad \textbf{(5.12)}$$

where $\phi = \tan^{-1}(M_{\mathrm{y}}/M_{\mathrm{x}})$. In Fig. 5.7(d), $M_{\mathrm{x}} < 0$, $M_{\mathrm{y}} > 0$, and $M_{\mathrm{z}} < 0$, thus

$$R_{\mathrm{H}}(-8\ \mathrm{kOe}) = R_{\mathrm{PHE}} \sin[2(\pi-\phi)] - R_{\mathrm{AHE}} = -R_{\mathrm{PHE}} \sin 2\phi - R_{\mathrm{AHE}} \qquad \textbf{(5.13)}$$

That means the magnitude of the R_{H} loop is given by $R_{\mathrm{PHE}} \sin 2\phi + R_{\mathrm{AHE}}$, and would be enhanced by the amount of $R_{\mathrm{PHE}} \sin 2\phi$. As a result, one would expect that the magnitude of the R_{H} loops would systematically increase with increasing J. However, as seen in Fig. 5.7(a), the magnitude of the R_{H} loops does not change when J is increased from 0.2×10^5 A/cm^2 to 13.8×10^5 A/cm^2. This indicates that H_{FL} is negligible, and that R_{H} has only contribution from R_{AHE}.

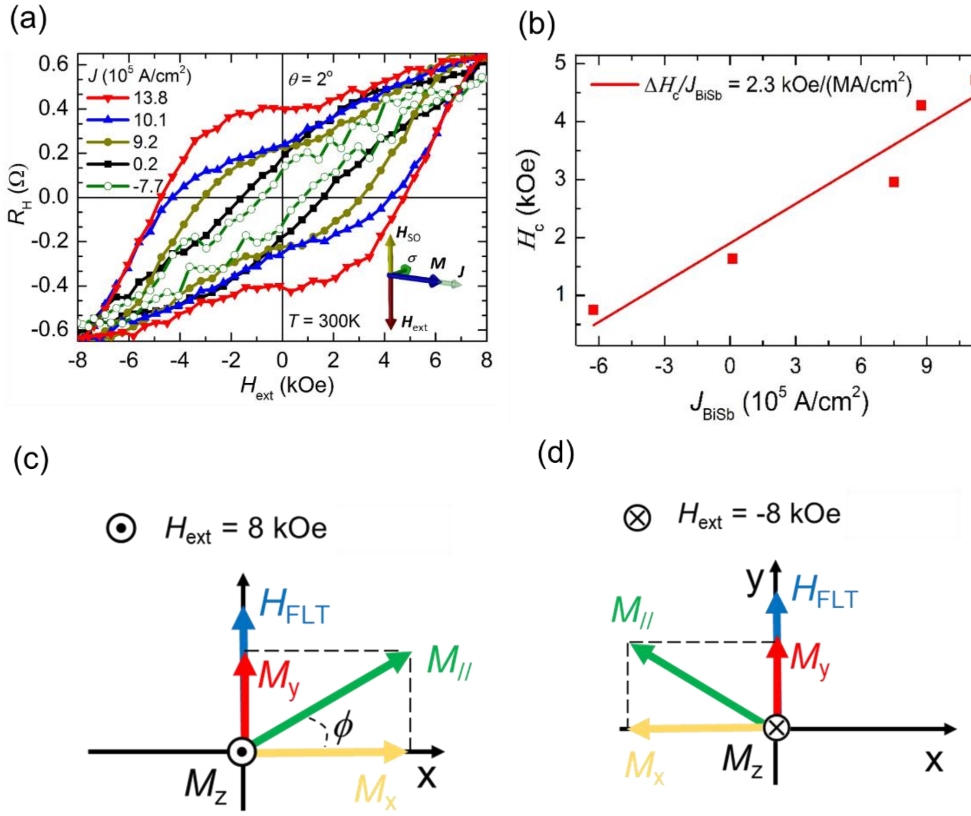

Figure 5.7: (a) R_H of a 100 μm × 50 μm Hall bar of the bilayer under a slightly tilting perpendicular magnetic field ($\theta = 2°$), measured with various current density J = -7.7 – 13.8×10^5 A/cm^2 at 300 K. Inset shows the perpendicular spin-orbit field H_{so} acting on the magnetization vector M at $H_{ext} = -H_c$ (coercive force) in the macrospin picture. (b) Coercive force H_c and its change ΔH_c as functions of the current density J_{BiSb} in the $Bi_{0.9}Sb_{0.1}$(10)/$Mn_{0.45}Ga_{0.55}$(3) bilayer. (c), (d) Direction of M_x, M_y, and M_z under a slightly tilting perpendicular magnetic field H_{ext} (θ = 2° toward the x direction), assuming a non-zero field-like spin-orbit field H_{FL} at H_{ext} = 8 kOe and H_{ext} = -8 kOe, respectively.

5.3.4. SOT effect in $Bi_{0.9}Sb_{0.1}$ - $Mn_{0.45}Ga_{0.55}$ bilayers under an in-plane external magnetic field

To further confirm the effect of $H_{so\text{-}z}$, R_H was measured under an in-plane H_{ext} (θ=90°). Figures 5.8(a) and 5.8(b) show the R_H-H_{ext} (θ=90°) hysteresis at J = 13.8×10^5 A/cm^2 and J = -13.8×10^5 ×10^5 A/cm^2, respectively. One can see that R_H rapidly increases up to H_{ext} ~ 4 kOe, and then gradually decreases at H_{ext} > 4 kOe. This behavior is consistent with the in-plane magnetization curve shown in Fig. 5.4(a); at H_{ext} = 0~4 kOe, the magnetic domains are rapidly reoriented toward the *x*-directions, so that $H_{so\text{-}z}$ and R_H reach their maximum value at 4 kOe. At H_{ext} > 4 kOe, the whole MnGa layer becomes a single domain, while the magnetization begins tilting toward the *x* direction and R_H decreases.

Furthermore, $H_{so\text{-}z}$ and R_H switch its directions when direction of M_x or J is changed. As shown in Fig. 5.8(c), the H_{so} direction can be switched between 4 different configurations by changing the direction of M_x (by sweeping the in-plane external field from positive to negative and vice-verse), or by changing the direction of the spin-polarization of the spin Hall current (changing the charge current direction from positive to negative). These results definitely demonstrate that the symmetry of H_{so} follows that of $M\times\sigma$, consistent with the symmetry of SOT.

Note that the polarity switching of R_H when direction of M_x or J is changed was observed not only in the low field range of $|H_{ext}|$ <4 kOe (multi-domain state), but also in the high field range of $|H_{ext}|$ > 4 kOe (single domain state). This eliminates the possibility of artifacts due to the topological Hall effect [12, 13, 14] or the tunneling planar Hall effect [15], since those effects require inhomogeneous magnetization to occur in our device, either in the form of spatially varying magnetic domains or skyrmions.

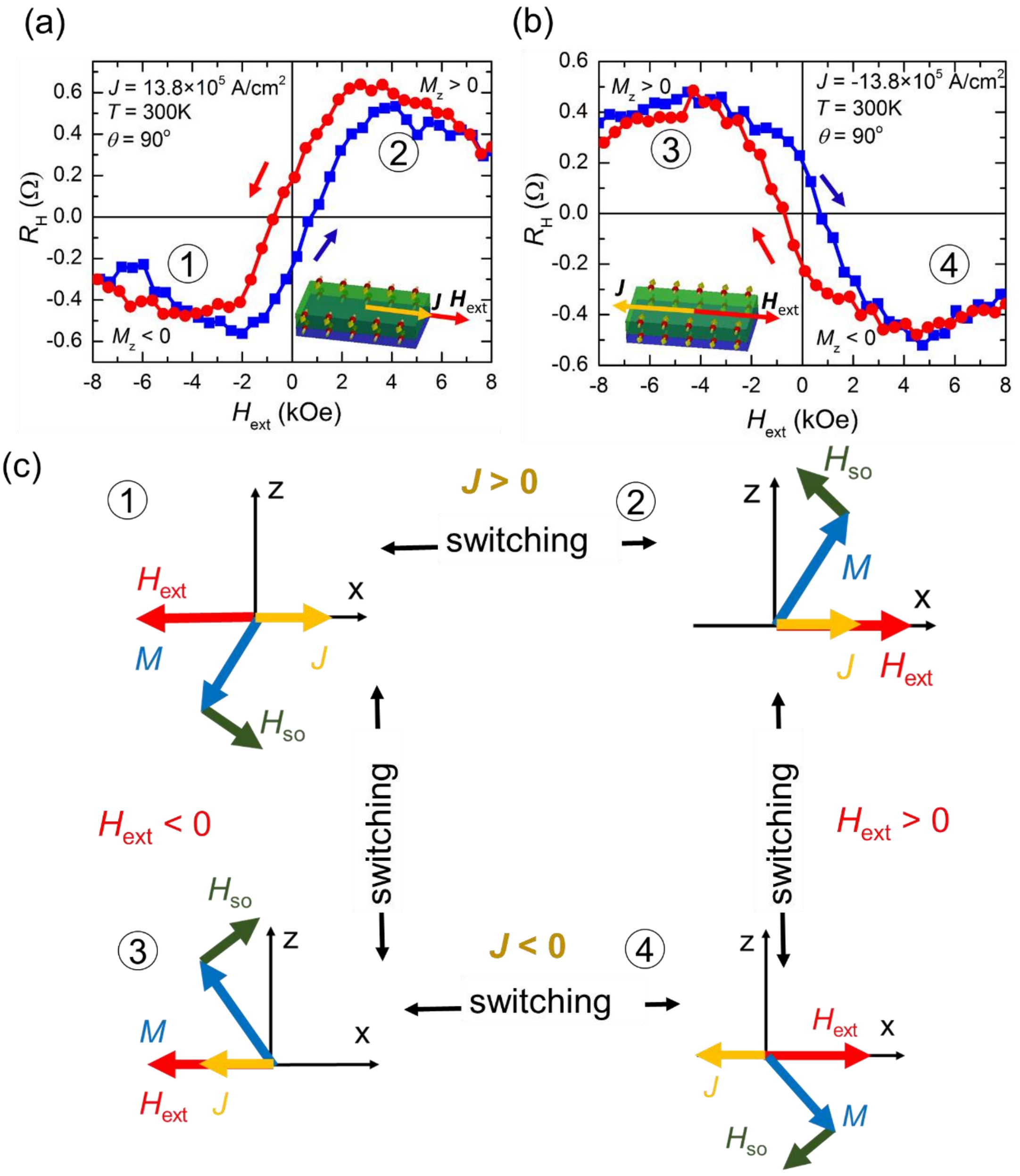

Figure 5.8: (a), (b) R_{H} as a function of an in-plane H_{ext} ($\theta = 90°$) at J = +13.8×10^5 A/cm^2 and -13.8×10^5 A/cm^2, respectively. (c) Symmetry of $H_{SO} \sim M \times \sigma$ confirmed by switching the in-plane magnetic field direction or the current direction.

5.3.5. Spin Hall angle evaluation

Next, the spin Hall angle was evaluated from data in Fig. 5.7(a). For the sake of simplicity, a macrospin model with coherent magnetization rotation was first assumed. At H_{ext} = -$H_c(J)$ (the coercive force at a given J), the net perpendicular magnetization component is zero, so there is only the in-plane magnetization component. The situation at H_{ext} = -$H_c(J)$ is shown in the inset of Fig. 5.7(a). At this point, H_{so} points to the z direction and counters H_{ext}. Thus, the macrospin model predicts that the shift of the coercive ΔH_c is equal to H_{so}. In reality, however, the $Mn_{0.45}Ga_{0.55}$ layer is in a multi-domain state at low magnetic fields, and magnetization reversal occurs through domain wall movement rather than coherent magnetization rotation. Nevertheless, full micromagnetic simulations have shown that the relation $H_{so} = \Delta H_c$ gives a good estimation for H_{so} with less than 5% of uncertainty in a Pt/BaM ferrite bi-layer [16]. Furthermore, the macroscopic model has been used to remarkably reproduce the experimental switching phase diagram due to SOT effect in Pt/Co bilayers [17]. This confirms the validity of this relation even though it is derived from a simple macrospin coherent rotation model.

H_{so} can also be estimated from the R_H-H_{ext} data in Figs. 5.8(a)-2(b) in the high in-plane field range ($|H_{ext}| > 4$ kOe), when the $Mn_{0.45}Ga_{0.55}$ layer becomes a single domain and the macrospin model is applicable. The obtained average value of $|H_{so}| = 2.9 – 3.4$ kOe for $J = \pm 13.8 \times 10^5$ A/cm^2 are within 10% of uncertainty from that obtained by assuming $H_{so} = \Delta H_c = 3.1$ kOe for $J = 13.8 \times 10^5$ A/cm^2 in Fig. 5.7(a) (see appendix A). Thus, in the following, the relation $H_{so} = \Delta H_c$ was used to estimate the spin Hall angle. Figure 5.7(b) plots ΔH_c obtained in Fig. 5.7(a) as a function of J_{BiSb}. The slope H_{so}/J_{BiSb} = 2.3 kOe/(MA/cm^2) was obtained at room temperature. This value is much larger than those of heavy metals and TIs reported before, such as Ta ~ 6.8 Oe/(MA/cm^2) in Fe (1.1)

/ Ta (7.2), Pt ~ 2.9 Oe/(MA/cm^2) in Fe (0.5) / Pt (2.3) [18], and Bi_xSe_{1-x} ~100 Oe/(MA/cm^2) in CoFeB (5) / Bi_xSe_{1-x} (4) [3]. The room-temperature spin Hall angle θ_{SH}, calculated by

$$\theta_{\mathrm{SH}} = \frac{2e}{\hbar} M_{\mathrm{MnGa}} t_{\mathrm{MnGa}} \frac{H_{\mathrm{SO}}}{J_{\mathrm{BiSb}}} \tag{5.14}$$

where M_{MnGa} and t_{MnGa} are the magnetization and thickness of $Mn_{0.45}Ga_{0.55}$, respectively, J_{BiSb} is the current density flowing in BiSb layer. The estimated spin Hall angle is 52, which is the highest value reported so far. Our data also show that θ_{SH} of BiSb has the same sign as those of $(Bi_{0.5}Sb_{0.5})_2Te_3$ [19], Bi_2Se_3 [2] and Pt [17].

5.4. Magnetization switching by ultra-low current density

In order to demonstrate magnetization switching by ultra-low current density using the large spin Hal effect of BiSb, a 100 μm × 50 μm Hall bar of a $Bi_{0.9}Sb_{0.1}$ (5) / $Mn_{0.45}Ga_{0.55}$ (3) bilayer was prepared. Figure 3(a) and 3(b) demonstrate the SOT switching of the MnGa layer when applying 100 ms pulse currents to the Hall bar and an in-plane H_{ext} = + 3.5 kOe and -3.5 kOe, respectively. One can see that clear switching at an average critical current density of $J = 1.5\times10^6$ A/cm^2 ($J_{\mathrm{BiSb}} = 1.1\times10^6$ A/cm^2). Here, the critical current density is defined at which the Hall resistance changes sign. Note that the switching of R_{H} between ±1 Ω corresponds to full magnetization switching. Furthermore, the switching direction is reversed when the in-plane H_{ext} direction is reversed, consistent with the behavior of SOT switching. The observed critical current density is much smaller than those of Ta (5) / MnGa (3) ($J = 1.1\times10^8$ A/cm^2) [20], IrMn (4) / MnGa (3) ($J = 1.5\times10^8$ A/cm^2) [21] and Pt (2) / MnGa (2.5) ($J = 5.0\times10^7$ A/cm^2) [22].

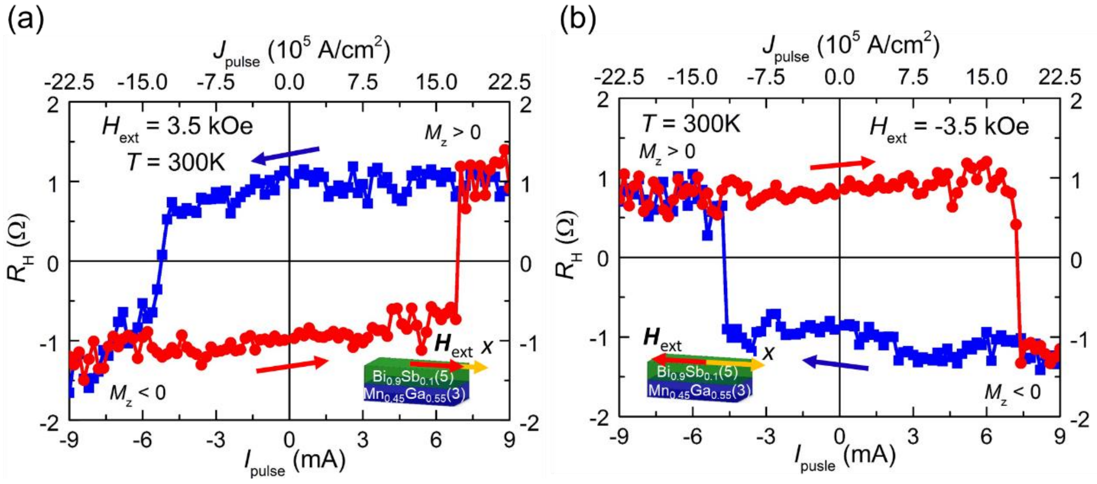

Figure 5.9: (a), (b) R_H of a 100 μm × 50 μm Hall bar of the $Bi_{0.9}Sb_{0.1}$ (5) / $Mn_{0.45}Ga_{0.55}$ (3) bilayer under 100 ms pulse currents and an in-plane H_{ext} of +3.5 kOe and -3.5 kOe, respectively.

Table 5.1: Room-temperature spin Hall angle θ_{SH}, conductivity σ, and spin Hall conductivity σ_{SH} of several heavy metals and TIs.

	θ_{SH}	σ ($\Omega^{-1}m^{-1}$)	σ_{SH} ($\frac{\hbar}{2e}\Omega^{-1}m^{-1}$)
β-Ta [1]	0.15	5.3×10^5	0.8×10^5
β-W [23]	0.4	4.7×10^5	1.9×10^5
Pt [17]	0.08	4.2×10^6	3.4×10^5
Bi_2Se_3 [2]	2-3.5	5.7×10^4	$1.1\text{-}2.0\times10^5$
Bi_xSe_{1-x} [3]	18.8	7.8×10^3	1.47×10^5
$Bi_{0.9}Sb_{0.1}$ (this work)	**52**	**2.5×10^5**	**1.3×10^7**

5.5. Comparisons with other spin Hall materials

BiSb has many characteristics that make it the best candidate for the pure spin current source in SOT-MRAM. Its conductivity is comparable to typical ferromagnetic and non-magnetic metals used in MRAM, while its spin Hall angle is as large as 52 at room temperature. It can be grown well on ferromagnetic metals without creating a magnetic dead layer. Table 5.1 summarizes σ, θ_{SH}, and σ_{SH} of several heavy metals and TIs at room temperature. In term of σ_{SH}, which is considered as the figure of merit for spin Hall materials, BiSb outperforms other TIs by a factor of 100 and the nearest competitor (Pt) by a factor of 30. Although there are reports of room-temperature SOT switching by other TIs in Bi_2Se_3/CoTb [24], Bi_2Se_3/NiFe [25], and Bi_xSe_{1-x}/CoFeB [3], the ferromagnets used in those works have a low coercive force of only a few 10 Oe ~ a few 100 Oe, which is much smaller than that (a few kOe) in realistic MRAM. Using BiSb, both very large spin-orbit field of 2.3 kOe/(MA/cm^2) and SOT switching at a low critical current density of 1.5×10^6 A/cm^2 have been demonstrated by using the MnGa as ferromagnetic layer with much higher PMA (40 ~ 50 kOe) and coercive force (> 1.6 kOe) than those used in previous experiments. These double check the very large spin Hall effect of BiSb.

The observation of the very large spin Hall effect in BiSb leaves many open questions about the physics of the spin Hall effect in TIs. Even though stronger spin-orbit interaction and larger spin Hall effect are expected for BiSb than Bi_3Se_2 or $(Bi,Sb)_3Te_2$ thanks to its very small band gap, the observation of $\sigma_{SH} = 1.3\times10^7 \frac{\hbar}{2e}\Omega^{-1}m^{-1}$ is unexpected. Because of the very small band gap, the electric current flows in both the surface and the bulk of BiSb, thus contribution of both surface and bulk spin Hall effect should be considered. However, first-principle calculation of the bulk intrinsic spin Hall effect of

BiSb yields a maximum value of $9.8\times10^4 \frac{\hbar}{2e}\Omega^{-1}\text{m}^{-1}$ when the Fermi level is in the band gap, which can account for only 0.74% of the observed value (although very large bulk intrinsic $\theta_{\text{SH}} = \frac{2e}{\hbar}\frac{\sigma_{\text{SH}}}{\sigma}$ is possible from the calculation since the bulk $\sigma \sim 0$ at zero temperature) [26]. Furthermore, the bulk extrinsic mechanism such as side-jump or skew-scattering is unlikely the main mechanism given the high carrier mobility and low scattering rate in BiSb alloys. Therefore, this suggests that the topological surface states of BiSb(012) are mainly responsible for the observed very large spin Hall effect in BiSb. It was theoretically predicted [27] and later experimentally confirmed by ARPES measurement [28] that the BiSb(012) surface has three Dirac cones at the $\overline{\Gamma}$, $\overline{\text{X}}$, and $\overline{\text{M}}$ point, while there is only one Dirac cone at the $\overline{\Gamma}$ point on the BiSb(001), Bi_2Se_3(001), and Bi_2Se_3(012) surface. This unique "valley degree of freedom" of the BiSb(012) surface may be related to the origin of the observed SHE. Detailed observation of the BiSb(012) surface states by spin-resolved ARPES is needed for unlocking the secret of the very large spin Hall effect in BiSb(012).

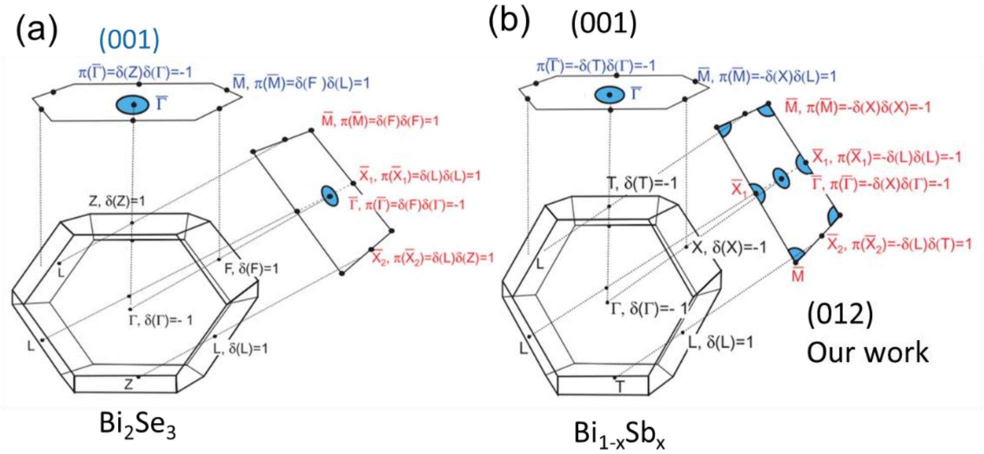

Figure 5.10: (a), (b) Topological prediction for the surface electronic structure of Bi_2Se_3 and $\text{Bi}_{1\text{-}x}\text{Sb}_x$ ($0.09 < x < 0.22$), respectively. Reproduced with permission [28].

5.6. Summary

In this chapter, the huge spin Hall angle in BiSb thin films with θ_{SH} ~ 52, and spin Hall conductivity σ_{SH} ~ $1.3\times10^{7}\frac{\hbar}{2e}\Omega^{-1}m^{-1}$ at room temperature was observed. BiSb not only has large σ ~ $2.5\times10^{5}\ \Omega^{-1}m^{-1}$ but also can generate a very large spin-orbit field of 2.3 kOe/(MA/cm^2) in $Bi_{0.9}Sb_{0.1}$ / MnGa bi-layers. These results underline the potential of BiSb as good spin Hall material in SOT-MRAM. As over ten years have passed from the proposals [29, 30] and the realization of TIs [31], BiSb emerges as a promising candidate for SOT-MRAM based on TIs.

References

1. L. Liu, C. F. Pai, Y. Li, H. W. Tseng, D. C. Ralph, and R. A. Buhrman, Science **336**, 555 (2012).

2. A. R. Mellnik, J. S. Lee, A. Richardella, J. L. Grab, P. J. Mintun, M. H. Fischer, A. Vaezi, A. Manchon, E.-A. Kim, N. Samarth, and D. C. Ralph, Nature **511**, 449 (2014).

3. DC. Mahendra, R. Grassi, J. Y. Chen, M. Jamali, D. R. Hickey, D. Zhang, Z. Zhao, H. Li, P. Quarterman, L. Yang, M. Li, A. Manchon, K. A. Mkhoyan, T. Low, and J. P. Wang, Nat. Mater. **17**, 800 (2018).

4. J. C. Y. Teo, L. Fu, and C. L. Kane, Phys. Rev. B **78**, 045426 (2008).

5. Y. Ueda, N. H. D. Khang, K. Yao, and P. N. Hai. Appl. Phys. Lett. 110, 062401 (2017).

6. D. Hsieh, D. Qian, L. Wray, Y. Xia, Y. S. Hor, R. J. Cava, and M. Z. Hasan, Nature **452**, 970 (2008).

7. T. Hirahara, Y. Sakamoto, Y. Saisyu, H. Miyazaki, S. Kimura, T. Okuda, I. Matsuda, S. Murakami, and S. Hasegawa, Phys. Rev. B. **81**, 165422 (2010).

8. A. Nishide, A. A. Taskin, Y. Takeichi, T. Okuda, A. Kakizaki, T. Hirahara, K. Nakatsuji, F. Komori, Y. Ando, and I. Matsuda*,* Phys. Rev. B **81**, 041309 (2010).

9. A. A. Taskin, Y. Ando, Phys. Rev. B **80**, 085303 (2009).

10. A. A. Taskin, K. Segawa, and Y. Ando, Phys. Rev. B **82**, 121302 (2010).

11. L. J. Zhu, S. H. Nie, and J. H. Zhao, Chin. Phys. B **22**, 118505 (2013).

12. P. Bruno, V. K. Dugaev, and M. Taillefumier, Phys. Rev. Lett. **93**, 096806 (2004).

13. K. Yasuda, R. Wakatsuki, T. Morimoto, R. Yoshimi, A. Tsukazaki, K. S. Takahashi, M. Ezawa, M. Kawasaki, N. Nagaosa, and Y. Tokura, Nat. Phys. **12**, 555 (2016).

14. B. M. Ludbrook, G. Dubuis, A. H. Puichaud, B. J. Ruck, and S. Granville, Sci. Rep. **7**, 13620 (2017).

15. B. Scharf, A. M. Abiague, J. E. Han, E. M. Hankiewicz, and I. Žutić, Phys. Rev. Lett.

117, 166806 (2016).

16. P. Li, T. Liu, H. Chang, A. Kalitsov, W. Zhang, G. Csaba, W. Li, D. Richardson, A. DeMann, G. Rimal, H. Dey, J. S. Jiang, W. Porod, S. B. Field, J. Tang, M. C. Marconi, A. Hoffmann, O. Mryasov, and M. Wu, Nature Comm. **7**, 12688 (2015).

17. L. Liu, T. Moriyama, D. C. Ralph, and R. A. Buhrman, Phys. Rev. Lett. **106**, 036601 (2011).

18. M. Kawaguchi, K. Shimamura, S. Fukami, F. Matsukura, H. Ohno, T. Moriyama, D. Chiba, and T. Ono, Appl. Phys. Exp. **6**, 113002 (2013).

19. Y. Fan, P. Upadhyaya, X. Kou, M. Lang, S. Takei, Z. Wang, J. Tang, L. He, L. T. Chang, M. Montazeri, G. Yu, W. Jiang, T. Nie, R. N. Schwartz, Y. Tserkovnyak, and K. L. Wang, Nat. Mater. **13**, 699 (2014).

20. K. K. Meng, J. Miao, X. Xu, Y. Wu, J. Xiao, J. Zhao, and Y. Jiang, Sci. Rep. **6**, 38375 (2016).

21. K. K. Meng, J. Miao, X. G. Xu, Y. Wu, X. P. Zhao, J. H. Zhao, and Y. Jiang, Phys. Rev. B **94**, 214413 (2016).

22. R. Ranjbar, K. Z. Suzuki, Y. Sasaki, L. Bainsla, and S. Mizukami, J. J. Appl. Phys. **55**, 120302 (2016).

23. C. F. Pai, L. Liu, Y. Li, H. W. Tseng, D. C. Ralph, and R. A. Buhrman, Appl. Phys. Lett. **101**, 122404 (2012).

24. J. Han, A. Richardella, S. A. Siddiqui, J. Finley, N. Samarth, and L. Liu, Phys. Rev. Lett. **119**, 077702 (2017).

25. Y. Wang, D. Zhu, Y. Wu, Y. Yang, J. Yu, R. Ramaswamy, R. Mishra, S. Shi, M. Elyasi, K. L. Teo, Y. Wu, and H. Yang, Nature Commun. **8**, 1364 (2017).

26. C. Sahin, and M. E. Flatté, Phys. Rev. Lett. **114**, 107201 (2015).

27. J. C. Y. Teo, L. Fu, and C. L. Kane. Phys. Rev. B **78**, 045426 (2008).

28. X. G. Zhu, M. Stensgaard, L. Barreto, W. S. Silva, S. Ulstrup, M. Michiardi, M. Bianchi, M. Dendzik, and P. Hofmann. New J. Phys. **15**, 103011 (2013).

29. C. L. Kane, and E. J. Mele, Phys. Rev. Lett. **95**, 226801 (2005).

30. B. A. Bernevig, T. L. Hughes, and S. C. Zhang, Science **314**, 1757 (2006).

31. M. König, S. Wiedmann, C. Brüne, A. Roth, H. Buhmann, L. W. Molenkamp, X. L. Qi, S. C. Zhang, Science **318**, 766 (2007).

Chapter 6

Topological Hall Effect and Skyrmions in BiSb - MnGa Bilayers

Besides SOT-MRAM, racetrack memory is a very promising candidate for high-density and low-cost magnetic memory. One of innovative types of race track memory utilizes the topological magnetic objects knows as skyrmions. Thanks to their small size (~5-80 nm [1, 2]) and low driving current density (~10^2 A/cm^2 [3]), skyrmions can enable manipulation of information with ultra-low power consumption.

Dzyaloshinskii-Moriya-Interaction (DMI) is the key ingredient to stabilize chiral domains wall of skyrmions, which can give to rise a fictitious magnetic field and can be detected by the topological Hall effect (THE) [4]. Recently, skyrmion-driven THE was observed in B20 compounds [5 - 8] and $SrRuO_3$-$SrIrO_3$ bilayers [9]. Since then, the THE has become an important tool for probing skyrmions. However, although skyrmions generated by bulk DMI have been found in different B20 compounds, they exist only at low temperature. Interfacial DMI in multilayers such as Pt/CoFeB, Pt/Co/Ni/Co and Pt/Co can generate skyrmions even at room temperature [10-14]. Unfortunately, these skyrmions are still meta-stable at zero magnetic field. For realistic application of skyrmions to racetrack memory, stable skyrmions at room temperature under absence of an external magnetic field are required.

This chapter will study the topological Hall effect (THE) in BiSb topological insulator / MnGa bilayers. The interfacial DMI is modulated by controlling the annealing temperature of the MnGa template. The THE observed at room temperature even under absence of an external magnetic field is the strong evidence for the existence of thermodynamically stable skyrmions in MnGa/BiSb bilayers. These results shed light on the role of the interfacial DMI tailored by suitable material choice and growth technique for generation of skyrmions at room temperature.

6.1. Sample preparation

The BiSb/MnGa bilayers were grown by MBE on semi-insulating GaAs(001) substrate with orientation of BiSb(012) // MnGa(001) // GaAs(001). In order to modulate the interfacial DMI, an additional annealing step was added into the growth process as shown in Fig. 6.1. The whole growth process was described as follows. After a thick GaAs buffer layer was grown at 550^{o}C, the substrate was cooled down to 50^{o}C to grown alternative monolayers of Mn-Ga-Mn-Ga. Then, the template of MnGa bilayer was formed by annealing for in 1 min at two different annealing temperatures: t_{an} = 350^{o}C (sample A), and t_{an} = 400^{o}C (sample B). The samples were cooled down again to grow a thick MnGa with a total thickness of 5 nm at 250^{o}C. Finally, a 10-nm BiSb thin film was grown under the substrate temperature of 200^{o}C. The growth of the BiSb/MnGa bilayers was monitored *in situ* by RHEED, and the thickness of BiSb(10)/MnGa(5) (the numbers in parentheses present layer's thickness in nanometers) thin films were controlled by their fluxes and the growing time. To further understand the role of interface between BiSb and MnGa thin film, samples of MnGa(5) thin film without BiSb layer and BiSb(10)/MnGa(5) bilayer without annealing step were also prepared.

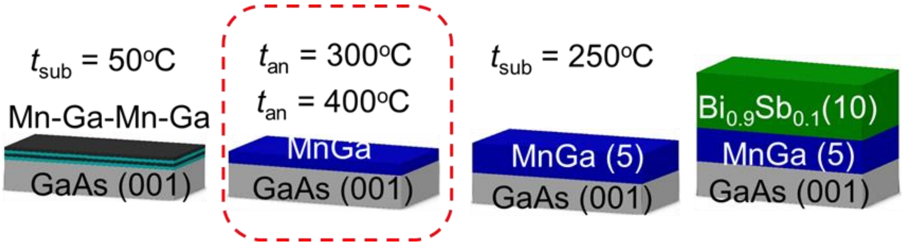

Figure 6.1: Schematic illustration of the growth process. An additional annealing step of the MnGa template layer was employed to tailor the DMI strength.

6.2. Topological Hall effect (THE)

The Hall resistivity can be expressed as

$$\rho_H = R_0 H + \rho_{\mathrm{AHE}} + \rho_{\mathrm{T}} \qquad \textbf{(6.1)}$$

where the first, second and third terms are the ordinary Hall effect, the anomalous Hall effect (AHE) and the THE, respectively. ρ_{H} of the BiSb/MnGa bilayers was measured by using 50×50 μm^2 Hall bars fabricated by convention ultraviolet photolithography and Ar ion milling. Since the THE coexists with the ordinary Hall effect and the AHE, it is necessary to estimate the AHE by measuring the magnetic circular dichroism (MCD) intensity-magnetic field (MCD-H) characteristics. The sample's magnetization was also measured by a superconducting quantum interface device (SQUID).

Figure 6.2(a-b) show the Hall resistivity (blue line), the AHE (red line) estimated by MCD, and the THE (green line) of the MnGa/ BiSb bilayers annealed at 350$^{\mathrm{o}}$C (Fig. 6.2a) and 400$^{\mathrm{o}}$C (Fig. 6.2b) at room temperature. In the Hall resistivity curve, two humps which can be attributed to the THE were clearly observed. While the sample A shows two humps between 0 and 3.5 kOe, the sample B shows two humps between -3 kOe and 3 kOe. This characteristic can be further confirmed in the THE curves. While the peak in the THE curve of the sample A appears at around 1.5 kOe, that of the sample B appears at zero external magnetic field. The existence of the THE in sample B under zero external magnetic field was observed at different temperatures. The magnetic phase diagram of sample B as a function of the external magnetic field (H) and temperature (T) is shown in Fig. 6.2(c). The full Hall resistivity data at each temperature are shown in Fig. 6.3(a-i). The THE amplitude of sample B decreases with decreasing temperature and disappeared at about 125 K as showed in Fig. 6.3(g).

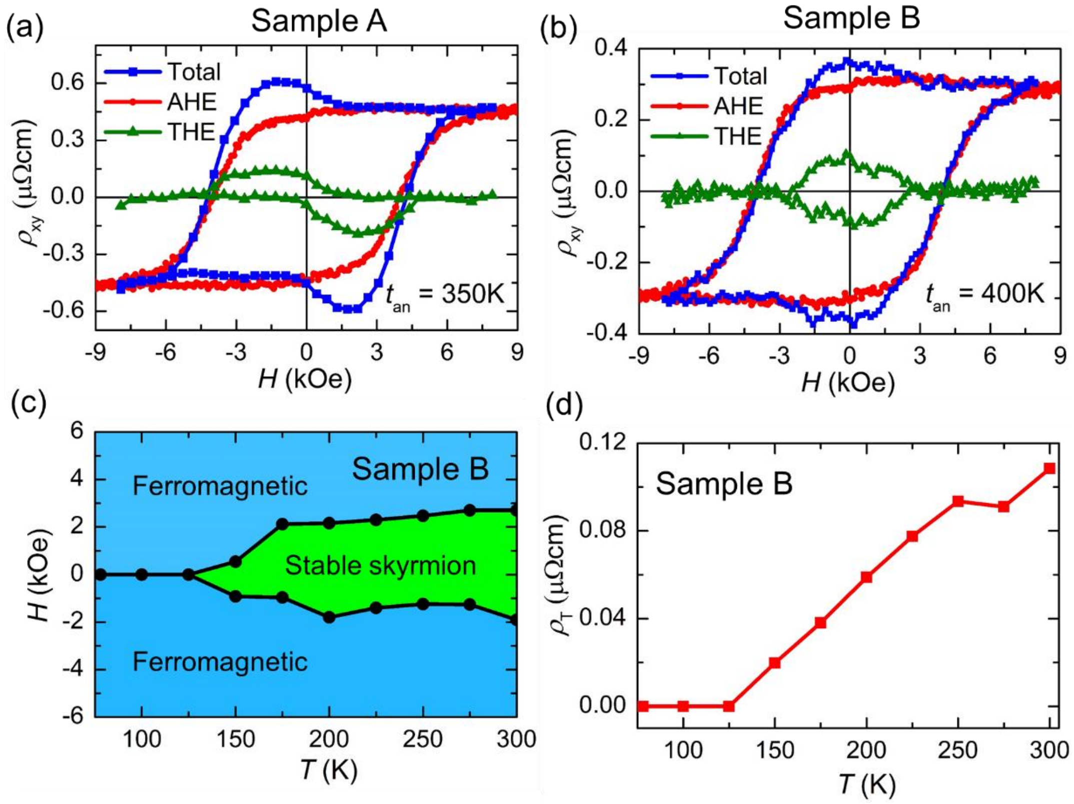

Figure 6.2: (a-b) Room-temperature topological Hall effect (THE) (green lines) extracted from the total Hall effect resistivity (blue lines) and the anomalous Hall effect (AHE) resistivity derived from magnetic circular dichroism intensity-magnetic field measurement (red lines) of MnGa(5 nm)/BiSb(10 nm) bilayers with different MnGa template annealing temperature t_{an} of 350ºC (sample A) and 400ºC (sample B), respectively. (c) Magnetic phase diagram of sample B as a function of the external magnetic field (H) and temperature (T). (d) The topological Hall resistivity ρ_T of sample B as a function of temperature.

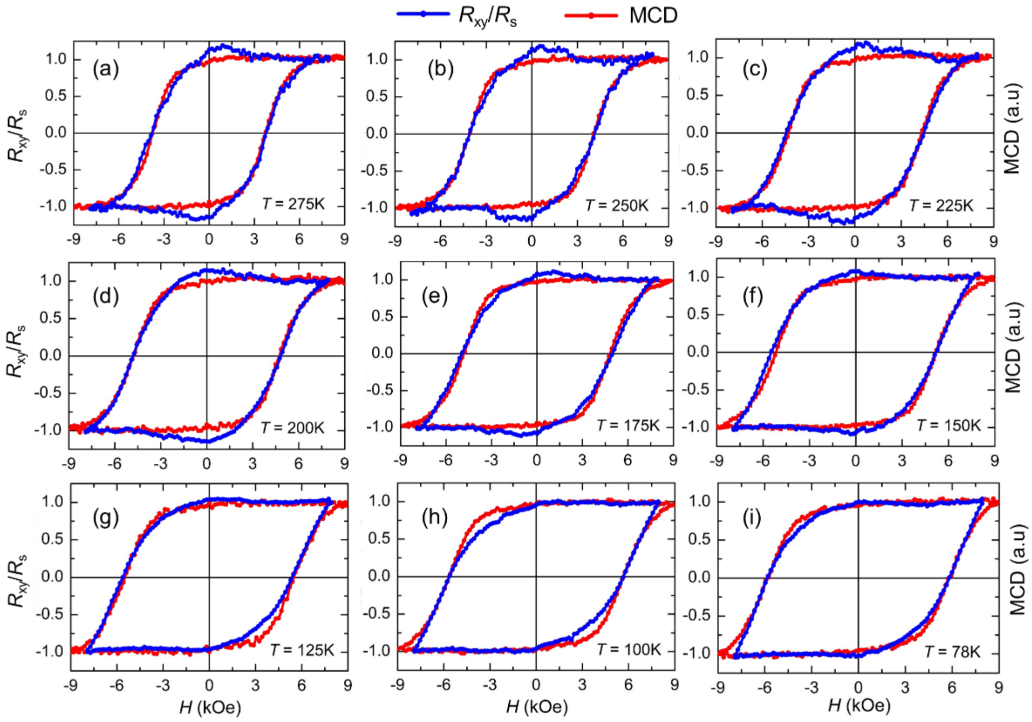

Figure 6.3: (a-i) The Hall resistivity (blue line) and magnetic circular dichroism intensity-magnetic field measurement (red line) of sample B at different temperatures.

Figure 6.4(a) sketches the zero-field magnetic potential in sample A and B. The topological magnetic states can be described by the skyrmion number (S). In the sample A, the energetically lower state is ferromagnet ($S = 0$), and the higher state is skyrmion ($S = 1$). As the results, for the skyrmions to be observed, the skyrmion state potential must be changed from the higher state to the lower state by applying an external magnetic field (H). The meta-stable skyrmion state under zero magnetic field can also be realized by heating or applying a bi-polar pulse magnetic field, or by “blowing” through a wire [15] at room temperature [16]. However, such meta-stable skyrmions are easily erased by applying a large magnetic field. In contrast, the situation in the sample B is quite different. The energetically lower state is skyrmion ($S = 1$), while the higher state is ferromagnet ($S = 0$). As the results, the skyrmions can be stable at zero external magnetic field ($H = 0$ kOe) at room temperature. The stable skyrmions cannot be erased by just applying a large magnetic field; as long as the field is reduced to zero, the skyrmions emerge again.

To prove that the observed THE is due to skyrmions generated by the interfacial DMI of BiSb and MnGa, I measured the Hall resistivity of a reference MnGa(5) single layer annealed at 400^{o}C and a BiSb(10)/MnGa(5) bilayer (sample C) without the annealing step, which are shown in Fig. 6.4(b) and Fig. 6.4(c), respectively. No THE is detected in both samples, confirming that the THE observed in Fig. 6.2(a-b) is due to the interfacial DMI between BiSb and MnGa thin film, not by the bulk DMI in the MnGa thin film, and that strength of their interfacial DMI depends on the annealing condition. Moreover, the critical DMI constant for skyrmion generation D_c can be modulated by changing the thickness of MnGa thin film. The Hall resistivity of a BiSb(10)/MnGa(10) bilayer annealed at 400^{o}C (sample D) is shown in Fig. 6.4(d) and compared with its MCD-H characteristics (as shown Fig. 6.5(a-i)). Only AHE was observed, and there is no THE detected because of the larger D_c as discussed later. All of these observation are consistent with the existence of skyrmions generated by the interfacial DMI.

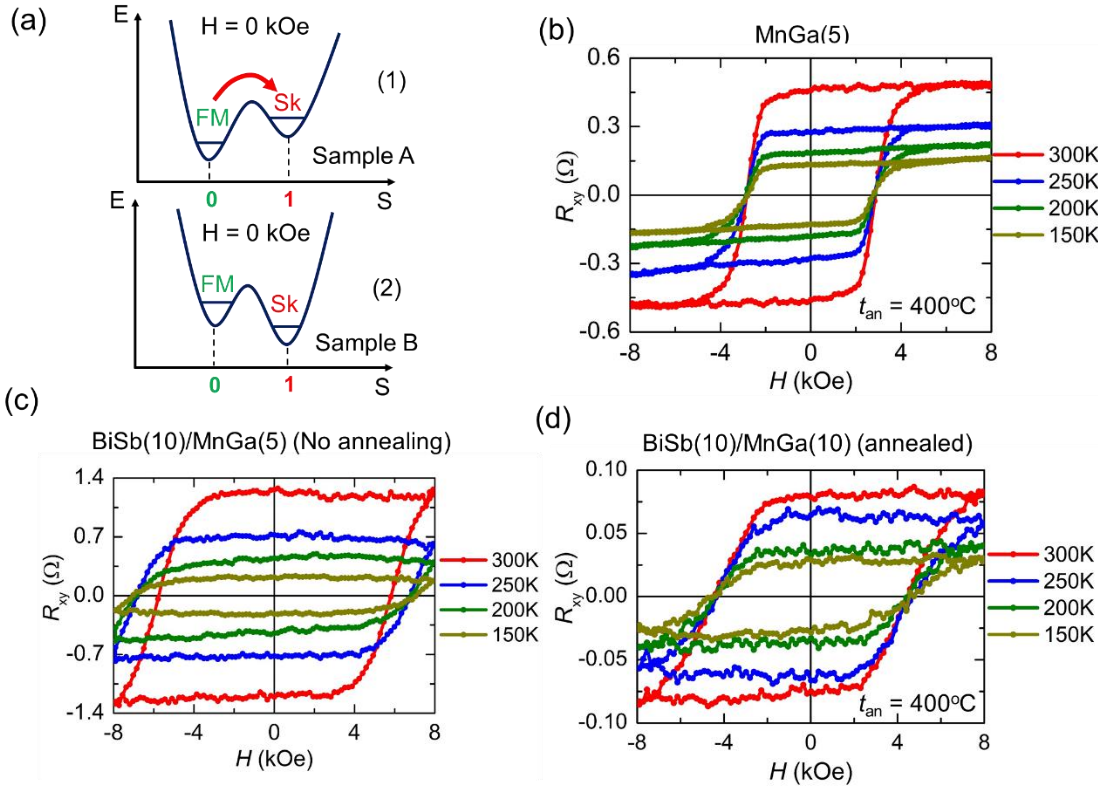

Figure 6.4: (a) Sketch of the zero-field potential for (1) sample A and (2) sample B. (b-d) Hall resistivity of a MnGa(5) single layer annealed at 400°C, a BiSb(10)/MnGa(5) bilayer without the annealing step (sample C) and a BiSb(10)/MnGa(10) bilayer annealed at 400°C (sample D).

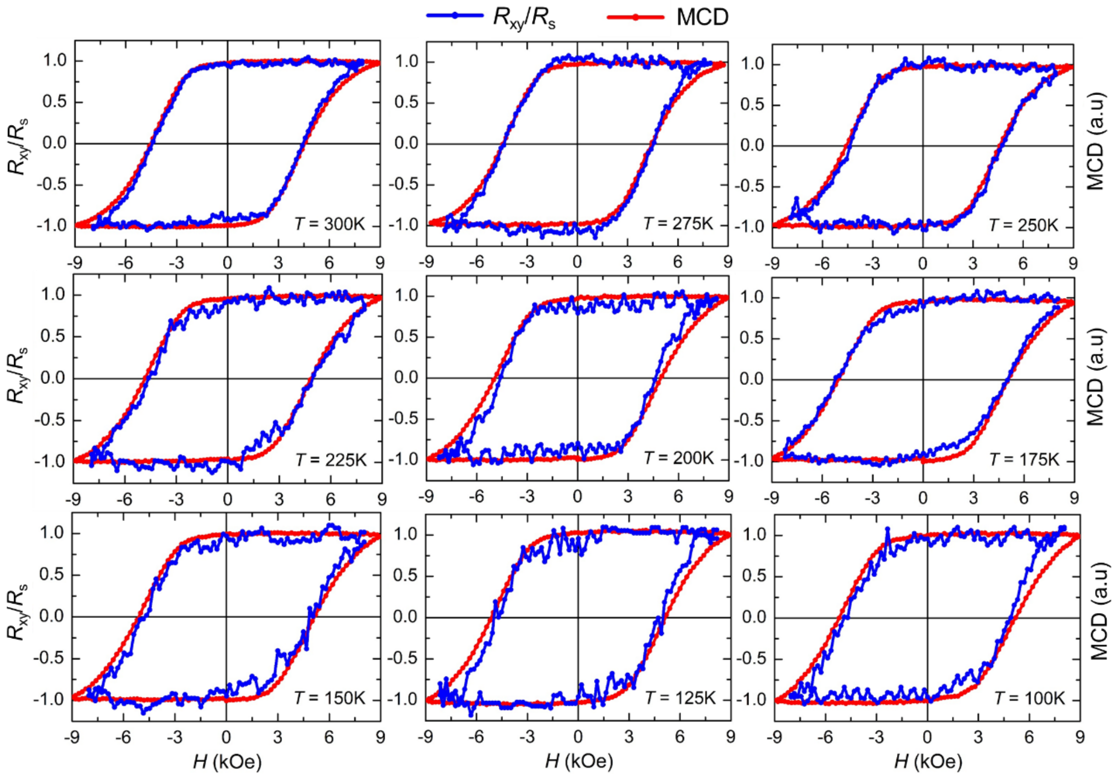

Figure 6.5: The Hall resistivity (blue line) and magnetic circular dichroism intensity-magnetic field measurement (red line) of the BiSb(10)/MnGa(10) bilayer (sample D) annealed at 400^{o}C under different temperatures. No THE was observed.

The domain wall energy with DMI is expressed as

$$\sigma_{\mathrm{DW}} = 4\sqrt{AK_{\mathrm{u}}} - \pi D \qquad \textbf{(6.2)}$$

where D is the effective DMI constant, A is the exchange constant, and K_{u} is anisotropy constant. When σ_{DW} comes to zero, skyrmions can emerge. The critical DMI energy constant can be estimated as

$$D_{\mathrm{c}} = 4\sqrt{AK} / \pi \qquad \textbf{(6.3)}$$

The exchange constant A is calculated from [17]

$$A = (a^2 T_{\mathrm{C}} \times M_s) / (2\,\mathrm{g} \times \mu_{\mathrm{B}}) \qquad \textbf{(6.4)}$$

where T_{C}, $\mathrm{M_s}$, g and μ_{B} is Curie temperature, saturation magnetization, Landé factor and Bohr magneton constant, respectively. Figures 6.7(a-h) show both the out-of-plane and in-plane magnetization of the reference MnGa(5) single layer annealed at 400°C (Fig. 6.6(a-b)), the BiSb(10)/MnGa(5-10) bilayers annealed at 400°C (sample B and sample D) (Fig. 6.6(c-d) and Fig. 6.6(g-h), respectively) and the MnGa(10)/BiSb(10) bilayer without the annealing step (sample C) (Fig. 6.6(e-f)). For annealed samples, the exchange constant A and anisotropy constant K_{u} are estimated to be about 5.4 pJ/m and 1.2×10^5 J/m^3, respectively, and the critical DMI constant D_{c} is 1 mJ/m^2.

Table 6.1 summarizes the THE, the exchange constant A, the anisotropy constant K_{u}, and the critical DMI energy constant D_{c} for the reference MnGa(5) and the sample B-D. By comparing sample B with sample C, one can see that the critical DMI energy constant was reduced over 2 times by the annealing step. For the sample D with thicker MnGa(10) thin film grown at the same condition, D_{c} ~ 7.0 mJ/m^2 which is nearly 7 times higher than that of sample B due to much larger M_{s}, and THE cannot be detected.

In multilayers, a critical interfacial DMI parameter D_{s} can be expressed as [13]

$$D_{\mathrm{s}} = D_{\mathrm{c}} \times t_{\mathrm{MnGa}} \tag{6.5}$$

The interfacial DMI constant is estimated D_s = 5.1 pJ/m for the sample B. For the sample C, D_s = 12.1 pJ/m (D_c = 2.43 mJ/m^2) which is two times larger than that of sample B. The vanishing of THE in sample C demonstrates the role of the annealing step on control of the critical DMI strength.

The domain wall width $\Delta = \sqrt{A/K}$ of sample B is estimated to be 5.4 nm and its fictitious magnetic field is estimated from

$$H_{\mathrm{eff}} = \rho_{\mathrm{T}} / (P \times R_0) \tag{6.6}$$

where P denotes the spin polarization of MnGa (P = 42%), and R_0 is the normal Hall coefficient ($R_0 = 0.6\times10^{-5}$ μΩcm/Oe). Hence, $H_{\mathrm{eff}} \sim 5.7$ kOe is estimated.

Table 6.2 compares D_c, and the critical interfacial DMI constant D_s of the sample B with previous works. A much larger D_s of 5.1 pJ/m was achieved in sample B. These results confirm that BiSb topological insulator is a promising candidate with large spin-orbit-torque [18] and huge interfacial DMI for generation and manipulation of skyrmion.

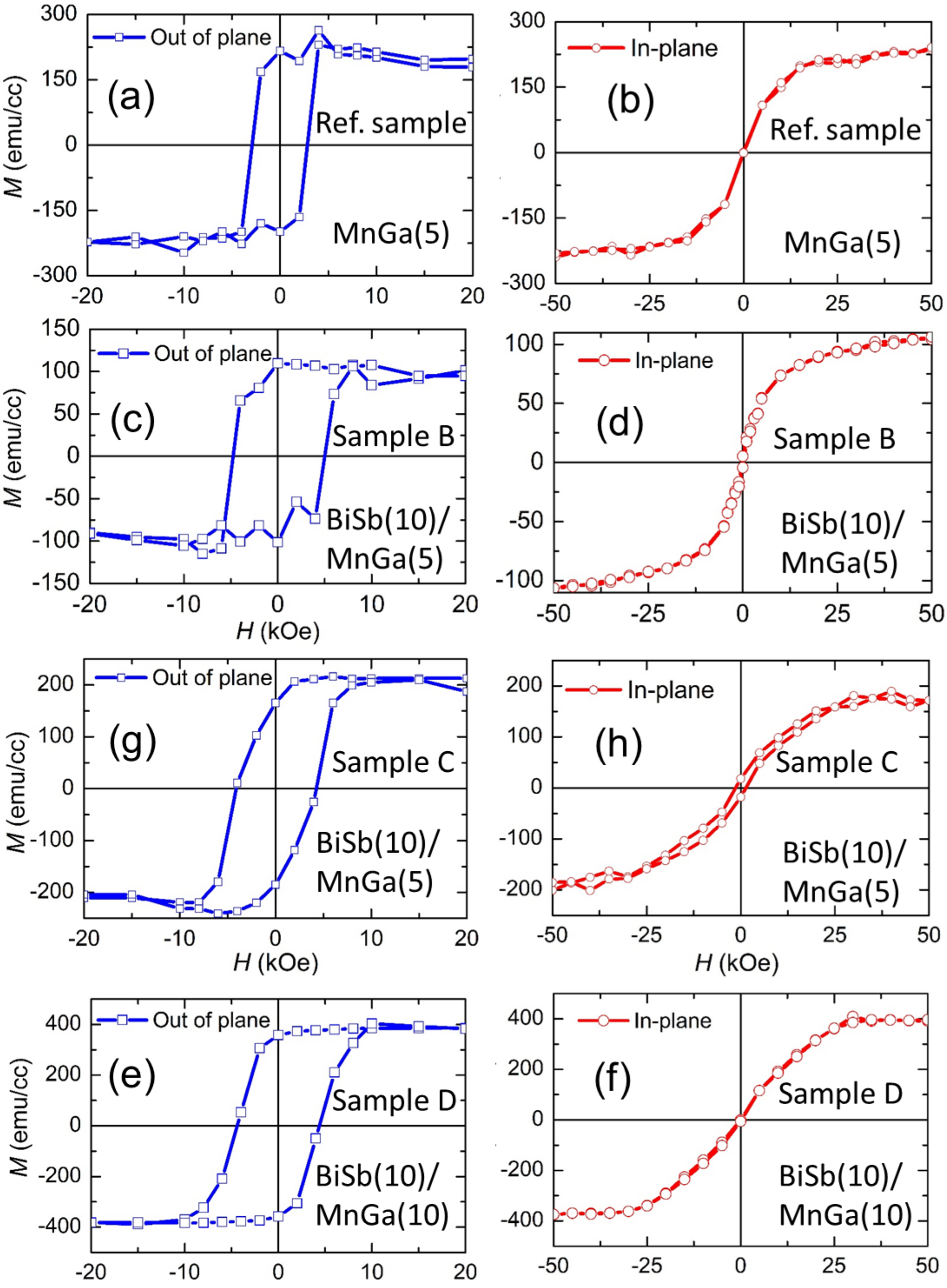

Figure 6.6: (a), (b) The out-of-plane and in-plane magnetization of a reference MnGa(5) single layer annealed at 400ºC. (c), (d) for sample B BiSb(10)/ MnGa(5) bilayers annealed at 400ºC. (e), (f) for sample C BiSb(10)/ MnGa(5) bilayers without annealing step. (g), (h) for sample D BiSb(10)/MnGa(10) bilayers annealed at 400ºC.

Table 6.1: The THE effect, the exchange constant A, the anisotropy constant K_u and the critical DMI energy constant D_c in the 400°C annealed reference MnGa(5) sample and sample B-D.

Sample	**Stack**	**Annealed**	**THE**	A **(pJ/m)**	K_u **(10^5 J/m^3)**	D_c **(mJ/m^2)**
Ref.	**MnGa(5)**	O	X	10.89	1.29	-
B	**BiSb(10)/MnGa(5)**	O	O	5.40	1.19	1.02
C	**BiSb(10)/MnGa(5)**	X	X	11.72	3.11	2.43
D	**BiSb(10)/MnGa(10)**	O	X	19.60	15.20	6.95

Table 6.2: Comparison of D_c and the critical interfacial DMI constant D_s observed in this work and other bilayers reported sofar.

	D_c **(mJ/m^2)**	D_s **(pJ/m)**
Co/Pt	1.30-2.05	1.37-2.17
CoFeB/Pt	1.0	0.8
MnGa/Pt or Ta	0.65-1.08	2.60-4.32
MnGa/BiSb (this work)	**1.02**	**5.1**

For the sample A, the critical DMI energy constant D_c of 1.08 mJ/m^2 is only slightly larger than that of sample B, and this cannot explain the difference in their potential landscape (Fig. 6.4 (a)). Here, I think that the surface roughness of the MnGa layer at different annealing temperatures plays an important role. Indeed, as shown in Fig. 6.7(a-c), the RHEED patterns are improved with annealing. To evaluate the surface roughness of MnGa, AFM was employed, and the measurement results are shown in Fig. 6.7(d-f). One can see that the root mean square value of the surface roughness R_q of MnGa was improved by annealing at higher temperatures.

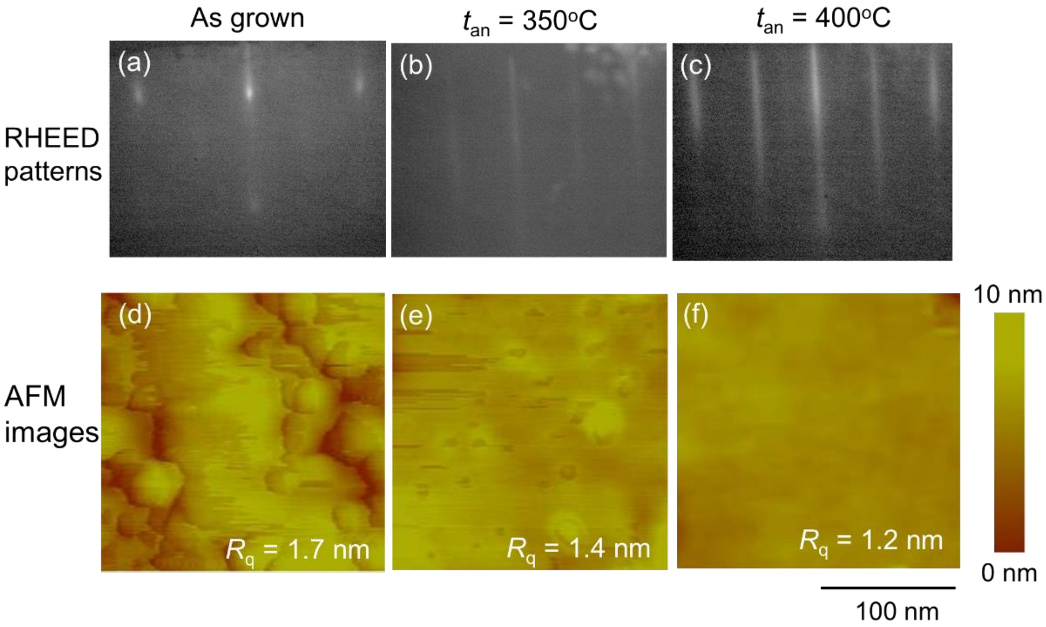

Figure 6.7: (a-c) RHEED patterns observed along the GaAs[$\bar{1}$10] direction of MnGa thin films for as grown and with annealing at 350°C and 400°C, respectively. (d-f) Surface of MnGa thin films measured by atomic force microscopy (AFM). The root mean square value of the surface roughness *R*q of each film is 1.7 nm, 1.4 nm and 1.2 nm, respectively.

6.3. Condition of DMI constant *D* and anisotropy constant K_u for generation of skyrmions

The existence of skyrmions is influenced not only by the DMI constant *D* but also by the anisotropy constant K_u as reported in previous work. Indeed, the typical value of K_u of MnGa thin film is estimated from 1.0×10^6 J/m^3 to 2.0×10^6 J/m^3[19, 20], but our samples only show THE for $K_u = 1.2\times10^5$ J/m^3. Therefore, in order to further understand the condition of K_u and *D* for generation of skyrmions, the finite difference time domain micromagnetic simulation by MuMax3 was employed [21]. The simulation follows steps proposed by M. Mruczkiewicz et al [22]. Bloch skyrmion is assumed in the initial state, and the final state is evaluated after relaxation to the ground state under zero magnetic field. The topological number is calculated as $S = \frac{1}{4\pi}\iint m\cdot\left(\frac{\partial m}{\partial x}\times\frac{\partial m}{\partial y}\right)dxdy$ [23]. The *S* value of uniform state, vortex state and skyrmion state are 0, 0.5, 1, respectively (see appendix B). The simulation parameters are the disk radius R = 64 nm, thickness t = 5 nm, saturation magnetization M_s = 108.6 emu/cc, exchange constant A = 5.4 pJ/m, damping factor α = 0.008, DMI constant D = 1.0 - 2.2 mJ/m^2 and magnetic anisotropy constant $K_u = 1.0\times10^5 - 5.0\times10^5$ J/m^3 which are similar to that of the 400^{o}C annealed samples. The results of simulation are showed in Fig. 6.9. The white squares present unconverged simulation, and the white line presents the D_c position where the THE was observed. One can see that the maximum K_u for generation of skyrmions is around 3.2×10^5 J/m^3. For K_u above this value, the disk changes to uniform state (S = 0). These results is consistent with my experiment results ($K_u = 1.2\times10^5$ J/m^3 for sample B) and interestingly, consistent with K. K. Meng et al [24] who show the largest value of K_u for observing THE in MnGa/heavy metal bilayers is approximately 3.0×10^5 J/m^3. Thus, my experimental results are consistent with the micromagnetic simulation results.

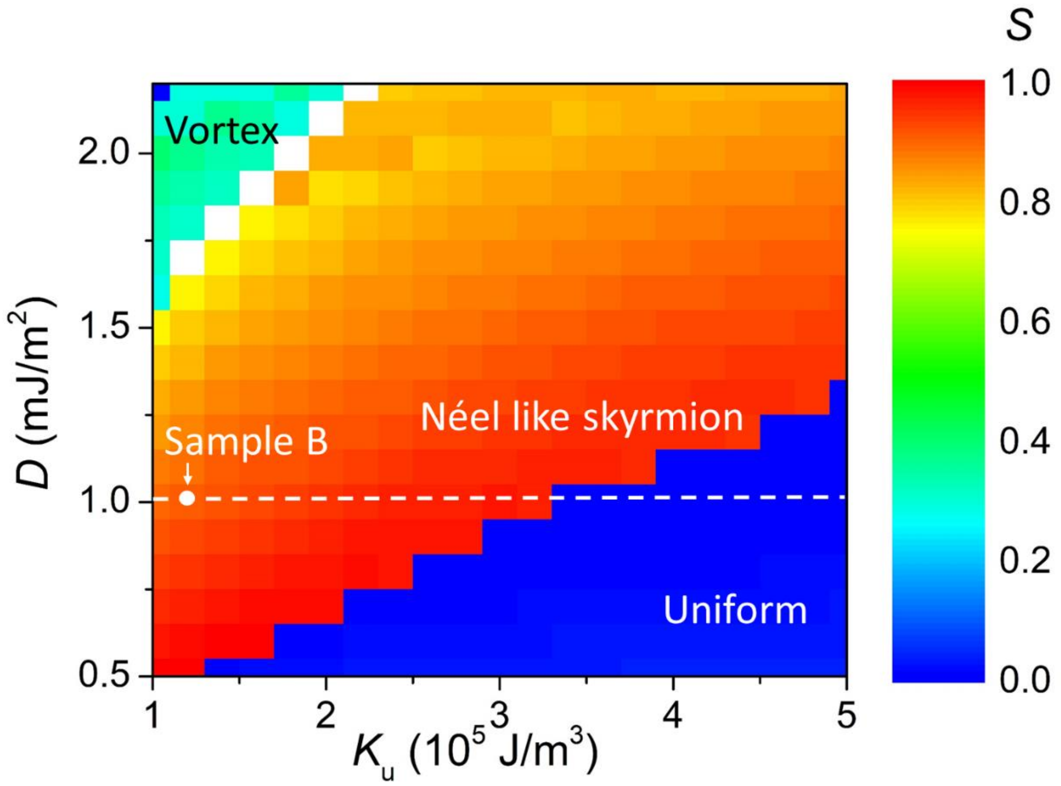

Figure 6.8: The skyrmion number S as a function of magnetic anisotropy constant K_u and DMI constant D. The white squares indicate unconverged simulator.

6.4. Summary

In this chapter, by combining the strong spin-orbit-interaction of BiSb and the small magnetization of MnGa, a large interfacial Dzyaloshinskii-Moriya-Interaction (DMI) (D_s = 5.1 pJ/m) was tailored by controlling the annealing temperature t_{an} of the MnGa template. Moreover, THE can be observed at room temperature even under absence of an external magnetic field, demonstrating field-free ground-state skyrmions. A large critical interfacial DMI constant of 5.1 pJ/m was obtained. These results confirm that BiSb topological insulator can generate not only colossal spin-orbit-torque, but also huge interfacial DMI for generation and manipulation of skyrmions.

References

1. G. Chen, A. Mascaraed, A. T. N'Diaye, and A. K. Schmid, Appl. Phys. Lett. **106**, 242404 (2015).

2. O. Boulle, J. Vogel, H. Yang, S. Pizzini, D. de Souza Chaves, A. Locatelli, T.O. Mentes, A. Sala, L. D. B. Prejbeanu, O. Klein, M. Belmeguenai, Y. Roussigne, A. Stashkevich, S.M. Cherif, L. Aballe, M. Foerster, M. Chshiev, S. Auffret, I.M. Miron, and G. Gaudin, Nat. Nanotechnol. **11**, 449 (2016).

3. F. Jonietz, S. Mühlbauer, C. Pfleiderer, A. Neubauer, W. Münzer, A. Bauer, T. Adams, R. Georgii, P. Böni, R. A. Duine, K. Everschor, M. Garst, and A. Rosch, Science **17**, 1648 (2010).

4. P. Bruno, V. K. Dugaev, and M. Taillefumier, Phys. Rev. Lett. **93**, 096806 (2004).

5. A. Neubauer, C. Pfleiderer, B. Binz, A. Rosch, R. Ritz, P. G. Niklowitz, and P. Böni, Phys. Rev. Lett. **102**, 186602 (2009).

6. N. Kanazawa, Y. Onose, T. Arima, D. Okuyama, K. Ohoyama, S. Wakimoto, K. Kakurai, S. Ishiwata, and Y. Tokura, Phys. Rev. Lett. **106**, 156603 (2011).

7. T. Yokouchi, N. Kanazawa, A. Tsukazaki, Y. Kozuka, M. Kawasaki, M. Ichikawa, F. Kagawa, and Y. Tokura, Phys. Rev. B **89**, 064416 (2014).

8. D. Liang, J. P. DeGrave, M. J. Stolt, Y. Tokura, and S. Jin, Nat. Comm. **6**, 8217 (2015).

9. J. Matsuno, N. Ogawa, K. Yasuda, F. Kagawa, W. Koshibae, N. Nagasa, Y. Tokura, and M. Kawasaki, Sci. Adv. **2**, e1600304 (2016).

10. S. Woo, K. Litzius, B. Krüger, M. Y. Im, L. Caretta, K. Richter, M. Mann, A. Krone, R. M. Reeve, M. Weigand, P. Agrawal, I. Lemesh, M. A. Mawass, P. Fischer, M. Kläui, and G. S. Beach, Nat. Mater. **15**, 501 (2016).

11. C. M. Luchaire, C. Moutafis, N. Reyren, J. Sampaio, C. A. F. Vaz, N. Van Horne, K. Bouzehouane, K. Garcia, C. Deranlot, P. Warnicke, P. Wohlhüter, J.-M. George, M.

Weigand, J. Raabe, V. Cros, and A. Fert, Nat. Nanotech **11**, 444 (2016).

12. H. T. Nembach, J. M. Shaw, M. Weiler, E. Jué, and T. J. Silva, Nat. Phys. **11**, 825 (2015).

13. O. Boulle, J. Vogel, H. Yang, S. Pizzini, D. S. Chaves, A. Locatelli, T. O. Mentes, A. Sala, L. D. Buda-Prejbeanu, O. Klein, M. Belmeguenai, Y. Roussigné, A. Stashkevich, S. M. Chérif, L. Aballe, M. Foerster, M. Chshiev, S. Auffret, I. M. Miron, and G. Gaudin, Nat. Nanotech **11**, 449 (2016).

14. K. Di, V. L. Zhang, H. S. Lim, S. C. Ng, M. H. Kuok, X. Qiu, and H. Yang, Appl. Phys. Lett. **106**, 052403 (2015).

15. S. Z. Lin, Phys. Rev. B **94**, 020402(R) (2016).

16. N. Romming, C. Hanneken. M. Menzel, J. E. Bickel, B. Wolter, K. V. Bergmann, A. Kubetzka, and R. Wiesendanger, Science **341**, 636 (2013).

17. M. Beg, R. Carey, W. Wang, D. C. Ortuno, M. Vousden, M. A. Bisotti, M. Albert, D. Chernyshenko, O. Hovorka, R. L. Stamps, H. Fangohr, Sci. Rep. **5**, 17137 (2015).

18. N. H. D. Khang, Y. Ueda, and P. N. Hai, Nat. Mater. **17**, 808 (2018).

19. Z. L. Jun, N. S. Hua, and Z. J. Hua, Chin. Phys. B **22**, 118505 (2013).

20. L. J. Zhu, D. Pan, S. H. Nie, J. Lu, and J. H. Zhao, Appl. Phys. Lett. **102**, 132403 (2013).

21. A. Vansteenkiste, J. Leliaert, M. Dvornik, M. Helsen, F. G. Sanchez, and B. V. Waeyenberge, AIP Adv. **4**, 107133 (2014).

22. M. Mruczkiewicz, M. Krawczyk, and K. Y. Guslienko, Phys. Rev. B **95**, 094414 (2017).

23. N. Nagaosa, and Y. Tokura, Nat. Nanotechnol. **8**, 899 (2013).

24. K. K. Meng, X. P. Zhao, P. F. Liu, Q. Liu, Y. Wu, Z. P. Li, J. K. Chen, J. Miao, X. G. Xu, J. H. Zhao, and Y. Jiang, Phys. Rev. B **97**, 060407(R) (2018).

Chapter 7

Unidirectional Magnetoresistance in GaMnAs - BiSb Bilayers

Besides the SHE and the THE, UMR is another attractive spin-related phenomenon, which can be used for determination of the magnetization direction of a single magnetic layer, making it possible to design novel SOT-MRAM with an extremely simple stacking structure and small foot print. Unfortunately, while UMR has been studied extensively in recent years as an attractive candidate for two-terminal magnetic memories and spin logic devices, improving its magnitude, which is still far below the practical value, and adequate understanding of the underlying microscopic origins are still required.

This chapter will study the UMR effect in a heterostructure of BiSb topological insulator – GaMnAs ferromagnetic semiconductor. I observed a large UMR ratio of 1.1% and found that this large UMR is not governed by the giant magnetoresistance (GMR)-like spin-dependent scattering, but by magnon emission/absorption and strong spin-disorder scattering in the GaMnAs layer. These results provide new insight into the complex physics of UMR, as well as a strategy for enhancing its magnitude for device applications.

7.1. Background

Figure 7.1(a) shows the schematic structure of a two-terminal planar MRAM device consisting of only a ferromagnetic layer and a spin Hall layer. For data writing, a bipolar pulse current is applied in plane for magnetization switching by the spin-orbit torque induced by SHE in the spin Hall layer. For data reading, a small bias current can be applied, and a sensing amplifier is used to determine the magnetization direction of the ferromagnetic layer by mean of the UMR effect. Such planar two-terminal memory devices are much simpler than the vertical magnetic tunnel junctions (MTJs) used in conventional MRAM, which involves over ten layers including a synthetic antiferromagnetic superlattice and a CoFeB layer for the reference layer, a MgO tunnel barrier, a CoFeB/Ta/CoFeB tri-layer for the free layer, a second MgO layer, and other supporting layers. Furthermore, there is a great degree of freedom in material choice for UMR-MRAM, since there is no restriction to the CoFeB/MgO/CoFeB combination as in the case of MTJs.

However, for the UMR effect to be used in such memory devices, its magnitude has to be at least a few % (earliest anisotropy magnetoresistance (AMR)-based MRAMs [1] have a typical AMR ratio of 2% for the Co permalloy as the magnetic layer). Previous studies of UMR in metallic bilayers, such as Ta or Pt/Co [2, 3] reports UMR ratios of about 0.005%, which are too small for practical applications. Recent interests have moved to topological insulator (TI)-based heterostructures, such as $Cr_x(Bi,Sb)_{2-x}Te_3/(Bi,Sb)_2Te_3$ [4] $(Bi,Sb)_2Te_3$/CoFeB and Bi_2Se_3/CoFeB [5]. Because of the large spin Hall angle in TIs [6, 7, 8, 9, 10], spin accumulation at the interface of those heterostructures can be enhanced, resulting in larger UMR ratios.

The physical origins of UMR are explained as combination of spin-dependent scattering (SS) and magnon scattering (MS) mechanisms at the interface or in the bulk of the ferromagnetic layer [11, 12]. Figure 7.1(b) illustrates the SS mechanism in a TI/FM heterostructure. The SHE or REE in the TI layer generates a pure spin current that is injected to the FM layer, resulting in spin accumulation near the surface. The transmission and reflection of spin at the interface depend on direction of the spin polarization σ and magnetization M, generating a GMR-like UMR signal. Furthermore, since the spin accumulation penetrates to bulk of the FM layer, the bulk spin-dependent scattering (denoted as bulk SS mechanism) of the FM layer also gives rise to a bulk UMR [13]. Note that this bulk UMR can have opposite polarity to the interfacial GMR-like UMR, depending on the mobility of majority/minority-spin electrons. Meanwhile, the MS mechanism involves magnon absorption or stimulated magnon emission in the FM layer when an accumulated spin flips its orientation (Fig. 7.1(c)). The change of the magnon temperature as the result of the MS process leads to the change of longitudinal resistance via the spin-disorder scattering of free carriers in the FM layer. All of these different mechanisms have recently been observed experimentally [11], but their magnitude varies with the material combination, and it is not clear how to optimize them to obtain a large enough UMR ratio for device applications. Recently, a large UMR ratio of 0.5% in $Cr_x(Bi,Sb)_{2-x}Te_3/(Bi,Sb)_2Te_3$ heterostructures was observed and explained as the manifestation of the enhanced asymmetric magnon scattering in the ferromagnetic TI $Cr_x(Bi,Sb)_{2-x}Te_3$ layer [4]. However, such asymmetric magnon scattering is limited to ferromagnetic TIs, whose Curie temperature is much lower than room temperature. Meanwhile, the GMR-like SS is the main mechanism in the $(Bi,Sb)_2Te_3$/CoFeB and Bi_2Se_3/CoFeB heterostructures [5], but the their UMR ratio is much smaller. Thus, a clear strategy for reaching over 1% of UMR ratio and a comprehensive understanding of the underlying microscopic mechanism of UMR in TI-based heterostructures are strongly required for device applications.

In this chapter, the UMR effect and their underling physical mechanisms will be investigated in GaMnAs ferromagnetic semiconductor / BiSb topological insulator heterostructures. Here, GaMnAs is a prototype ferromagnetic semiconductor with strong spin-disorder scattering [14], and BiSb is a topological insulator with a giant spin Hall effect [9, 10]. By varying the conductivity of the BiSb layer, I can change the current distribution flowing in the GaMnAs layer and the BiSb layer, and selectively study the mechanism of UMR in each case. The experiment results confirm that the MS mechanism is dominant in the GaMnAs layer with a maximum UMR of 1.1%, breaking the 1% barrier for the first time. The bulk SS mechanism in the GaMnAs layer is also observed with the corresponding maximum UMR of –0.009%. In addition, I found that other factors, such as the anomalous Nernst effect (ANE) of the GaMnAs layer and the ordinary Nernst effect (ONE) of the BiSb layer, can dominate the UMR-like signals, when the pure spin current injection from the BiSb to the GaMnAs layer is suppressed by the conductivity mismatch. These results provide a strategy to maximize the UMR ratio for practical device applications.

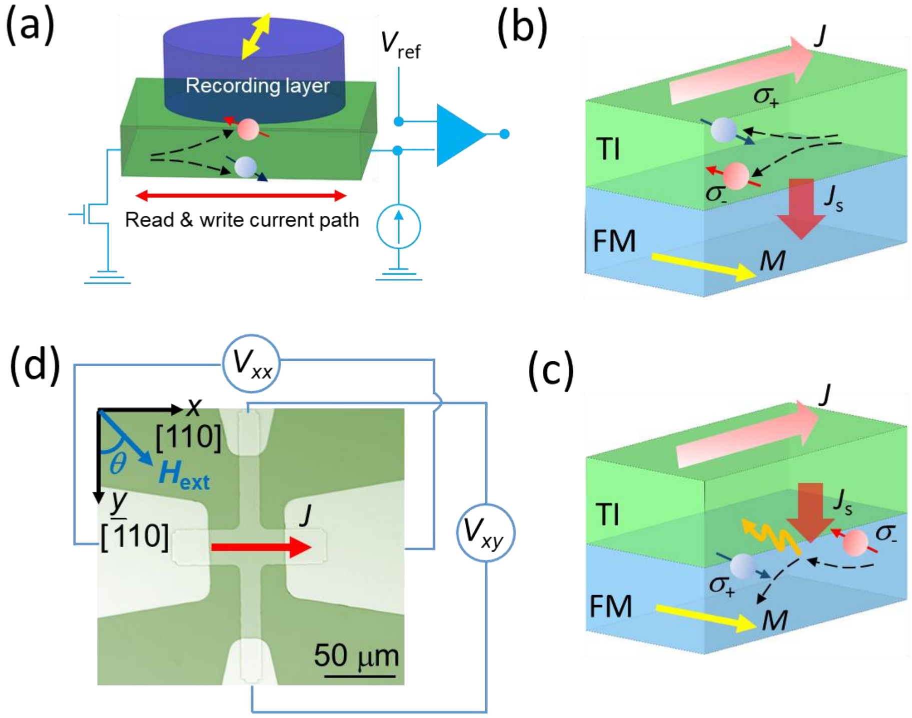

Figure 7.1: (a) Two-terminal planar MRAM device with an extremely simple stacking structure, consisting of only a ferromagnetic layer and a spin Hall layer. Spin-orbit torque and unidirectional magnetoresistance are utilized for data writing and reading, respectively. (b-c) Schematic illustration of the spin-dependent scattering (SS) and magnon scattering (MS) mechanism of UMR, respectively. (d) Optical image of a $Ga_{0.91}Mn_{0.09}As$ (10 nm) / $Bi_{0.9}Sb_{0.1}$ (10 nm) Hall bar and magnetoresistance measurement configuration.

7.2. Preparation of GaMnAs - BiSb bilayers

The 10 nm-thick $Ga_{0.91}Mn_{0.09}As$ (bottom) / 10 nm-thick $Bi_{0.85}Sb_{0.15}$ (top) heterostructures were grown on insulating GaAs(001) substrates by MBE. After removal of the surface oxide layer of GaAs substrate, a 20 nm-thick GaAs buffer was grown to obtain an atomically smooth surface at 580°C. Then, a 10 nm-thick $Ga_{0.91}Mn_{0.09}As$ layer was grown on the GaAs substrate at 300°C at the rate of 9 nm/min. The BiSb growth rate is 3.5 nm/min for both two samples. Finally, these samples were cooled down to the room temperature for deposition of an As thin cap layer. The growth process was monitored *in situ* by reflection high electron diffraction.

The samples were patterned into 100 μm × 25 μm Hall bars by optical lithography and Ar ion milling. A 60 nm-thick Au and a 6 nm-thick Cr adhesion layer were deposited as electrodes by electron beam evaporation, which reduce the effective length of the Hall bars to 50 μm. Figure 7.1(d) shows a photograph of a Hall bar with contact electrodes and the measurement configuration. UMR hysteresis curves were measured by sweeping an in-plane magnetic field H along the GaAs$[\bar{1}10]$ direction (the y direction) under various current density J. To extract the UMR hysteresis and eliminate the large even-function component of the conventional magnetoresistance $R_{xx}(H)$ of GaMnAs, the odd-function component ΔR_{xx} and UMR ratio were measured as follows

$$\Delta R_{xx} = R_{xy}(J) - R_{xy}(-J) \quad \textbf{(7.1)}$$

$$\text{UMR ratio} = \Delta R_{xx}^{\text{extr}} / R_{xx}(0) \quad \textbf{(7.2)}$$

where $\Delta R_{xx}^{\text{extr}}$ and $R_{xx}(0)$ are the extremum of $\Delta R_{xx}(H \geq 0)$ and the Hall bar resistance at zero magnetic field, respectively. In addition, to evaluate the contribution of the ANE and the ONE in the UMR signal, ΔR_{xx} and the odd-function component ΔR_{xy} of the planar

Hall resistance R_{xy} were measured under a rotating in-plane magnetic field. Here, ΔR_{xy} is expressed as

$$\Delta R_{\mathrm{xy}} = R_{xy}(J) - R_{xy}(-J) \tag{7.3}$$

In order to change the current distribution in the heterostructures, I fabricated two samples whose top BiSb layer has different crystal quality and electrical conductivity while the $Ga_{0.91}Mn_{0.09}As$ layer is kept the same. The first sample (denoted as sample A) has a poly-crystalline BiSb layer with low electrical conductivity ($\sigma \sim 1.5 \times 10^4\ \Omega^{-1}\mathrm{m}^{-1}$), which is similar to that of GaMnAs [15]. Thus, roughly half of the bias current flows in each layer of the sample A. Meanwhile, the second sample (denoted as sample B) has a (001)-oriented BiSb layer [16] with much higher conductivity ($\sigma \sim 2 \times 10^5\ \Omega^{-1}\mathrm{m}^{-1}$) [17], so that most of the bias current flows in the BiSb layer, while less than 10% of the bias current flows in the GaMnAs. In order to change the BiSb thin film's crystal quality, the BiSb layer was grown at different substrate temperature: 200°C for the sample A and 150°C for the sample B. This allows us to study the mechanism of UMR in each case independently. Figure 7.2(a) and 7.2(b) show a cross-sectional transmission electron microscope image of sample A and B, respectively, which confirm the contrasting crystal quality of the BiSb layer between two samples. Figure 7.2(c) shows the temperature dependence of the resistance R of the Hall bar of sample A. The resistance – temperature characteristics of the sample A represents that of GaMnAs, with $\mathrm{d}R/\mathrm{d}T$ singularity at the Curie temperature ($T_{\mathrm{C}} \sim 85$ K) [18]. Below T_{C}, R rapidly decreases as the result of suppressed spin-disorder scattering in GaMnAs. Note the large difference between the maximum and the minimum value of R is as large as 26%. The resistance change of sample A is strongly governed the resistance change of the GaMnAs rather than by the BiSb layer. In contrast, the resistance – temperature characteristics of the Hall bar of sample B, shown in Fig. 7.2(d), represents that of BiSb, showing a plateau at low temperatures due to the dominant metallic conduction on the topological surface states of BiSb [17]. The clear difference between the *R*-*T* curves of the two samples is consistent with the different distribution of the bias current in the two samples.

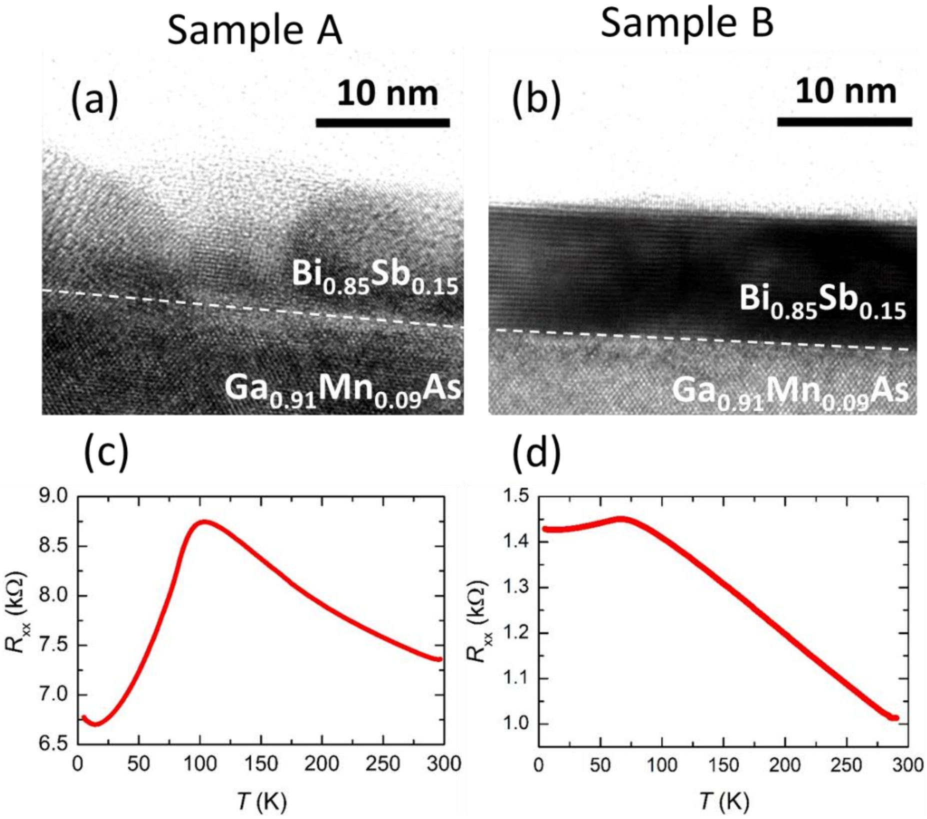

Figure 7.2: (a-b) Cross-sectional transmission electron microscope image of sample A and B, respectively. The top BiSb layer is polycrystalline with the electrical conductivity of about 1.5×10^4 $\Omega^{-1}m^{-1}$ in sample A, while it is (001)-oriented with the electrical conductivity of about 2×10^5 $\Omega^{-1}m^{-1}$in sample B. (a-b) Temperature dependence of the resistance *R* of a Hall bar of sample A and B, respectively.

7.3. UMR of sample A and its origin

Figure 7.3(a-h) show the UMR hysteresis curves $\Delta R_{xx} - H_{\mathrm{ext}}$ for the sample A at the base temperature T_{base} of 4 K and the current density $J = 0.2 \times 10^6$ A/cm^2 – 1.6×10^6 A/cm^2. The UMR is negative and has small magnitude (maximum -0.009%) at small $J \leq 6\times10^5$ A/cm^2. However, at higher $J \geq 8\times10^5$ A/cm^2, the UMR becomes positive and increases drastically, reaching 0.55% at $J = 1.6\times10^6$ A/cm^2. Such a switching of UMR polarity as a function of current density has not been observed before, indicating that there are several competing mechanisms of UMR. Considering that the spin Hall angle of BiSb has the same sign as that of Pt [9, 10], the negative UMR observed at small J means that the longitudinal resistance is larger when the spin polarization σ is parallel to M, and smaller when σ is antiparallel to M. This cannot be explained by the interfacial GMR-like SS and the MS mechanism, which should give an ordinary (positive) UMR effect. The only plausible mechanism of this phenomenon is the bulk SS mechanism, which can give rise to an inverse UMR when the mobility of the minority electrons is higher than that of majority electrons [13]. Such an inverse UMR effect was recently observed in $Co_{80}Cr_{20}$ / Pt bi-layers, where the $Co_{80}Cr_{20}$ is known to have higher mobility for minority electrons and the MS mechanism was suppressed by applying a strong external magmatic field [11]. In this case, the bulk SS mechanism in GaMnAs is dominant at low J and low T_{base}, when the MS mechanism is neglectable. At elevating J, the sample temperature increases due to Joule heating, and the MS mechanism began to take over, resulting in ordinary UMR.

To further see the competing action between the bulk SS mechanism and the MS mechanism, the UMR hysteresis at a higher T_{base} of 30 K was measured as shown in Fig. 7.4(a-h). One can see that the inverse UMR exists only at $J = 2\times10^5$ A/cm^2, and switches to the ordinary UMR at $J \geq 6\times10^5$ A/cm^2, agreeing with the stronger MS mechanism at higher temperature. Importantly, the UMR ratio reaches 1.1% at $J = 1.6\times10^6$ A/cm^2, breaking the 1% barrier for the first time. We concluded that the dominant mechanism in GaMnAs is MS with the corresponding UMR ratio at the order of 1%, while the bulk SS mechanism also exists but results in a much smaller UMR ratio at the order of -10^{-3}%.

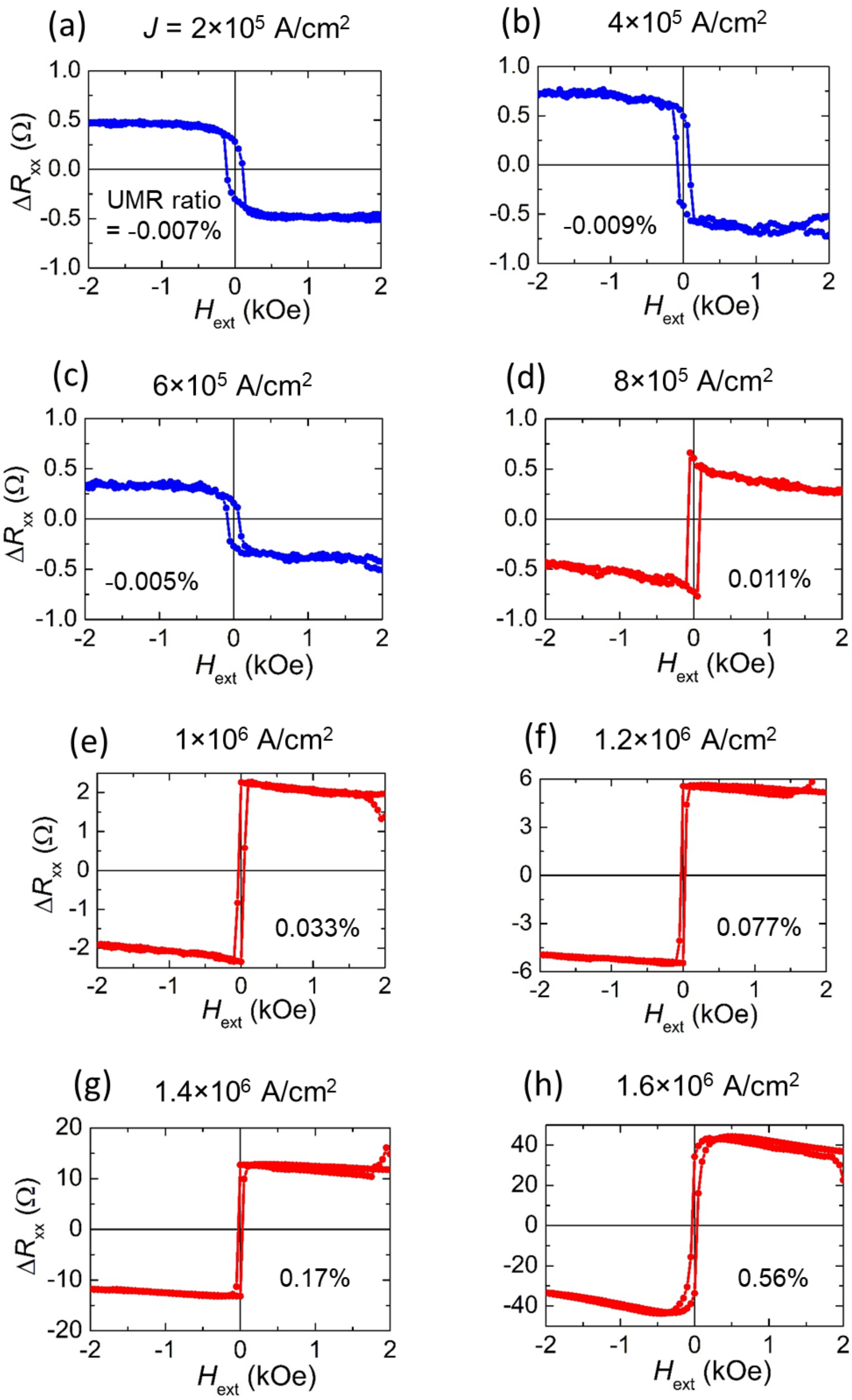

Figure 7.3: (a-h) UMR hysteresis curves ΔR_{xx} – H_{ext} for sample A at the base temperature T_{base} of 4 K and the current density $J = 0.2 \times 10^6$ A/cm^2 – 1.6×10^6 A/cm^2. The magnetic field was applied along the y direction. The inverse (negative) UMR at low J is governed by the bulk SS mechanism, while the ordinary (positive) UMR at high J is due to the MS mechanism.

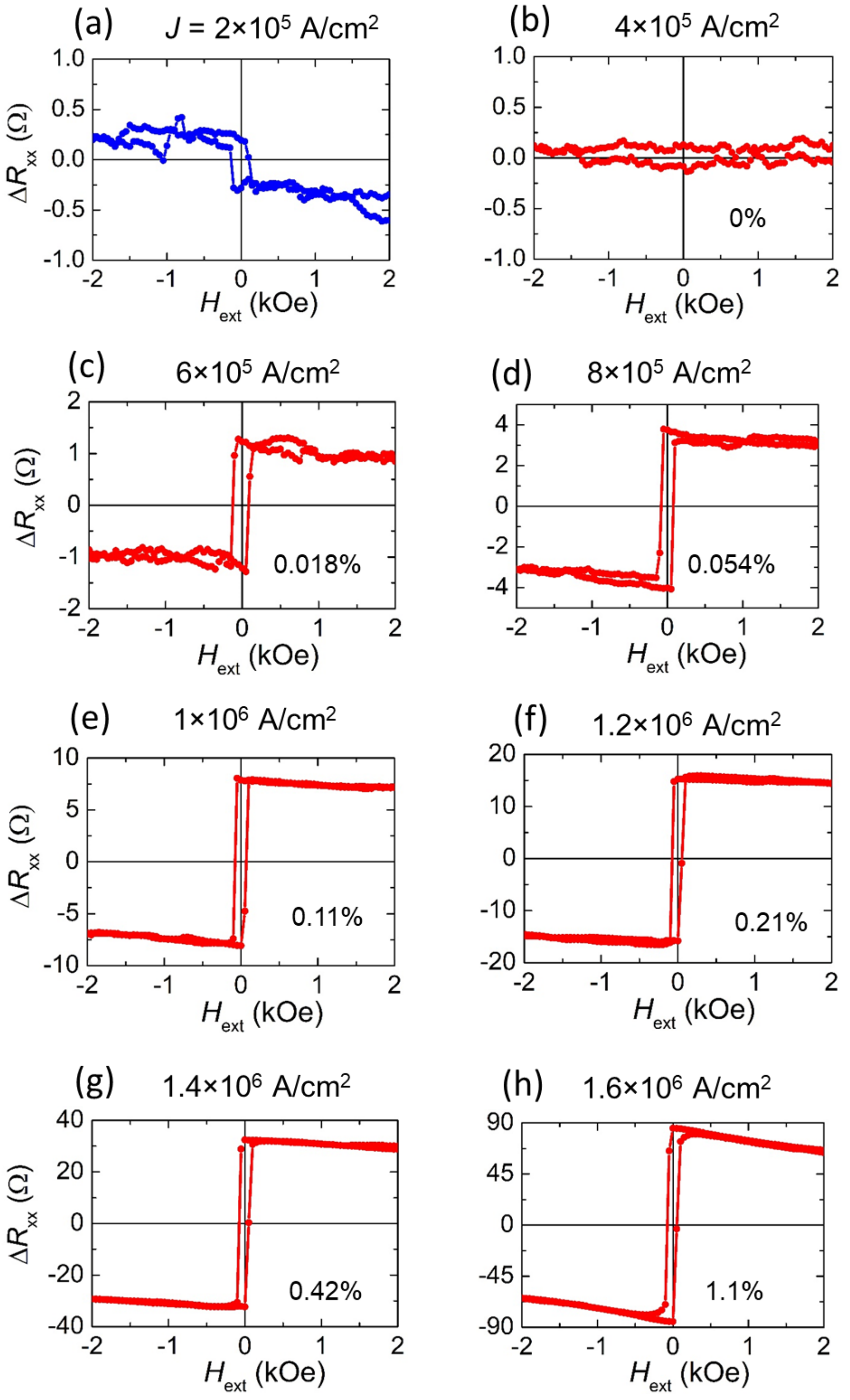

Figure 7.4: (a-h) The inverse UMR exists only at $J = 2\times10^5$ A/cm^2, and switches to the ordinary UMR at $J \geq 6\times10^5$ A/cm^2 due to stronger MS mechanism at higher temperature. The UMR ratio reaches 1.1% at $J = 1.6\times10^6$ A/cm^2, breaking the 1% barrier for the first time.

Figure 7.5(a) summarizes the UMR ratio as a function of J at various T_{base}. One can see that the UMR ratio rapidly increases with both J and T_{base}. Let the contribution of the bulk SS mechanism, the interfacial GMR-like SS mechanism, and the MS mechanism to the UMR ratio, to the UMR ratio as aJ ($a < 0$), bJ ($b > 0$), and $cJ + dJ^3$ ($c, d > 0$), respectively. The total UMR ratio can be fitted by $\alpha J + \beta J^3$, where $\alpha = a + b + c$ represents the linear contribution from the bulk SS minus that of the interfacial GMR-like SS and the MS mechanism, while $\beta = d$ represents the non-linear contribution of the MS mechanism at high J. The fitting shows reasonably good agreement with the experimental results, except for those at $T_{\mathrm{base}} = 50$ K and $J \geq 1.4 \times 10^6$ A/cm^2, where Joule heating makes the sample temperature close to the Curie temperature. Figure 7.5(b) shows the values of α, β at various T_{base}. α is negative and nearly unchanged for a wide range of temperature, indicating that the linear component of UMR is dominated by the bulk SS mechanism. Meanwhile, β gradually increases up to 50 K. Since UMR due to the MS mechanism depends on magnon absorption/emission, its magnitude is proportional to $(\mathrm{d}R/\mathrm{d}T)\Delta T_{\mathrm{m}}$, where $\Delta T_{\mathrm{m}} \sim J^3$ at high J is the magnon temperature difference between two magnetization directions. Thus, β is proportional to $\mathrm{d}R/\mathrm{d}T$. This observed β-T dependence is consistent with the increasing $\mathrm{d}R/\mathrm{d}T$ at elevated temperature near the Curie temperature of GaMnAs (Fig. 7.2(c)), reconfirming that the observed large UMR ratio at high J originates from the MS mechanism. The fact that UMR due to the MS mechanism increases with increasing temperature is quite attractive for device applications, because other well-known magnetoresistance effects, such as GMR [19, 20] or tunneling magnetoresistance (TMR) [21, 22] always decreases with increasing temperature. To further see the MS mechanism in action, Fig. 7.5(c) shows the UMR ratio at the very small J of 2×10^5 A/cm^2 as a function of T_{base}. At $T_{\mathrm{base}} \leq 30$ K, the UMR ratio is still negative since the bulk SS mechanism is dominant at this small current density and low temperatures. However, the UMR ratio becomes positive at $T_{\text{base}} \geq 40$ K, where the non-linear component of the MS mechanism become strong enough.

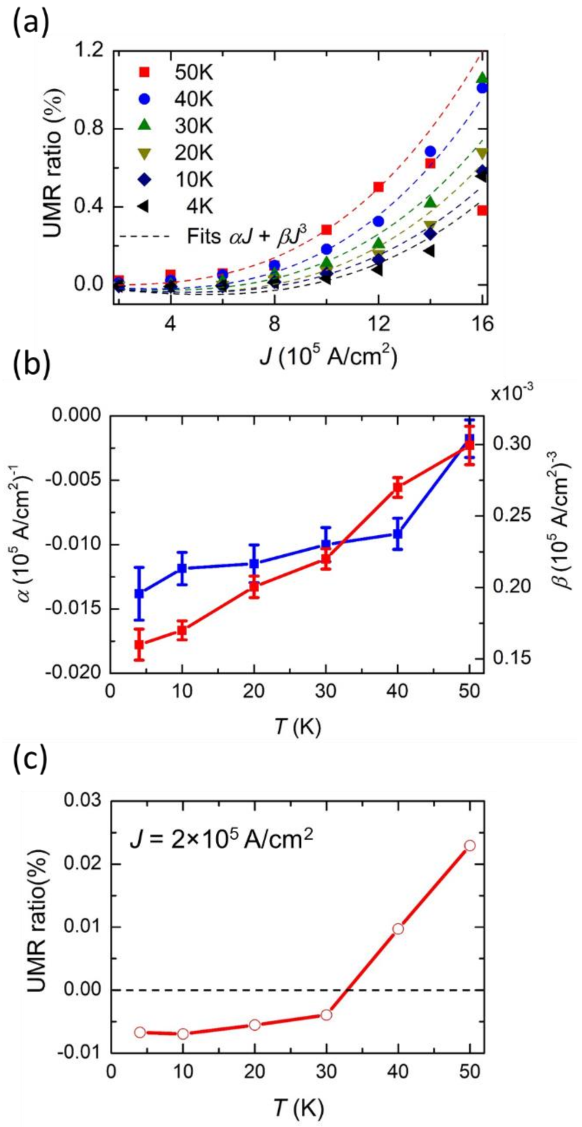

Figure 7.5: (a) UMR ratio as a function of J at various T_{base}. Dashed lines show the fitting curves by $\alpha J + \beta J^3$. (b) Values of α (blue) and β (red) at various T_{base}. α is negative and nearly unchanged for a wide range of temperature, indicating that the linear component of UMR is dominated by the bulk SS mechanism. Meanwhile, β gradually increases up to 50 K, consistent with the MS mechanism. (c) UMR ratio at the very small J of 2×10^5 A/cm^2 as a function of T_{base} in Fig. 5c, reflecting the competition between the bulk SS and MS mechanism.

There is another mechanism that can results in UMR-like behavior of ΔR_{xx}: the anomalous Nernst effect (ANE) of the GaMnAs layer with $V_{\mathrm{ANE}} \propto M\times\nabla T$, where ∇T is the temperature gradient in the GaMnAs layer. The corresponding thermal voltage is $V_{xx} \propto M_{\mathrm{y}}\nabla T_z$. However, the artifact ΔR_{xx} due to this thermal effect should be proportional to J (since $\nabla T_z \propto J^2$), thus it cannot be the origin of the observed J^3 dependence of UMR at high J. Nevertheless, contribution from the thermal effect was quantitatively evaluated by measuring ΔR_{xx} and ΔR_{xy} with an in-plane rotating magnetic field. Figure 7.6(a) and 7.6(b) show the magnetic field direction θ-dependence of ΔR_{xx}, measured at $T_{\mathrm{base}} = 4$ K, $J = 1.6\times10^6$ A/cm^2, and $H_{\mathrm{ext}} = 2$ kOe and 7.8 kOe, respectively. The amplitude of the ΔR_{xx} - θ curve (~ 20 Ω) at $H_{\mathrm{ext}} = 7.6$ kOe is smaller than that (~ 40 Ω) at $H_{\mathrm{ext}} = 2$ kOe due to suppression of magnon population under a higher magnetic field, as expected from the dominant MS mechanism. Figure 7.6(c-e) show the representative θ-dependence of ΔR_{xy}, measured at $H_{\mathrm{ext}} = 2$ kOe, 4 kOe, and 7.8 kOe, respectively. The experimental ΔR_{xy}-θ curves can be decomposed to the field-like torque's contribution (green curves), which is written as

$$R_{\mathrm{FL}} = R_{\mathrm{PHE}}\times(H_{\mathrm{FL}}/H_{\mathrm{ext}})\times(\sin 3\theta - \sin\theta) \qquad \textbf{(7.4)}$$

where R_{PHE} is the planar Hall resistance and H_{FL} is the field-like effective field, and the antidamping-like torque and thermal effects' contribution (blue curves), which is expressed as

$$R_{\mathrm{AD}} + R_{\nabla T} = (c_{\mathrm{AD}}/(H_{\mathrm{ext}} + H_{\mathrm{dem}}) + c_{\mathrm{AN}} + c_{\mathrm{ON}}\times H_{\mathrm{ext}})\sin\theta \qquad \textbf{(7.5)}$$

where c_{AD}, c_{AN} and c_{ON} are the coefficient of antidamping-like torque, the ANE of the GaMnAs layer, the ONE of the BiSb layer, respectively, and H_{dem} is the demagnetization field. By fitting to the experimental ΔR_{xy}-θ curves, $R_{\mathrm{AD}} + R_{\nabla T}$ can be extracted. Figure

7.6(f) shows its amplitude as a function of H_{ext}, which yields $c_{\mathrm{AN}} = 0.46\ \Omega$ and $c_{\mathrm{ON}} = 0.02\ \Omega\cdot\mathrm{kOe}^{-1}$, respectively. Thus, ANE is the main thermal effect, and its contribution to ΔR_{xx} is 0.92 Ω at $J = 1.6\times10^{6}\ \mathrm{A/cm}^{2}$, estimated from the Hall bar's size. The UMR ratio due to the ANE effect in sample A is about 0.02% at $T_{\mathrm{base}} = 4$ K and $J = 1.6\times10^{6}\ \mathrm{A/cm}^{2}$, which is much smaller than the observed UMR ratio of 0.56%, and even smaller than the estimated -0.056% from the bulk-SS mechanism. Therefore, while there are thermal effects contribution to UMR, its magnitude is neglectable in sample A.

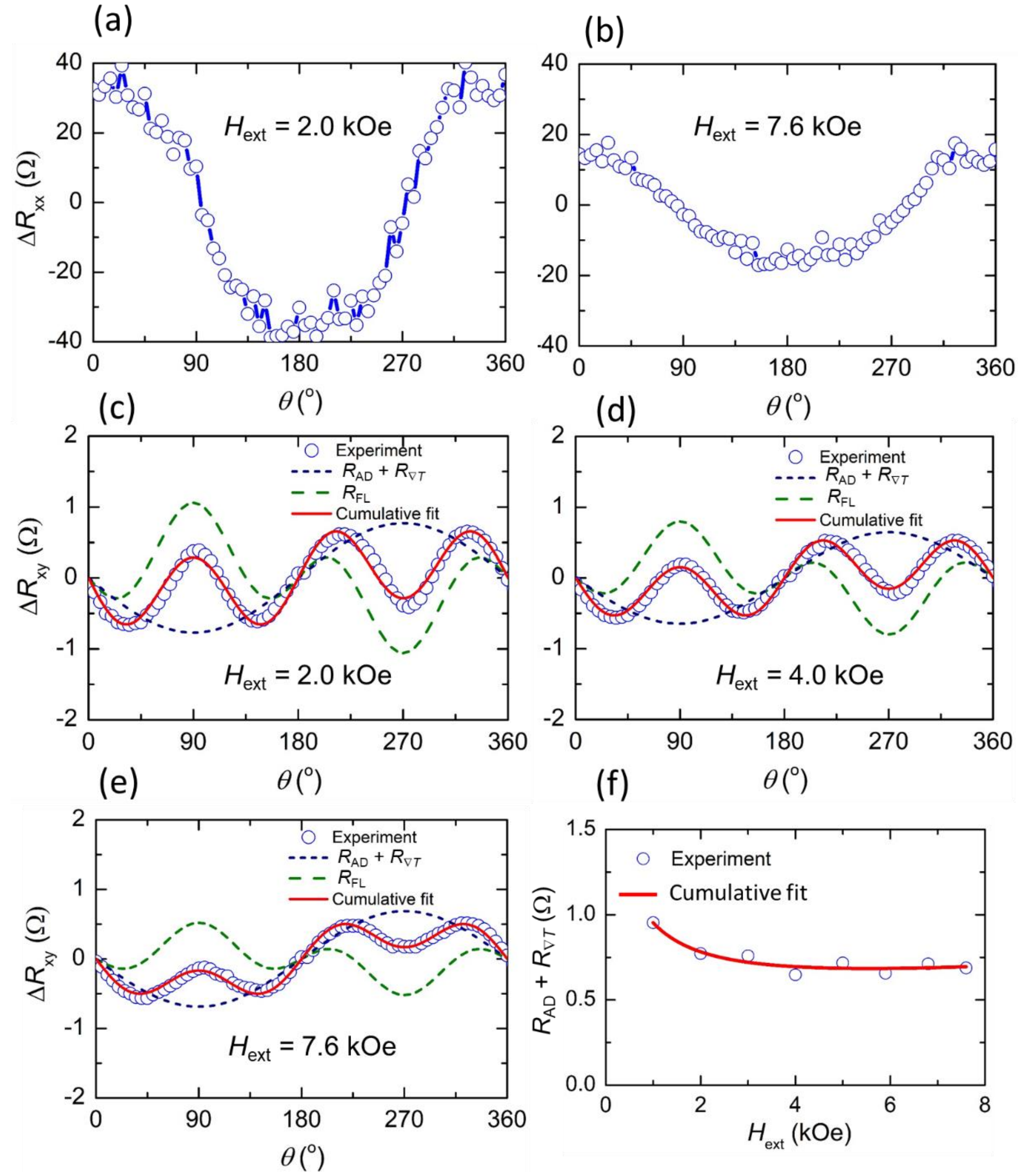

Figure 7.6: (a-b) Magnetic field direction θ–dependence of ΔR_{xx}, measured at T_{base} = 4 K, $J = 1.6 \times 10^6$ A/cm^2, and H_{ext} = 2 kOe and 7.6 kOe. respectively. (c-e) θ–dependence of ΔR_{xy} under H_{ext} = 2.0, 4.0, and 7.6 kOe, respectively. Blue circles: experimental data, green lines: contribution from the field-like torque R_{FL}, blue lines: contribution from the antidamping-like torque and thermal effects $R_{AD} + R_{\nabla T}$, red lines: cumulative fit curves. (f) $R_{AD} + R_{\nabla T}$ amplitude as a function of H_{ext}. Red line shows the fitting curve by $c_{AD}/(H_{ext} + H_{AD}) + c_{AN} + c_{ON} \times H_{ext}$.

7.4. UMR of sample B and its origin

In contrast to sample A where the conductivity of the BiSb and the GaMnAs layer is nearly the same, the conductivity of the BiSb is much higher than that of the GaMnAs layer in sample B. Such a situation is suitable to study the role of the conductivity matching in the UMR effect. Figure 7.7(a-h) show the UMR hysteresis curves $\Delta R_{xx} - H_{\text{ext}}$ of sample B at T_{base} = 4 K and $J = 0.2 \times 10^6$ A/cm^2 – 1.6×10^6 A/cm^2 for sample B. In this sample, most of the bias current flows in the BiSb layer, thus the bulk SS and MS mechanism in the GaMnAs are not detected. In contrast to sample A, the UMR ratio of sample B increases slowly, reaching a maximum UMR ratio of 0.020% at $J = 1.6 \times 10^6$ A/cm^2, which is an order of magnitude smaller than that of sample A measured at the same condition. In addition, contribution of the ONE can be observed through a linear dependence with a positive gradient of UMR on the external magnetic field H_{ext} at high J.

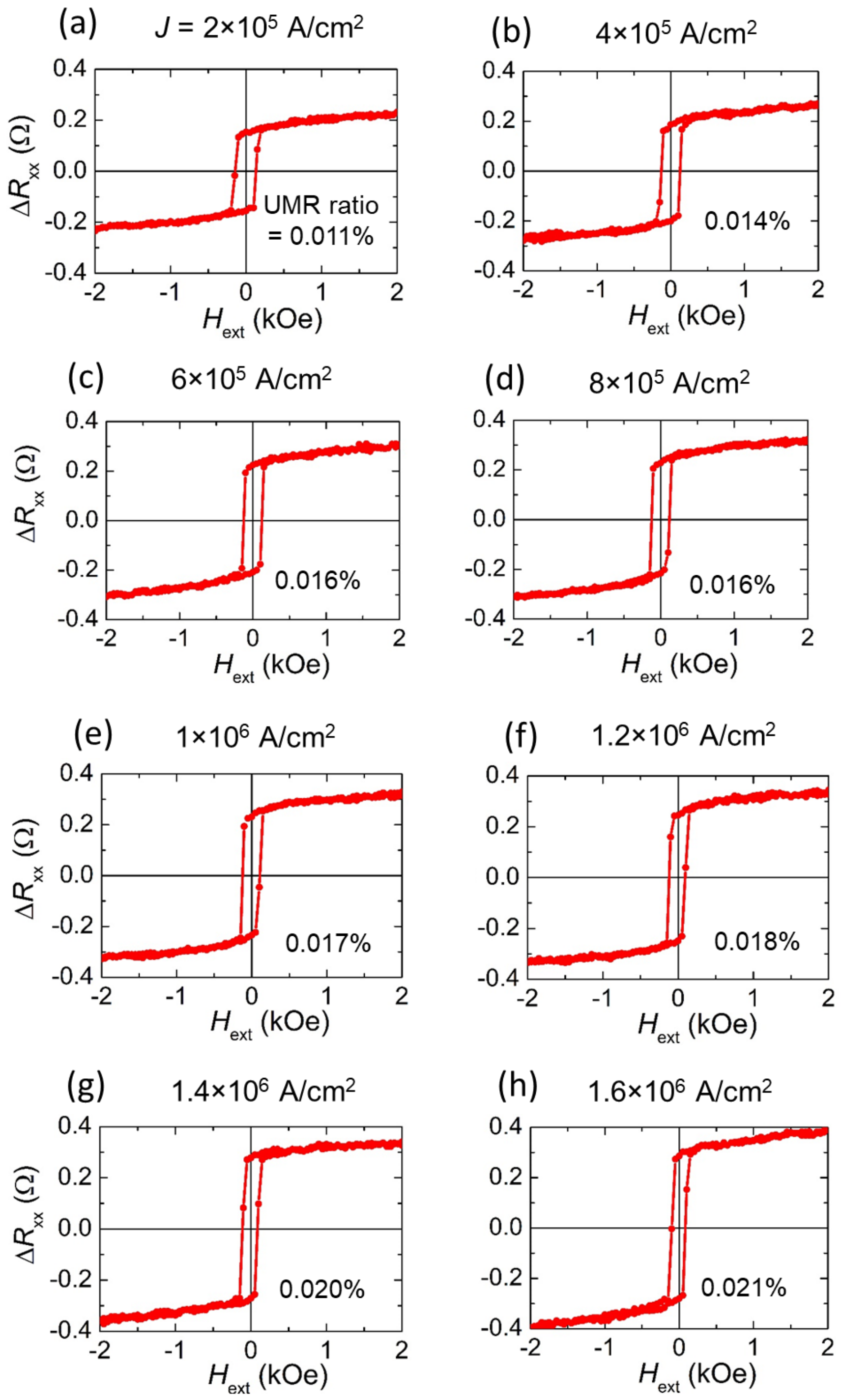

Figure 7.7: (a-h) UMR hysteresis curves $\Delta R_{xx} - H_{\mathrm{ext}}$ of sample B at T_{base} = 4 K and J = 0.2×10^6 A/cm^2 – 1.6×10^6 A/cm^2 for sample B.

Figure 7.8(a) summarizes the UMR ratio of sample B as a function of J at various T_{base}. The UMR ratio increases linearly with J at all temperatures, and its maximum value at $J = 1.6 \times 10^6$ A/cm^2 is nearly temperature-independent. At the first look, this behavior seems consistent with interfacial GMR-like SS mechanism. However, I found that this UMR-like signal in the sample B is completely governed by the thermal effects. Figure 7.8(b) shows the θ - dependence of ΔR_{xy} for sample B at $J = 1 \times 10^5$ A/cm^2 with H_{ext} = 1.0 and 7.6 kOe. One can see that ΔR_{xy} is dominated by the $(R_{\mathrm{AD}} + R_{\nabla \mathrm{T}})\sin\theta$ component that increases with increasing of H_{ext}, while the field-like torque R_{FL} component is absent. Figure 7.8(c) shows the extracted $R_{\mathrm{AD}} + R_{\nabla \mathrm{T}}$ amplitude as a function of H_{ext} at $J = 1 \times 10^5$ and 2×10^5 A/cm^2, which show that the antidampling-like torque $R_{\mathrm{AD}} = c_{\mathrm{AD}}/(H_{\mathrm{ext}} + H_{\mathrm{AD}})$ component is also absent, and the thermal component $R_{\nabla \mathrm{T}} = c_{\mathrm{AN}} + c_{\mathrm{ON}} \times H_{\mathrm{ext}}$ is dominant. At $J = 2 \times 10^5$ A/cm^2, $c_{\mathrm{AN}} = 0.075\ \Omega$ and $c_{\mathrm{ON}} = 0.016\ \Omega\cdot\mathrm{kOe}^{-1}$ were obtained. The corresponding contribution of ANE and ONE to ΔR_{xx} are 0.15 Ω and 0.032 $\Omega\cdot\mathrm{kOe}^{-1}$ at $J = 2 \times 10^5$ A/cm^2. Thus, the thermal effects perfectly describe the UMR hysteresis in Fig. 7.7(a), which means there is no UMR related to the GMR-like SS mechanism. This is consistent with the absence of the pure spin current injection from BiSb to the GaMnAs layer, as evidenced by the zero field-like torque and antidamping-like torque effects in the ΔR_{xy}–θ curves. The absence of pure spin current injection in sample B, despite better quality of the top BiSb layer, is the consequence of the well-known “conductivity mismatch” problem [23], which is known to prevent spin injection in bilayers with significantly different conductivity, such as metallic ferromagnet/semiconductor heterostructures. In the sample B, the conductivity of BiSb is much larger than that of GaMnAs, thus the spin injection efficiency is close to zero.

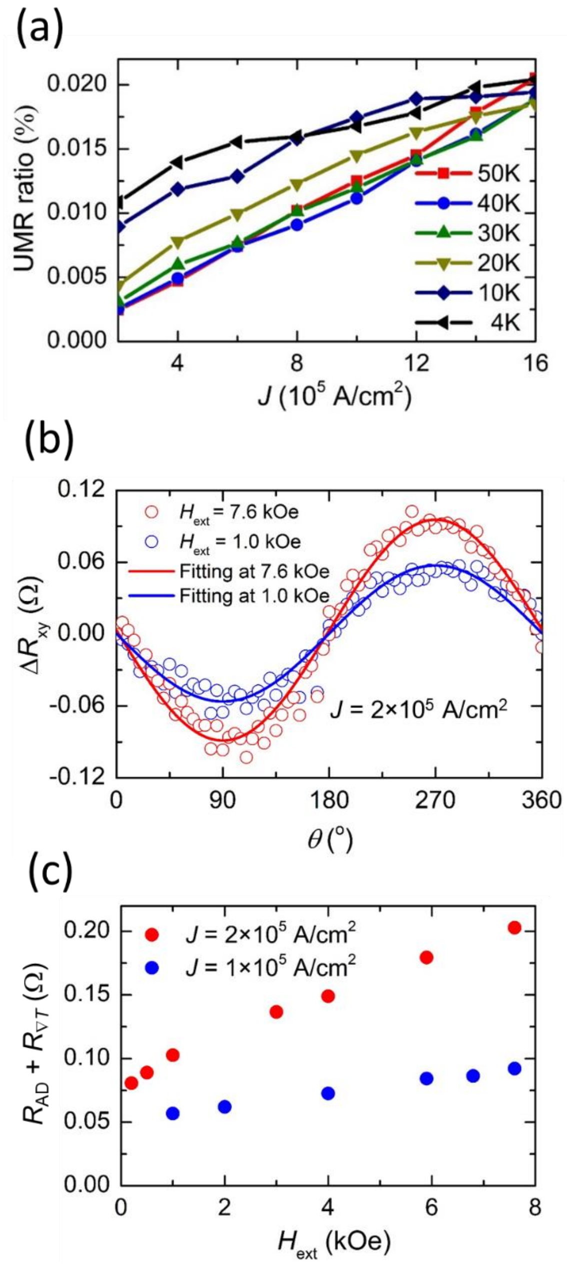

Figure 7.8: (a) UMR ratio of sample B as a function of J at various T_{base}. (b) θ–dependence of ΔR_{xy}, measured at $T_{\mathrm{base}} = 4$ K, $J = 2\times10^5$ A/cm^2, and $H_{\mathrm{ext}} = 1$ kOe (blue) and 7.6 kOe (red), respectively. Solid lines show the fitting curves by (R_{AD} + $R_{\nabla T}$). (c) $R_{\mathrm{AD}} + R_{\nabla T}$ amplitude as a function of H_{ext} at $J = 1\times10^5$ A/cm^2 (blue) and 2×10^5 A/cm^2(red).

7.5. Discussion

These results demonstrate that it is possible to obtain a UMR ratio larger than 1% in GaMnAs / poly crystalline BiSb heterostructures, which is larger than those in metallic bilayers and TI / metallic ferromagnet systems by several orders of magnitude. In particular, these results show that utilizing magnon scattering in ferromagnetic materials with strong spin disorder scattering and conductivity matching are the key factors to obtain a large UMR ratio for UMR-MRAM applications. Besides the required strong spin disorder scattering, the ferromagnetic material should have high enough resistivity to reduce the effect of parasitic resistance of electrical interconnection. Ferromagnetic semiconductors, like the GaMnAs material used in this work, are promising. Although the highest Curie temperature of GaMnAs thin film reported so far (~ 200 K) [24] is still lower than room temperature, several Fe-doped narrow-gap ferromagnetic semiconductors with room-temperature ferromagnetism, such as GaFeSb [25] or InFeSb [26, 27], have been realized recently.

On the other hand, topological insulators, such as Bi_2Se_3 [6], $(BiSb)_2Te_3$ [7], sputtered Bi_xSe_{1-x} [8], or poly-crystalline BiSb (this work), are promising as the spin Hall layer, since they have large spin Hall angle and comparable electrical conductivity with ferromagnetic semiconductors. In contrast to GMR or TMR effects for which material combinations have been exhaustedly explored, those for UMR are largely unexplored and open for development. Further material engineering may improve the UMR ratio to over 10%, which is essential for UMR-MRAM with extremely simple structure and fast writing/reading. My demonstration of an UMR ratio over 1% is an important step toward this goal.

7.6. Summary

This chapter presented the UMR effect in $Ga_{0.91}Mn_{0.09}As$ (10 nm)/$Bi_{0.85}Sb_{0.15}$ (10 nm) bilayers and clarified its origin. The large UMR ratio comes from the MS mechanism, while the SS mechanism plays a very small role. Moreover, the UMR ratios are several orders of magnitude larger than that in metallic bilayers and other TIs/FM systems. These results provide helpful insight into spin transport in strong spin-orbit-couple systems and can open the door to realistic applications such as two-terminal magnetic storage and spintronic devices based on UMR.

References

1. J. Daughton, T. Sol. Films **216**, 162 (1992).

2. C. O. Avci, K. Garello, J. Mendil, A. Ghosh, N. Blasakis, M. Gabureac, M. Trassin, M. Fiebig, and P. Gambardella, Appl. Phys. Lett. **107**, 192405 (2015).

3. C. O. Avci, K. Garello, A. Ghosh, M. Gabureac, S. F. Alvarado, and P. Gambardella, Nat. Phys. **11**, 570 (2015).

4. K. Yasuda, A. Tsukazaki, R. Yoshimi, K. S. Takahashi, M. Kawasaki, and Y. Tokura, Phys. Rev. Lett. **117**, 127202 (2016).

5. Lv. Yang, J. Kally, D. Zhang, J. S. Lee, M. Jamali, N. Samarth, and J. P. Wang, Nat. Commun. **9**, 111 (2018).

6. A. R. Mellnik, J. S. Lee, A. Richardella, J. L. Grab, P. J. Mintun, M. H. Fischer, A. Vaezi, A. Manchon, E. A. Kim, N. Samarth, and D. C. Ralph, Nature **511**, 449 (2014).

7. Y. Fan, P. Upadhyaya, X. Kou, M. Lang, S. Takei, Z. Wang, J. Tang, L. He, L. T. Chang, M. Montazeri, G. Yu, W. Jiang, T. Nie, R. N. Schwartz, Y. Tserkovnyak, and K. L. Wang, Nat. Mater. **13**, 699 (2014).

8. DC. Mahendra, R. Grassi, J. Y. Chen, M. Jamali, D. R. Hickey, D. Zhang, Z. Zhao, H. Li, P. Quarterman, L. Yang, M. Li, A. Manchon, K. A. Mkhoyan, T. Low, and J. P. Wang, Nat. Mater. **17**, 800 (2018).

9. N. H. D. Khang, Y. Ueda, P. N. Hai, Nat. Mat. **17**, 808 (2018).

10 . T. Shirokura, K. Yao, Y. Ueda, and P. N. Hai, preprint at https://arxiv.org/abs/1810.10840 (2018).

11. C. O. Avci, J. Mendil, G. S. D. Beach, and P. Gambardella, Phys. Rev. Lett. **121**, 087207 (2018).

12. I. V. Borisenko, V. E. Demidov, S. Urazhdin, A. B. Rinkevich, and S. O. Demokritov, Appl. Phys. Lett. **113**, 062403 (2018).

13. S. S. L. Zhang, and G. Vignale, Phys. Rev. B **94**, 140411 (2016).

14. F. Matsukura, H. Ohno, A. Shen, and Y. Sugawara, Physical Review B **57**, R2037 (1998).

15. K. W. Edmonds, K. Y. Wang, R. P. Campion, A. C. Neumann, N. R. S. Farley, B. L. Gallagher, and C. T. Foxon, Appl. Phys. Lett. **81**, 4991 (2002).

16. K. Yao, N. H. D. Khang, and P. N. Hai, J. Cryst. Growth **511**, 99 (2019).

17. Y. Ueda, N. H. D. Khang, K. Yao, and P. N. Hai, Appl. Phys. Lett. **110**, 062401 (2017).

18. V. Novák, K. Olejník, J. Wunderlich, M. Cukr, K. Výborný, A. W. Rushforth, K. W. Edmonds, R. P. Campion, B. L. Gallagher, Jairo Sinova, and T. Jungwirth, Phys. Rev. Lett. **101**, 077201 (2008).

19. M. N. Baibich, J. M. Broto, A. Fert, N. V. Dau, F. Petroff, P. Etienne, G. Creuzet, A. Friederich, and J. Chazelas, Phys. Rev. Lett. **61**, 2472 (1988).

20. G. Binasch, P. Grunberg, F. Saurenbach, and W. Zinn, Phys. Rev. B. **39**, 4828 (1989).

21. T. Miyazaki, and N. Tezuka, J. Magn. Magn. Mat. **139**, L231 (1995).

22. J. S. Moodera, L. R. Kinder, T. M. Wong, and R. Meservey, Phys. Rev. Lett. **74**, 3273 (1995).

23. G. Schmidt, D. Ferrand, L. W. Molenkamp, A. T. Filip, and B. J. van Wees, Phys. Rev. B **62**, R4790 (2000).

24. L. Chen, X. Yang, F. Yang, J. Zhao, J. Misuraca, P. Xiong, and S. von Molnár, Nano Lett. **11**, 2584 (2011).

25. N. T. Tu, P. N. Hai, L. D. Anh, and M. Tanaka, Appl. Phys. Lett. **108**, 192401 (2016).

26. A. V. Kudrin, Y. A. Danilov, V. P. Lesnikov, M. V. Dorokhin, O. V. Vikhrova1, D. A. Pavlov, Yu. V. Usov, I. N. Antonov, R. N. Kriukov, A. V. Alaferdov, and N. A. Sobolev, J. Appl. Phys. **122**, 183901 (2017).

27. N. T. Tu, P. N. Hai, L. D. Anh, and M. Tanaka, Appl. Phys. Exp. **11**, 063005 (2018).

Chapter 8

Conclusions and Future Perspectives

8.1. Conclusions

In this study, various spin-related phenomena in BiSb-ferromagnet bilayers were investigated for spintronic applications based on TIs. Here, the key results are highlighted as follows.

In chapter 1, the thesis background was introduced. The primary concepts of spin spintronics and its applications were reviewed. Spin-orbitronics was introduced as a novel concept that aims to utilize the spin-orbit interaction (SOI) in spintronic devices and has expanded spintronic materials to much broader spectra where spin devices utilize not only magnetic materials but also nonmagnetic materials with strong SOI. Toward exploring new materials with strong SOI, TIs and BiSb in particular appear as promising candidates. The motivation and outline of this thesis were introduced.

In chapter 2, fundamental physics of SOI was introduced. SOI-related effects, such as the Rashba-Edelstein effect, the SHE, THE, etc. were reviewed as new ideas that can help improve or even completely change spintronic device technologies. These ideas inspire my researches of spin-related phenomena in BiSb-ferromagnet bilayers as the main topic in the rest parts of thesis.

In chapter 3, the fabrication process of BiSb/FM bilayer thin films and characterization techniques were described in details. The thin film fabrication based on MBE and real-time monitoring by RHEED played the main role in fabrication process. For sample characterizations, different types of measurement, such as XRD measurement, magnetotransport measurement, magneto-optical measurement, magnetization measurement and AFM measurement were briefly introduced.

In chapter 4, growth of MnGa thin layer with high PMA on BiSb thin film despite their differences in the crystal symmetry and lattice constant were achieved. The high PMA in BiSb/MnGa bilayers was confirmed by MCD, AHE and SQUID measurements.

In chapter 5, the large spin Hall effect in BiSb thin film was investigated in various BiSb/MnGa bilayers. A huge spin-orbit field of 2.3 kOe/(MA/cm^2) was observed at room temperature. This value is much larger than those of heavy metals and other TIs by at least an order of magnitude. The estimated θ_{SH} of 52 is the largest value as reported so far. Comparing with other spin Hall material, BiSb shows the big advantage of large θ_{SH} and high electrical conductivity. In term of spin Hall conductivity $\sigma_{\mathrm{SH}} = (\hbar / 2e)\theta_{\mathrm{SH}} \times \sigma$ which considered as the figure merit for spin Hall materials, BiSb outperforms the nearest competitor (Pt) and other TIs by at least an order of magnitude. Finally, the ultra-low current density of 1.5 MA/cm^2 for SOT magnetization switching was demonstrated in BiSb/MnGa bilayers, even though the MnGa ferromagnet used in this work has higher PMA energy by an order of magnitude than those used in previous room-temperature SOT magnetization switching experiments.

In chapter 7, the THE in BiSb topological insulator / MnGa bilayers with an additional annealing step was observed and provided a firm evidence for the existence of skyrmions. By combining the strong spin-orbit-interaction of BiSb and the small magnetization of MnGa, a large critical interfacial Dzyaloshinskii-Moriya-Interaction (DMI) constant (D_{s} = 5.1 pJ/m) was achieved by controlling the annealing temperature of the MnGa template. Moreover, field-free ground-state skyrmions were observed for the first time at room temperature even under absence of an external magnetic field which is also consistent with micromagnetic simulations. These results confirm that BiSb topological insulator can generate not only large spin-orbit-torque, but also huge interfacial DMI for generation and manipulation of skyrmions.

In chapter 8, the large UMR in $Ga_{0.91}Mn_{0.09}As/Bi_{0.9}Sb_{0.1}$ bi-layers was reported. The observed UMR ratio is many orders of magnitude larger than those observed in metallic bi-layers and other TIs/CoFeB heterostructures. In addition, I found that the large UMR ratio comes from the MS mechanism, while the SD mechanism plays a very small role. These results provide helpful insight into spin transport in strong spin-orbit-couple systems and can open the door to realistic applications, such as two-terminal magnetic storage and spintronic devices based on UMR.

8.2. Future Perspectives

SOT-MRAM is the main application of BiSb studied in this thesis. Thanks to the high conductivity [1] and huge spin Hall angle [2], BiSb is the most promising pure spin current source for SOT-MRAM. From my results, the performance of BiSb-based SOT-MRAM in nano size of 37 nm was estimated and compared with commercial STT-MRAM at the same size (as shown in Fig. 8.1). The writing current can be reduced by at least an order of magnitude, while the writing speed in SOT-MRAM is 20 times faster than in STT-MRAM. The writing energy, therefore, can be reduced by at least two orders of magnitude. Moreover, the low writing current will help scale down the size of driving transistors which help increase the bit density of SOT-MRAM. This bench making demonstrates that BiSb-based SOT-MRAM outperforms STT-MRAM and can be very competitive with conventional volatile memory technologies.

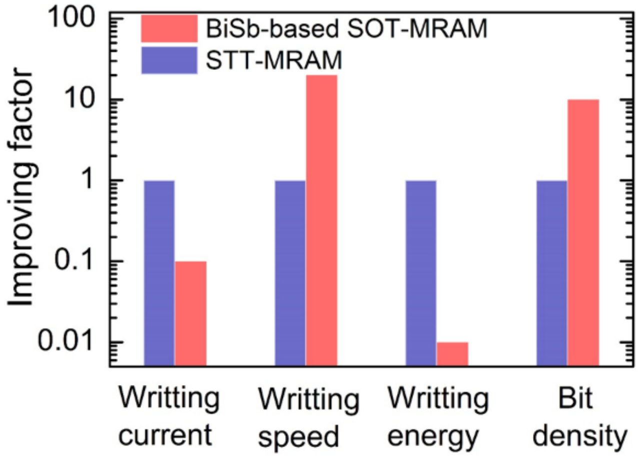

Figure 8.1: Benchmarking of SOT-MRAM based on BiSb as a spin source. The estimations are referenced with the performance of STT-MRAM with the same size (~ 37 nm).

Process integration of BiSb into a realistic MTJ stack remains the challenging problem for the realization of BiSb-based SOT-MRAM. In particular, because the

BiSb(012) surface is critical to obtain the very large spin Hall effect at room temperature, controlling of the surface orientation is a very important issue. However, the potential applications of BiSb(012) to realistic MRAM is very optimistic, because BiSb seems to grow with the BiSb(012) orientation on underlying ferromagnetic layers with a cubic crystal structure, and fortunately, most of the metallic layers used in MRAM has a cubic crystal structure, just like the MnGa layer in this work.

Furthermore, it is necessary to investigate whether the performance of BiSb(012) surface does not degrade when fabricated by the industry-friendly sputtering method, rather than by the MBE method as in this work. This can be quite challenging since there are big differences between the lab and industrial conditions. While thin film fabrication process in my studies was done by MBE to ensure the high quality of BiSb and ferromagnetic layers, conventional physical vapor deposition, such as sputtering will be employed for the industrial mass production, and its final step requires annealing of SOT-MRAM devices in 1 hour at 400^{o}C, which is higher than BiSb's melting temperature and can may modify its intrinsic transport properties. Therefore, the spin Hall angle θ_{SH} and electrical conductivity σ of BiSb layer can be changed and directly affect the writing energy of SOT-MRAM devices [3]. Fortunately, recent studies from our group show that BiSb survives such condition by using a capping layer. Second, the spin Hall angle of TI seems not to degrade when deposited using the sputtering method. Recently, θ_{SH} of a sputtered 4 nm-thick Bi_xSe_{1-x} layer was found to be about 18.8 [4], which is larger than θ_{SH} = 2~3 of the MBE-grown Bi_2Se_3 layer [5]. On the other hand, while MnGa thin film was used as the magnetic layer in my researches, industrial applications employ other materials, such as CoFeB or Co-based multilayers. Therefore, it is important to study the SHE effect in BiSb/CoFeB or BiSb/Co-based multilayers.

Race track memory based on skyrmions is another application of BiSb. Confirming the existence of skyrmions by the THE and demonstration of field-free ground state skyrmions are promising for skyrmion-driven racetrack memory [6, 7]. Future study will be direct observation of skyrmions and SOT-driven skyrmion motion.

Two terminal SOT-MRAM without a reference layer is another application of BiSb. The novel UMR-based MRAM is very promising since they require only two layers [8] and two terminals for both reading and writing. This unique advantage cannot be seen in conventional SOT-MRAM and other kinds of MRAM. Observation of the large UMR ratio up to 1.1% is a milestone toward realistic UMR-based MRAM. The next step will be realization of the large UMR ratio (> 1%) at room temperature by the magnon-scattering mechanism.

References

1. Y. Ueda, N. H. D. Khang, and P. N. Hai, Appl. Phys. Lett. **110**, 062401 (2017).
2. N. H. D. Khang, Y. Ueda, and P. N. Hai, Nat. Mater. **17**, 808 (2018).
3. C. F. Pai, Nature Materials **17**, 755 (2018).
4. DC. Mahendra, R. Grassi, J. Y. Chen, M. Jamali, D. R. Hickey, D. Zhang, Z. Zhao, H. Li, P. Quarterman, L. Yang, M. Li, A. Manchon, K. A. Mkhoyan, T. Low, and J. P. Wang, Nat. Mater. **17**, 800 (2018).
5. A. R. Mellnik, J. S. Lee, A. Richardella, J. L. Grab, P. J. Mintun, M. H. Fischer, A. Vaezi, A. Manchon, E.-A. Kim, N. Samarth, and D. C. Ralph, Nature **511**, 449 (2014).
6. S. Woo, K. Litzius, B. Krüger, M. Y. Im, L. Caretta, K. Richter, M. Mann, A. Krone, R. M. Reeve, M. Weigand, P. Agrawal, I. Lemesh, M. A. Mawass, P. Fischer, M. Kläui, and G. S. Beach, Nat. Mater. **15**, 501 (2016).
7. C. M. Luchaire, C. Moutafis, N. Reyren, J. Sampaio, C. A. F. Vaz, N. Van Horne, K. Bouzehouane, K. Garcia, C. Deranlot, P. Warnicke, P. Wohlhüter, J.-M. George, M. Weigand, J. Raabe, V. Cros, and A. Fert, Nat. Nanotech **11**, 444 (2016).
8. K. Olejník, V. Novák, J. Wunderlich, and T. Jungwirth, Phys. Rev. B **91**, 180402 (2015).

Appendix A

H_{so} obtained by fitting data in Figs. 5.8(a)-5.8(b) in the high in-plane field range (H > 4 kOe)

To further confirm the validity of the relationships $H_{\mathrm{so}} = \Delta H_{\mathrm{c}}$ used to estimate H_{so} from data in Fig. 5.7(a), fitting of the experimental R_{H}-H data in Figs. 5.8(a)-(b) was performed in the high in-plane magnetic field range ($|H|$ > 4 kOe). As dicussed before in chapter section 5.3.1, when an in-plane $|H|$ > 4 kOe is applied, all domains are oriented toward the magnetic field direction, and the whole sample becomes a single domain (macrospin). Therefore, it is possible to estimate H_{so} by fitting the R_{H}-H data at $|H|$ > 4 kOe to the single domain model. Note that the field-like spin-orbit field is negligible, thus the magnetization vector is in the x-z plane. Therefore, all torques acting on M are along the y direction. The torque balance equation for M becomes a simple scalar equation

$$T_{\mathrm{SO}} + T_{\mathrm{ani}} + T_{\mathrm{H}} = 0 \qquad \textbf{(A1)}$$

where $T_{\mathrm{so}} = H_{\mathrm{so}}M$ is the spin-orbit torque, $T_{\mathrm{H}} = -HM\cos\phi$ is the torque by the in-plane external field $H//x$, $T_{\mathrm{ani}} = \frac{\mathrm{d}E_{\mathrm{ani}}}{\mathrm{d}\phi} = K_{\mathrm{u}}\sin 2\phi - K_4 \sin 4\phi$ is the torque by anisotropy magnetic fields. Equation A1 can be rewritten as

$$H_{\mathrm{SO}} + \frac{1}{2}H_{\mathrm{u}}\sin 2\phi - \frac{1}{4}H_4\sin 4\phi - H\cos\phi = 0 \qquad \textbf{(A2)}$$

Note that Equation A2 is same as that derived in the pioneering work of L. Liu *et al.*, Phys. Rev. Lett., 109 (2012) 096602, for the Pt/Co bi-layer, except for the term $-\frac{1}{4}H_4\sin 4\phi$ from the bi-axial anisotropy field and the opposite direction of H_{so} (because BiSb is deposited on top of MnGa, unlike Liu's Pt/Co bi-layer where Pt is deposited under Co.)

Using Eq. A2, one can find H_{so} using a single data point of ϕ (deduce from R_H) and H, given that H_u and H_4 are known. However, we found that the values H_u = 10 kOe, H_4 = 30 kOe obtained for the as-grown BiSb/MnGa bi-layer do not give a unique H_{so} for different data points (R_H, H) of the Hall bar. This may be due to the fact that the BiSb/MnGa bi-layer underwent additional stress and annealing during the photolithography and ion-milling process for fabrication of the Hall bar, thus H_u and H_4 of the Hall bar may be different from that of the as-grown bi-layer. Indeed, the coercive force of the Hall bar at small current densities (1.6 kOe) is smaller than that (4.5 kOe) of the as-grown bi-layer. Here, H_u and H_4 are treated as adjustable parameters and estimate H_{so} using the following procedure.

First, Eq. A2 can be rewritten as

$$H_{\mathrm{SO}} = -\frac{1}{2} H_{\mathrm{u}} \sin 2\phi + \frac{1}{4} H_4 \sin 4\phi + H \cos\phi = \mathrm{const} \qquad \textbf{(A2)}$$

At a given current density, H_{so} is unique and should not change with ϕ or H. H_{so} is derived by the following algorithm.

(1) Assume a pair of H_u and H_4.

Calculate H_{so} from Eq. S5 using the experiment data in Fig. 2(c) or 2(d) at $|H| > 4$ kG.

(2) Fitting the calculated $|H_{so}|$ to a linear $a|H| + b$ function.

(3) Adjust H_4 so that $a < 0.001$ (i.e. nearly independent from H); thus, b gives the average $|H_{so}|$.

(4) Adjust H_u so that the average deviation of H_{so} for all data points δ = $\sqrt{\overline{(|H_{\mathrm{so}}| - b)^2}} / b$ becomes less than 5%.

H_u and H_4 are adjusted, and the (1)-(5) loop is repeated until $a < 0.001$ and $\delta < 5\%$. If these conditions cannot be satisfied, the calculation loop is stoped and the data is ignored.

The calculation was performed using data of the forward sweep (H: -8 kOe → + 8 kOe) and backward sweep (H: +8 kOe → -8 kOe) in Fig. 5.8(a) and 5.8(b). There are three sets of data that satisfied these conditions. Other data are too noisy and do not fit well. The fitting results are summarized in Table. A1 and shown in Figs. A1.

The obtained average $|H_{so}|$ are 2.9 – 3.4 kOe for $J = \pm 13.8 \times 10^5$ A/cm^2, which are within 10% of uncertainty from that obtained by assuming $H_{so} = \Delta H_c = 3.1$ kOe for $J = 13.8 \times 10^5$ A/cm^2 in Fig. 5.7(a).

Table A1. Fitting results for data in Figs. 5.8(a) and 5.8(b) to Eq. A3.

Data source		***a***	***b***	$\boldsymbol{\delta}$	**Ref.**
Fig. 2(c) J = 13.8×10^5 A/cm^2	Backward sweep $H < -4$ kOe	0.0009	2.9 kOe	4.7%	Fig. A1(a)
Fig. 2(d) J = -13.8×10^5 A/cm^2	Forward sweep $H < -4$ kOe	0.0004	3.4 kOe	4.9%	Fig. A1(b)
Fig. 2(d) J = -13.8×10^5 A/cm^2	Forward sweep $H > 4$ kOe	0.0001	3.4 kOe	4.8%	Fig. A1(c)

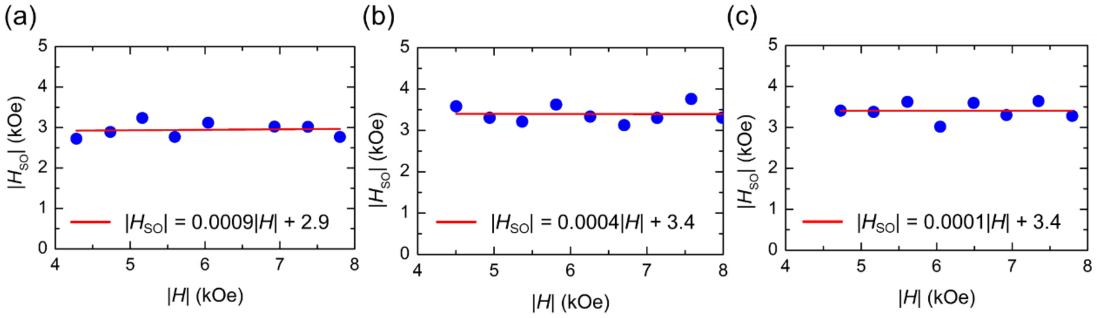

Figure A1: Fitting results using Eq. S5 for (a) data in Fig. 5.8(a) with J = 13.8×10^5 A/cm^2, backward sweep, $H < -4$ kOe, (b) data in Fig. 5.8(b) with J = -13.8×10^5 A/cm^2, forward sweep, $H < -4$ kOe, and (c) data in Fig. 5.8(b) with J = -13.8×10^5 A/cm^2, forward sweep, $H > 4$ kOe.

Appendix B

MuMax3 script for micro magnetic simulation

MuMax3 is an open-source and finite-element micromagnetic simulation software. MuMax3 is freely distributed under GPLv3 license on http://mumax.github.io. Representative magnetization configurations in my simulations are shown in Fig. B1. Results for K_u = 1.2×105 J/m3 and D = 1.0 mJ/m^2 are presented in Fig. B2. The MuMax3 code is shown as below.

```
setgridsize(128, 128, 1);          // set number of domains
setcellsize(1e-9, 1e-9, 5e-9);     // set domain size
SetGeom(Circle(1.28e-07));         // set a circular geometry

Msat  = 108.64e3;                  // saturation magnetization
Aex   = 5.4e-12;                   // exchange stiffness
alpha = 0.008;                     // Landau-Lifshitz damping constant of MnGa
AnisU = vector(0, 0, 1);           // uniaxial anisotropy in z direction
Dbulk = 0;                         // no bulk Dzyaloshinskii-Moriya strength
B_ext = vector(0, 0, 0);           // no external magnetic field

tableadd(Dind);
tableadd(Ku1);
tableadd(ext_topologicalcharge);
tableadd(LastErr);
tableadd(PeakErr);
```

```
Dind = 0.5e-3;                        //set Interfacial Dzyaloshinskii-Moriya strength
        for i:=1e5; i<=5e5; i+=0.2e5{
                Ku1 = i;
                m = BlochSkyrmion(1, 1);
                relax();
                save(m);
                tablesave();
        }
  Dind = 0.6e-3;
        for i:=1e5; i<=5e5; i+=0.2e5{
                Ku1 = i;
                m = BlochSkyrmion(1, 1);
                relax();
                save(m);
                tablesave();
        }
…
  Dind = 2.5e-3;
        for i:=1e5; i<=5e5; i+=0.2e5{
                Ku1 = i;
                m = BlochSkyrmion(1, 1);
                relax();
                save(m);
                tablesave();
        }
```

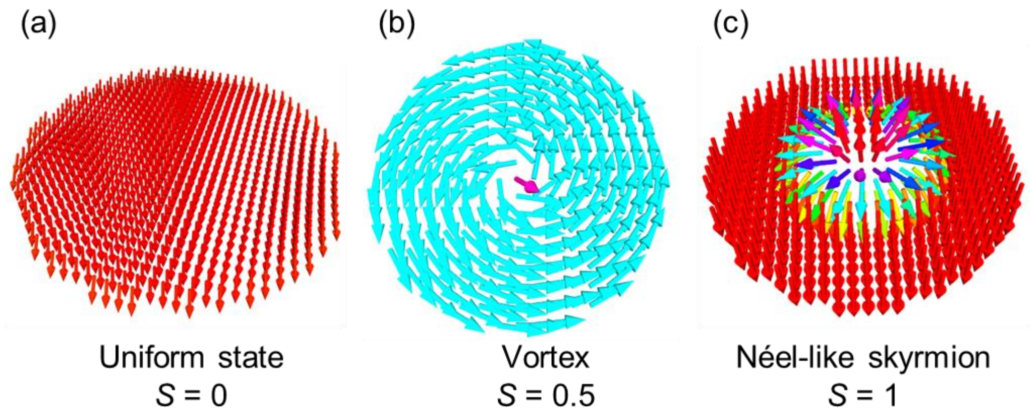

Figure B1: Three representative magnetization configurations. (a) uniform state (S = 0), (b) Vortex (S = 0.5), and (c) Néel-like skyrmion (S =1).

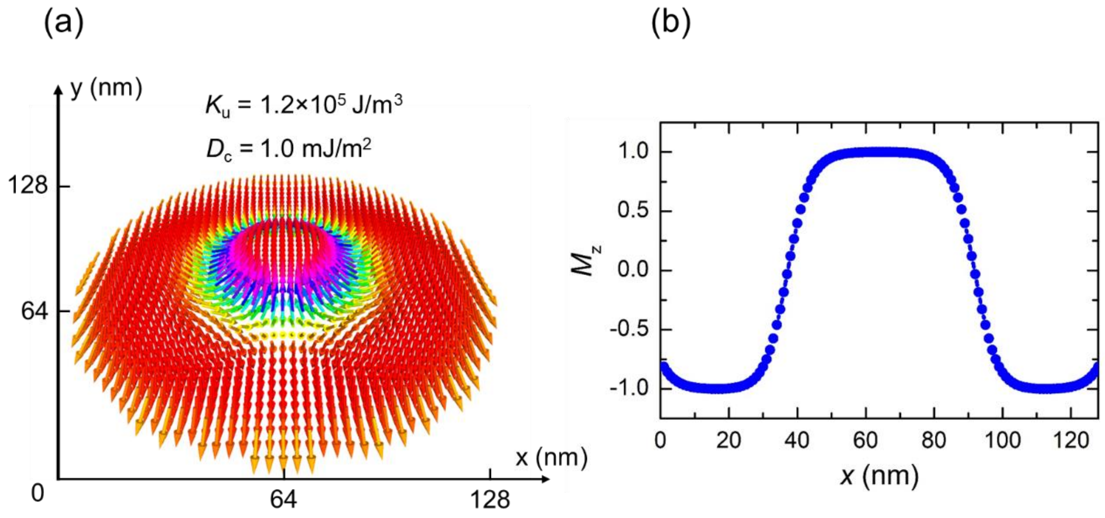

Figure B2: (a) Néel-like skyrmion simulated by MuMax3 at K_{u} = 1.2×105 J/m3 and D = 1.0 mJ/m^2. (b) M_{z} profile along the x direction for the Néel-like skyrmion in Fig. B2 at y = 64 nm. The size of the skyrmion is about 55 nm.

Acknowledgments

First of all, I would like to express my gratitude to my supervisor, Prof. Pham Nam Hai who has greatly supported and constantly guided me with his wisdom, tranquility and professionalism in these years. He not only taught me physics, helped me solve the problems blocking my researches, but also let me know the passion and pleasure when becoming a research scientist. 3-year is not a long time but it is enough for me to understand that he is a great supervisor and become a researcher under his guidance is a wonderful thing. Without his support, this research would not be completed.

I would like to especially thank my co-worker Mr. Yugo Ueda who has been my tutor since the first day of my PhD program. With his patient and thoughtful advice, he taught me about the fabrication process, device fabrication, measurement setup and many more things in physics. He shared with me about personal things and endless discussions that we have enjoyed together.

I wish to express my sincere thankfulness to Dr. Duong Dinh Hiep, Dr. Nguyen Thanh Tu and Dr. Bui Cong Tinh who always are my best friends and support me in this PhD research.

I would like to thank other members in my Lab, such as Mr. Yoshida, Mr. Otsuka, Mr. Nishishima, Mr. Yamane, Mr. Chonan, Mr. Tuo, Mr. Shirokura and especially Mr. Kenichiro Yao for their help, technical supports and joyful discussions about Japan and life.

I would like to thank the members of Tanaka Lab at Tokyo University, Munekata Lab and Nakagawa Lab in Tokyo Institute of Technology who kindly supported me in the experiment.

I wish to express my thankfulness to Mr. Ida and other members in Ookayama Materials Analysis Division for their technical supports in the experiment.

I would like to acknowledge the Japanese Government (MEXT) Scholarship for their financial support in this PhD study.

Finally, I would like to deeply thank my beloved family for your endless supports and encouragement.

Related publications and presentations

Papers

1. **N. H. D. Khang**, Y. Ueda, and P. N. Hai, "A conductive topological insulator with large spin Hall effect for ultralow power spin-orbit torque switching", Nature Materials **17**, 808 (2018).

2. P. N. Hai, **N. H. D. Khang**, K. Yao, and Y. Ueda, "Conductive BiSb topological insulator with colossal spin Hall effect for ultra-low power spin-orbit-torque switching", Proc. SPIE **10732**, 107320U (2018).

3. K. Yao, **N. H. D. Khang**, P. N. Hai, "Influence of crystal orientation and surface termination on the growth of BiSb thin films on GaAs substrates", Journal of Crystal Growth **511**, 99 (2019).

4. **N. H. D. Khang**, Y. Ueda, K. Yao, and P. N. Hai, "Growth and characterization of MnGa thin films with perpendicular magnetic anisotropy on BiSb topological insulator", Journal of Applied Physics **122**, 143903 (2017) (**selected as feature paper with an AIP Scilight article**).

5. Y. Ueda, **N. H. D. Khang**, K. Yao, and P. N. Hai, "Epitaxial growth and characterization of $Bi_{1-x}Sb_x$ spin Hall thin films on GaAs(111)A substrates", Applied Physics Letters **110**, 062401 (2017).

6. **N. H. D. Khang**, and P. N. Hai, "Giant Unidirectional Magnetoresistance in topological insulator-ferromagnetic semiconductor heterostructures", (submitted and under review).

7. **N. H. D. Khang**, T. Fan, and P. N. Hai, "Field-free ground-state skyrmions in BiSb/MnGa bi-layers at room temperature revealed by topological Hall effect", (in preparation).

Patent application

Patent name: “Method to fabricate ferromagnets/BiSb heterostructures and magnetoresistive memory”.

Japanese and PCT patent applications, No. 2017-177564.

Inventors: P. N. Hai, **N. H. D. Khang**.

Presentations

International Conferences

1. **N. H. D. Khang**, T. Fan, and P. H. Hai, “Observation of topological Hall effect and field-free stable skyrmions in MnGa/BiSb bi-layers at room temperature”, The 10th International School and Conference on Spintronics and Quantum Information Technologies (Spintech X), June 2019.
2. **(Invited) N. H. D. Khang**, Y. Ueda, and P. N. Hai, “Colossal spin Hall effect in a conductive topological insulator $Bi_{0.9}Sb_{0.1}$ for ultra-low-power spin-orbit-torque switching”, The 11th Vietnam-Japan Scientific Exchange Meeting, September 2018.
3. **N. H. D. Khang**, Y. Ueda, and P. N. Hai, “Ultra-low-power spin-orbit-torque switching using the colossal spin Hal effect in BiSb topological insulator”, Intermag2018, April 2018.
4. **N. H. D. Khang**, Y. Ueda, and P. N. Hai, “Magnetic and structural properties of MnGa thin films grown on $Bi_{0.8}Sb_{0.2}$ topological insulator”, Junjirou Kanamori Memorial International Symposium – New Horizon of Magnetism, September 2017.
5. **N. H. D. Khang**, Y. Ueda, and P. N. Hai, “MnGa thin films grown on BiSb topological insulator for SOT-MRAM”, The 10th Vietnam-Japan Scientific Exchange Meeting, September 2017.
6. **N. H. D. Khang**, Y. Ueda, and P. N. Hai, “MnGa thin films with perpendicular magnetic anisotropy grown on BiSb topological insulator”, Spintech IX, July 2017.

Domestic Conferences

1. **N. H. D. Khang**, and P. N. Hai, “Large Unidirectional Magnetoresistance in GaMnAs/BiSb bilayers”, The 66th JSAP Spring meeting, March 2019.

2. **N. H. D. Khang**, T. Fan, and P. N. Hai, “Field-free ground-state skyrmions in BiSb/MnGa bi-layers at room temperature revealed by topological Hall effect”, PASPS-23, December 2018 (**best student English presentation award**).

3. **N. H. D. Khang**, T. Fan, and P. N. Hai, “Field-free ground-state skyrmions in BiSb/MnGa bi-layers at room temperature revealed by topological Hall effect”, The 79th JSAP Autumn Meeting, September 2018.

4. **N. H. D. Khang**, Y. Ueda, and P. N. Hai, “Room-temperature colossal spin Hall effect in topological insulator $Bi_{0.9}Sb_{0.1}$(012) thin films for ultra-low-power spin-orbit-torque switching, The 65th JSAP Spring meeting, March, 2018.

5. **N. H. D. Khang**, Y. Ueda, and P. N. Hai. MnGa thin films with perpendicular magnetic anisotropy grown on BiSb topological insulator, The Tokyo Tech Spintronics Symposium 2017, July 2017.

6. **N. H. D. Khang**, and P. N. Hai, “Growth and characterization of MnGa thin films on BiSb topological insulator”, The 64th JSAP Spring meeting, March 2017.